HAZ SOFTENING KINETICS IN DUAL-PHASE AND MARTENSITIC STEELS

HEAT-AFFECTED ZONE SOFTENING KINETICS IN DUAL-PHASE AND MARTENSITIC STEELS

By ELLIOT BIRO, B.A.Sc., M.A.Sc.

A Thesis
Submitted to the School of Graduate Studies
in Partial Fulfillment of the Requirement for the Degree
Doctor of Philosophy

McMaster University

Doctor of Philosophy (2013)	McMaster University
(Materials Science and Engineering)	Hamilton, Ontario

TITLE:	Heat-Affected Zone Softening Kinetics in Dual-Phase and Martensitic Steels
AUTHOR:	Elliot Biro, B.A.Sc., M.A.Sc. (University of Waterloo)
SUPERVISORS:	Dr. Joseph R. McDermid Dr. J. David Embury Dr. Y. Norman Zhou
NUMBER OF PAGES:	xxii, 167

Dedicated to
Dina, Saul and Miriam

ABSTRACT

Advanced high strength steels, such as dual-phase and martensitic steels, are increasingly being used by automakers to decrease the thickness of steel sheet used in parts without sacrificing part strength. When welded, the martensite within the dual-phase and martensitic steel microstructures tempers, reducing the heat-affected zone (HAZ) hardness compared to the base material, locally reducing strength. This process is known as HAZ softening. HAZ softening has been well studied; however, the kinetics of this process has not been quantified and the processes responsible for HAZ softening have not been examined. This thesis investigated both of these topics.

HAZ softening was modelled using the Johnson-Mehl-Avrami-Kolmogorov (JMAK) equation. As the thermal profile during welding is non-isothermal, the effects of temperature and time on steel tempering kinetics could not be separated by examining post-welded properties. The effects of tempering temperature and time were separated through a series rapid isothermal tempering experiments. Hardness data from these experiments allowed the HAZ softening rate to be empirically quantified through fitting the JMAK equation. This material model was then validated by predicting HAZ softening in laser and resistance spot welds. Although the fitted JMAK constants could be used to predict post-weld HAZ hardness, they did not agree with the classic literature values associated with martensite tempering.

To understand why the JMAK coefficients did not match those of the classic martensite tempering literature, the softening data from one of the martensitic steels was re-examined. This study revealed that the softening process was a combination of two processes: carbide nucleation and carbide coarsening. The activation energies calculated for each process matched the classic literature values. Carbide coarsening dominated during tempering, which had a non-linear relation with change in hardness. The relationship between carbide coarsening and hardness was responsible for the softening kinetics measured from the rapid tempering experiments.

ACKNOWLEDGEMENTS

This work could not have been possible without contributions from many people. Firstly I would like to thank my supervisors: Dr. David Embury who accepted me as a student and consistently challenged me by asking me some of the most interesting questions I've heard. He also taught me that a hotel restaurant in Paris is possibly the best place to hold a supervisor meeting. Dr. Joseph McDermid kept me on track as I progressed through McMaster and continually questioned my data, which allowed me to understand where I needed to improve both my experiments and theories. Finally Dr. Norman Zhou both pushed me to start my PhD, and pushed me to complete it. His knowledge of welding processes and labs helped me to tie my fundamental metallurgical observations to the real world experience of welding.

This work would not have been as strong as it was without the input and conversations from my colleagues in ArcelorMittal Global research. Christine Kaczynski, Samuel Vignier, Mathilde Hervé, and Antoine Tulupe heat treated samples for me with the Gleeble. Patrick Barge taught me how to prepare thin foils, and then let me use his TEM to view them. Collin Scott took the time to sit with me, offered his opinion on my electron micrographs and let me know which samples needed to be redone. Annick Willems prepared my TEM samples using her FIB when I thought

that producing a thin foil just where I wanted was impossible. Emmanuel Lucas, Thomas Dupuy, and Arnaud Lens all offered invaluable insight on some of my observations. Finally, Olivier Bouaziz who convinced me both that the easier issues of martensite softening should be solved before tackling softening in DP steels and my calculated softening kinetics did not match literature and needed to be further studied. Thank-you all for opening your labs to me and giving me your time, especially now when resources are as strained as they are and you all have important duties to carry-out.

I would like also like to thank the students and post-doctorial fellows and professors from the Centre for Advanced Materials Joining at the University of Waterloo. Thank-you Dr. Sashank Nayak, Dr. Victor Baltazar, Dave Huang, Daniel Westerbaan, Dr. Mingsheng Xia, and Dr. Mary Wells for offering your insight and collaborations. This work would not have been possible without your input and discussions.

Much of the electron microscopy in this work would also not have been possible without the assistance of Fred Pearson, Steve Koprich, and Andy Duft from the Brockhouse Institute for Material Research who all helped me preparing my samples and operating the equipment at the Canadian Centre for Electron Microscopy.

I would also like to thank ArcelorMittal who both sponsored this study, provided all of the my material and permitted me to use company resources to pursue these problems.

Finally I would like to mention my family who had to put up with six years of me being distracted and not being able to always put them first. Dina, Saul and Miriam, I am happy to say that you can now have your husband and daddy back.

TABLE OF CONTENTS

ABSTRACT .... **iv**

ACKNOWLEDGEMENTS .... **vi**

TABLE OF CONTENTS .... **ix**

LIST OF TABLES .... **xii**

LIST OF FIGURES .... **xiii**

LIST OF ABBREVIATIONS AND SYMBOLS .... **xviii**

DECLARATION OF ACADEMIC ACHIEVEMENT .... **xxi**

1 Introduction **1**

2 Literature Review **4**

- 2.1 Microstructure and mechanical properties of DP and Martensitic Steels 5
  - 2.1.1 Development of DP mechanical properties 7
- 2.2 Welding 16
  - 2.2.1 Laser Welding 18
  - 2.2.2 Welding Transformations 21
- 2.3 Martensite Tempering 26
- 2.4 Softening in the HAZ of DP and Martensitic Weldments 29
  - 2.4.1 Effect of HAZ softening on mechanical properties 30
  - 2.4.2 Effect of martensite content on HAZ softening 32
  - 2.4.3 Effect of welding heat input on HAZ softening 34
  - 2.4.4 Effect of DP steel chemistry on HAZ softening 35
- 2.5 Martensite Tempering Models 36
  - 2.5.1 Carbide nucleation and growth models 36
  - 2.5.2 Empircal methods modelling hardness changes from martensite tempering 40
  - 2.5.3 Tempering Parameters 41
  - 2.5.4 Johnson-Mehl-Avrami-Kolmogorov Transformation Model 42
  - 2.5.5 Adaption of Models to Non-Isothermal Tempering 47

3 Softening Kinetics in the Sub-Critical Weld HAZ **52**

- 3.1 Abstract 52
- 3.2 Introduction 53
- 3.3 Methodology 55
  - 3.3.1 Materials 55
  - 3.3.2 Welding 58
  - 3.3.3 Measuring Welding Heat Input 58
  - 3.3.4 Sample Preparation 60

3.3.5 Microhardness....60
3.3.6 Electron Microscopy....61
3.4 Results....62
3.4.1 Softening in DP Steels....62
3.4.2 Decomposition Products in Low and High Heat Input Welds....64
3.5 Discussion....67
3.5.1 Comparison of Softening Kinetics....67
3.5.2 Fitting Softening Kinetics to the Avrami Equation....69
3.6 Conclusions....75
3.7 Acknowledgements....76
3.8 References....76

4 Predicting Transient Softening in the Sub-Critical HAZ of DP and Martensitic Steels....79
4.1 Abstract....79
4.2 Introduction....80
4.3 Methodolgy....83
4.3.1 Softening Kinetics Model....88
4.3.2 Modelling of Weld Temperature History....89
4.4 Results and Discussion....91
4.4.1 Tempering Kinetics Quantification....91
4.4.2 Using the JMAK equation to describe non-isothermal tempering during welding....98
4.4.3 Predicting the hardness of laser and spot welds at r_{Ac1}....99
4.4.4 Microstructural comparison of sub-critical weld HAZ and Gleeble samples....102
4.5 Conclusions....108
4.6 Acknowledgements....109
4.7 References....110

5 Decoupling of the Softening Processes during Tempering of a Martensitic Steel....113
5.1 Abstract....113
5.2 Introduction....114
5.3 Experimental Methods....117
5.4 Johnson-Mehl-Avrami-Kolmogorov Softening Kinetics Model 120
5.5 Results....122
5.5.1 Tempering Data Analysis....122
5.5.2 Stage I Softening – Carbide Nucleation....125
5.5.3 Ferrite Grain Size....127
5.5.4 Stage II Softening – Carbide Coarsening....129
5.6 Discussion....133
5.7 Conclusions....139
5.8 Acknowledgements....141

5.9 Nomenclature 141
5.10 References 142
6 Discussion 146
6.1 Processes Responsible for softening 146
6.2 Softening Kinetics 149
6.3 Predicting softening in welds 154
7 Conclusions and Future Work 156
7.1 Conclusions 156
7.2 Future Work 158
8 References 160

LIST OF TABLES

Table 3-1. Details of Base Materials Used in Study. Steel Chemistries Given in Wt Pct (At. Pct)................................ 57
Table 3-2. Laser Characteristics Used for Welding. 58
Table 3-3. Fitting constants for the Avrami Equation........................... 71
Table 4-1. Details of experimental materials (chemistry listed in wt%) 84
Table 4-2. Tempering parameters for experimental steels. 85
Table 4-3. JMAK fitting parameters and model goodness of fit measurement for experimental steels. 95
Table 4-4. Minimum hardness and time constants of weld samples to validate JMAK softening model (Figs. 4-7 and 4-8).. 101
Table 4-5. Relative t_{Ac1} and ϕ values of samples used for TEM examination... 103
Table 5-1. Chemistry (in wt%) and hardness of M220 experimental steel. 117
Table 5-2. Temperatures and times used for experimental rapid tempering heat treatments. 118
Table 5-3. Time required to complete Stage I softening for tempering temperatures between 360℃-650℃. 127
Table 5-4. Cementite equivalent diameter and densities with associated inter-particle distance and ΔH from samples tempered at 500℃....................... 131
Table 6-1. JMAK fitting parameters and model goodness of fit measurement for experimental steels (copied from Table 4-3).. 154

LIST OF FIGURES

Figure 2-1. Typical engineering stress-strain curves of DP steels [3]. 5
Figure 2-2. Typical engineering stress-engineering strain curves of martensitic steels [3]. 7
Figure 2-3. Flow stress and UTS of DP steels as a function of martensite volume fraction [5]. 8
Figure 2-4. Effect of increasing intercritical annealing temperature (decreasing martensite C content) on the strength of DP steels [7]. 9
Figure 2-5. Engineering stress-strain curves of a DP and conventional steel with similar ultimate tensile strengths [7]. 11
Figure 2-6. TEM micrographs showing the a) high dislocation density adjacent to martensite grains and b) the low dislocation density in the bulk of a ferrite grain in as-produced DP steel [8]. 11
Figure 2-7. UTS and YS of various DP steels as a function of cooling rate [9]. 12
Figure 2-8. Yield strength of DP steel as a function of martensite volume fraction [10]. 12
Figure 2-9. Stress-strain curves of two materials with the same UTS but different strain hardening rates. 14
Figure 2-10. Log-log plot of strain hardening rate with increasing strain for a DP steel [8]. 15
Figure 2-11. Comparison of the strain hardening rates of several steel families [7]. 16
Figure 2-12. Schematic of weld pools formed from laser welding in a) conduction and b) keyhole [20]. 21
Figure 2-13. Temperature distribution of a Rosenthal type solution as measured a) on the plate surface and b) along the weld centreline [28]. 24
Figure 2-14. Temperature distribution of a typical steel weld and its correlation to the Fe-C phase diagram [22]. 25
Figure 2-15. Micrographs of a) martensite and b) tempered martensite in a 0.12 wt% C steel [31]. 27

Figure 2-16. Summary of Fe-C martensite decomposition processes as a function of temperature during a one hour heat treatment [36]. 28

Figure 2-17. Hardness profiles from four steels [39]............................... 30

Figure 2-18. DP600 Microstructure in a) the base metal showing ferrite (grey phase) and martensite (white phase) b) and the tempered HAZ showing ferrite and tempered martnsite (light grey speckled phase). Etchant: LePera's Tint [41]. 30

Figure 2-19. Change in stress-strain curves from the simulated tempered HAZ in DP780 [43]. 31

Figure 2-20. Limiting dome height of DP980 laser welded blanks made with a range of heat inputs to generate various amounts of HAZ softening [44]... 32

Figure 2-21. Hardness profiles through laser welds in three DP steels [27].. 33

Figure 2-22. Correlation between HAZ softening and DP steel martensite volume fraction [27]. 33

Figure 2-23. HAZ softening observed in two DP600 steels as a function of weld heat input [41]... 35

Figure 2-24. Tempering diagrams for a) carbon steel and b) the influence of various alloying elements when tempering at 600ºF [51]. 41

Figure 2-25. Schematic of the nucleation and growth of a daughter phase (β) from a parent phase at three points in time. At long times (t_3) kinetic models may over-predict the transformed volume if previously transformed material is not accounted for [53]. 44

Figure 2-26. General shape of the JMAK equation. 46

Figure 2-27. Illustration of a JMAK curve calculated from a two-temperature heat treatment using the additive method [72]. 49

Figure 2-28. Illustration of a) general non-isothermal heat treatment and b) the equivalent isothermal heat treatment calculated using the temperature domain method [70]. 50

Figure 3-1. Base material microstructures of (a) Cr DP600, (b) Cr/Mo DP600, (c) rich chemistry DP780, and (d) lean chemistry DP780. Increased magnification of autotempered martensite from indicated areas are shown in the micrograph insets. 57

Figure 3-2. Cross section of a typical weld showing the distance from the centreline to the fusion boundary (r_m) and the edge of the intercritical zone (r_{Ac1}) (taken from Ref. 8)....... 59

Figure 3-3. Minimum HAZ hardness *vs* time constant for DP600 materials. Note that weld heat input increases with increasing τ, per Eq. [3-2]. 63

Figure 3-4. Minimum HAZ hardness *vs* time constant for DP780 materials and the time constants of the welds examined in Fig. 5. Note that weld heat input increases with increasing τ. 63

Figure 3-5. Martensite phase found in the softened HAZ from a) low and b) high heat input welds from the lean DP780 steel. 64

Figure 3-6. TEM images of cementite particles found in the sub-critical HAZ of the lean chemisty DP780 welded with a) low and b) high heat input as well as examples of individual particles and their SAD patterns from the welds made with c) low and d) high heat input.................. 66

Figure 3-7. TEM images of cementite particles found in the sub-critical HAZ of the rich chemisty DP780 welded with a) low and b) high heat input as well as examples of individual particles and their SAD patterns from the welds made with c) low and d) high heat input.................. 67

Figure 3-8. Progression of martensite decomposition in DP600 steels with increasing heat input. 72

Figure 3-9. Progression of martensite decomposition in DP780 steels with increasing heat input. 72

Figure 3-10. Comparison between the softening kinetics of all steels examined. The compositional information is the calculated martensite C content, per Table 3-1........... 73

Figure 3-11. Avrami *k* parameter *vs* martensite C content for all experimental steels. 74

Figure 4-1. Typical Gleeble heat treatment cycle (taken from a 650°C peak annealing temperature cycle). 85

Figure 4-2. Comparison between the exact temperature history during welding and that of the parabolic temperature history for an arbitrary area within the HAZ (taken from [Ref. 23]). 91

Figure 4-3. Hardness of tempered DP780 as a function of tempering time and temperature. 92

Figure 4-4. Hardness of tempered M220 as a function of tempering time and temperature. 93

Figure 4-5. Calculated fraction of softening completed for DP780 as a function of tempering time and temperature. 93

Figure 4-6. Calculated fraction of softening completed for M220 as a function of tempering time and temperature. 94

Figure 4-7. Comparison between the measured hardness and the hardness predicted by the JMAK equation using the parameters listed in Table 4-3. 101

Figure 4-8. Comparison between the measured HAZ softening and the HAZ softening predicted by JMAK equation using the parameters listed in Table 4-3. 102

Figure 4-9. Structure of the as-received DP780 at (a) low and (b) high magnification. 103

Figure 4-10. Tempered HAZ of DP780 welded with high heat input showing (a) the decomposed microstructure and (b) an area with large carbides along with the SAD pattern of the carbides found in the decomposed martensite. 104

Figure 4-11. DP780 heat treated in the Gleeble at 650℃ for 10 s showing (a) the decomposed microstructure and (b) the SAD pattern of the carbides found in the decomposed martensite from the indicated area. 105

Figure 4-12. Tempered HAZ of DP780 welded with low heat input showing (a) the partially decomposed microstructure and (b) the SAD pattern of the carbides found in the decomposed martensite. 106

Figure 4-13. DP780 heat treated in the Gleeble at 650℃ for 0.5 s showing (a) the decomposed microstructure (b) an area with large carbides along with the SAD pattern of the carbides found in the decomposed martensite. 106

Figure 5-1. Softening progress (ϕ) versus tempering time for experimental M220 alloy. 121

Figure 5-2. Transformed M220 softening data. 123

Figure 5-3. SEM microstructures of the a) as-received M220 and after tempering at 400˚C for b) 0.2 s, c) 1 s d) 2 s and at 500˚C for e) 0.2 s, f) 1 s and g) 2 s. 125

Figure 5-4. Arrhenius plot of *k* verus *1/T* for Stage I softening data (Figure 5-2) for samples tempered between 360-420˚C. 126

Figure 5-5. Optical microstructures of samples tempered at a) 500℃ for 0.2s and b) 600℃ for 10s. 128

Figure 5-6. Average carbide equivalent diameter versus temping time for samples tempered at 500℃ and 600℃. 130

Figure 5-7. Comparison between the measured hardness from samples tempered at 500℃ and the hardness predicted by the modified Ashby-Orowan model [31]....... 132

Figure 5-8. Arrhenius plot of *k* verus *1/T* for Stage II softening data (Figure 5-2). 133

Figure 5-9. Softening progress (ϕ) versus cementite particle diameter for samples tempered at 500℃........... 138

Figure 6-1. Transformed softening data for M220 steel (copied from Figure 5-2). 147

Figure 6-2. Time to complete carbide nucleation stage during rapid tempering of M220 (data taken from Table 5-3). 148

Figure 6-3. Comparison between the softening kinetics of four steels with various martensite volume fractions and alloying additions, per Table 3-1 (copied from Figure 3-10)... 151

Figure 6-4. Softening (ϕ) of M190 and M220 versus effective tempering times at 650℃........................ 153

Figure 6-5. Logarithmic transformation of the M190 and M220 softening data adjusted to 650℃. 154

Figure 6-6. Comparison between the measured HAZ softening and the HAZ softening predicted by the JMAK equation using the parameters listed Table 4-3 (copied from Figure 4-8). 155

LIST OF ABBREVIATIONS AND SYMBOLS

a	thermal diffusivity ($\lambda/\rho c$)
AHSS	advanced high strength steel
b	length of the burgess vector
c	specific heat capacity
$c_{H\text{-}J}$	Hollomon-Jaffe carbon dependent tempering constant
C_0	equilibrium solute concentration in the matrix
$\mathrm{CE_N}$	Yurioka carbon equivalent
CI	confidence interval
C_R	solute concentration in the matrix adjacent to the particle
CP	complex phase
c_p	constant pressure specific heat capacity
d	sheet thickness
d_p	particle diameter
d_{p0}	initial particle diameter
D	coefficient of diffusion
D_V	volumetric coefficient of diffusion
D_{GB}	grain boundary coefficient of diffusion
DP	dual-phase
f_{MART}	martensite volume fraction
FIB	focused ion beam
G	shear modulus
G^*	activation energy to form the smallest stable particle size
G_R	particle growth rate
GMAW	gas metal arc welding
h	Planck constant
H	hardness
H_∞	minimum hardness
H_{Base}	base metal hardness
H_{min}	minimum hardness
H_{BM}	base metal hardness
$H_{C,T}$	tempered martensite hardness accounting for martensite C content and tempering temperature
ΔH	change in hardness
ΔH_x	change in tempered martensite hardness associated with alloying addition x
HAZ	heat-affected zone
I	nucleation rate
JMAK	Johnshon-Mehl-Avrami-Kolmogorov
k	transformation kinetics associated with growth and nucleation

k_0	fitting parameter for k
k_1	geometric constant
k_B	Boltzmann constant
k_D	diffusion dependent constant
k_{GB}	combination of metallurgical factors affecting grain boundary diffusion
k_{i+1}	kinetics associated with the current isothermal section
k_{Pipe}	combination of metallurgical factors affecting pipe diffusion
k_v	combination of metallurgical factors affecting volumetric diffusion
L	interparticle spacing
LBW	laser beam welding
LDH	limiting dome height
m	particle coarsening rate exponent
M_T	Taylor factor
n	JMAK reaction rate exponent
N_V	number of nucleation sites
PHS	press hardened steel
q	conversion factor between hardness and yield strength
Q	activation energy
Q^*	energy barrier for atoms to pass from the matrix to the particle
Q_{net}	net heat input
r	distance from heat source
$\bar{r}$	average cementite radius
$\bar{r}_0$	initial average cementite radius
R	universal gas constant
r_{Ac1}	distance from the weld centreline to the Ac$_1$ isotherm
r_m	distance from the weld centreline to the fusion boundary
r_p	particle radius
RSW	resistance spot welding
SAD	select area diffraction
SEM	scanning electron microscope
t	time
t_0	initial time
t_i^*	adjusted time for the start of the current isothermal section
t_{Ac1}	isothermal tempering time at the Ac$_1$ temperature resulting in the same softening progression as the original non-isothermal heat treatment
Δt_{i+1}	duration of the current isothermal section
T	instantaneous temperature
T_0	initial temperature
T_{Ac1}	Ac$_1$ temperature
T_m	melting temperature

TEM	transmission electron microscope
TRIP	transformation induced plasticity
UTS	ultimate tensile strength
v	welding speed
V	total volume of material
V_M	molar volume
V^β	volume of daughter phase
V_e^β	volume of daughter phase formed by nucleation and particle growth without accounting for previously transformed material
YAG	Yittrium Aluminum Garnet
YPE	yield point elongation
YS	yield strength
α	constant amalgamating the particle/matrix surface tension and matrix solute concentration
δ	grain boundary thickness
ε_{True}	true strain
ϕ	normalized softening progression
ϕ_ι	softening progression at the beginning of the current isothermal section
$\phi_{\iota+1}$	softening progression at the end of the current isothermal section
γ	surface free energy per unit area of the particle/matrix interface
λ	thermal conductivity
ν	molar density
ρ	material density
σ_{True}	true stress
σ_{ST}	surface tension of the carbide/matrix interface
τ	time constant – time to heat from initial temperature to peak temperature

DECLARATION OF ACADEMIC ACHIEVEMENT

The academic contribution of the work within this thesis was prepared by the candidate with assistance from others. Chapters 3-5 of the thesis comprise of manuscripts from the candidate's thesis research that have either been published or are currently under review in peer-reviewed scientific journals. Chapter 6 comprises an overall discussion of the contributions found within Chapters 3-5. The candidate is the primary author for the manuscripts found within Chapters 3-5. The individual contributions to these chapters from each co-author are detailed below.

Chapter 3 reprints the manuscript "E. Biro, J.R. McDermid, J.D. Embury, and Y. Zhou, *Softening Kinetics in the Sub-Critical Weld HAZ*, Metall. Mater. Trans. A., vol. 41A, no. 9, pp. 2348-2356, 2010". For this contribution, the author planned and supervised the experiments, performed all samples analyses, carried out the data analysis, wrote the first draft of the manuscript and implemented out all subsequent modifications. Dr. McDermid, Dr. Embury and Dr. Zhou assisted with data analysis, edited the manuscript and supervised modifications and revisions to the paper.

Chapter 4 reprints the manuscript "E. Biro, S. Vignier, C. Kaczynski, J.R. McDermid, E. Lucas, J.D. Embury, and Y.N. Zhou, *Predicting Transient Softening in the Sub-Critical Heat-Affected Zone of Dual-Phase and Martensitic Steel Welds*, ISIJ Int., vol. 53, no. 1, pp. 110-118, 2013".

For this manuscript, the author planned and supervised the experiments, conducted all of the microscopy, carried out the necessary data analysis, wrote the first draft of the manuscript and implemented all required modifications. Mr. Vignier and Ms. Kaczynski carried out all of the Gleeble experiments and Mr. Vignier also carried out all hardness testing. Mr. Lucas supervised Mr. Vignier and Ms. Kaczynski. Dr. McDermid, Dr. Embury and Dr. Zhou assisted with data analysis, edited the manuscript and supervised modifications and revisions to the paper.

Chapter 5 reprints the manuscript “E. Biro, J.R. McDermid, S. Vignier, and Y.N Zhou, *Decoupling of the Softening Processes during Tempering of a Martensitic Steel*” has been of submitted for review in Acta Materialia on July 25, 2013 and was assigned manuscript number A-13-1737. The submission was still under review as of the time of submission of this thesis. For this contribution, the candidate performed all metallurgical analysis as well as the data analysis. The candidate also wrote the first draft of the manuscript and carried out all required modifications. Mr. Vignier supervised the production of the additional Gleeble samples. Dr. McDermid and Dr. Zhou assisted with data analysis, edited the manuscript and supervised the modifications and revisions to the paper.

Chapters 1, 2, 6 and 7 were entirely synthesised and written by the candidate. Dr. McDermid assisted with editing these chapters.

1 Introduction

Since the early 2000's the automotive industry has been increasingly adopting dual-phase (DP) and martensitic steels as a means to preserve structural part strength while decreasing material thickness. This has allowed automotive manufacturers to reduce vehicle weight while maintaining crash resistance. Both DP and martensitic steels have some martensite in their microstructures, which when heated between 250°C and their Ac_1 temperature will temper, softening the material. This softening process occurs in the tempered region of the heat-affected zone (HAZ) of the welds, leading to a condition known as HAZ softening. HAZ softening was first identified when DP steels were introduced for wheel rim applications in the late 1970's, where it was responsible a reduction in the weld rim strength near the weld. Since then, much work has been done to characterise how HAZ softening affects material and welded joint properties. However, little work has been performed to describe HAZ softening kinetics.

This thesis seeks to understand the kinetics of HAZ softening and has three main objectives:

1. To characterise the connection between weld heat input, steel composition, and softening,

2. To quantify softening kinetics in DP and martensitic steels and be able to predict the HAZ softening occurring during welding as a function of weld heat input,
3. To understand the mechanisms responsible for HAZ softening.

This thesis will comprise the following chapters. The current literature describing HAZ softening along with the concepts used to analyse this process will be reviewed and discussed in the Literature Review (Chapter 2). The previously posed objectives will be discussed in Chapters 3 through 5, which reprint manuscripts arising from the present research that have either been published or submitted for review in peer-review journals. Chapter 3 will discuss the softening kinetics of HAZ softening of DP steels. Chapter 4 will quantify the kinetics of HAZ softening progression in DP and martensitic steels and presents a technique to predict HAZ softening as a function of temperature history during welding. Chapter 5 will present a model connecting the stages observed in the softening process to those of tempering by presenting how the tempering process affects material hardness. This model was validated by correlating the softening progression observed in a martensitic steel to the classic martensite tempering literature. In Chapter 6, the results from Chapters 3-5 will be related to show the progression of these contributions in a brief discussion. Finally, in Chapter 7, conclusions will be drawn and possible future work will be outlined.

The papers presented in the Chapters 3 and 4 are printed in their final (accepted) form. The manuscript presented in Chapter 5 is presented in its as-submitted form as of July 25, 2013 and is subject to revision depending on the reviews received on the manuscript. However, the figures, tables, and equations numbers for all manuscripts have been re-formatted to provide a consistent style throughout this thesis. All references in Chapters 3, 4, and 5 are presented in the style specified for the journal it was submitted to. As such, the references in these chapters may be repeated, and overlap with the references in Chapters 2 and 6, the listings for which are located at the end of the thesis.

2 Literature Review

Legislation is currently in place requiring North American automotive companies to improve the fuel economy of their fleets to an estimated 4.4 l/100 km for passenger vehicles and 4.9 l/100 km for light trucks by 2025 [1]. One of the means by which automakers will achieve these goals is by reducing the weight of their vehicles, which can reduce fuel consumption by between 0.15-0.70 l/100 km per reduction of 100 kg of vehicle mass [2]. Reducing vehicle weight will require thickness reduction of the sheet steels used in the body-in-white. When steel sheet thickness is reduced, part strength may decrease. To counter the effects of reduced thickness on part strength, and thus vehicle safety, vehicle designers are increasingly incorporating advanced high strength steels (AHSS) into their designs [3]. These steels have much higher strengths than conventional steels without large reductions in formability. AHSS encompass many families of steels with various microstructures and properties such as: dual-phase (DP), transformation induced plasticity (TRIP), complex phase (CP), martensitic, and press hardened steels (PHS). This study investigated DP and martensitic steels.

2.1 Microstructure and mechanical properties of DP and Martensitic Steels

DP steels have a composite microstructure made up of ferrite, martensite and sometimes bainite [4,5]. This microstructure gives these steels unique mechanical properties when compared to those of conventional steels. For example, DP steels typically have a relatively high elongation for their ultimate tensile strength, a high tensile to yield strength ratio, no yield point elongation and are bake hardenable [4]. Commonly DP steels are classified by either their ultimate tensile strength (UTS) or both their yield strength (YS) and UTS separated by a slash. For example DP600 has a 600 MPa UTS and a DP350/600 has a 350 MPa YS and a 600 MPa UTS. A comparison of the typical stress-strain curves of DP and mild steel may be seen in Figure 2-1.

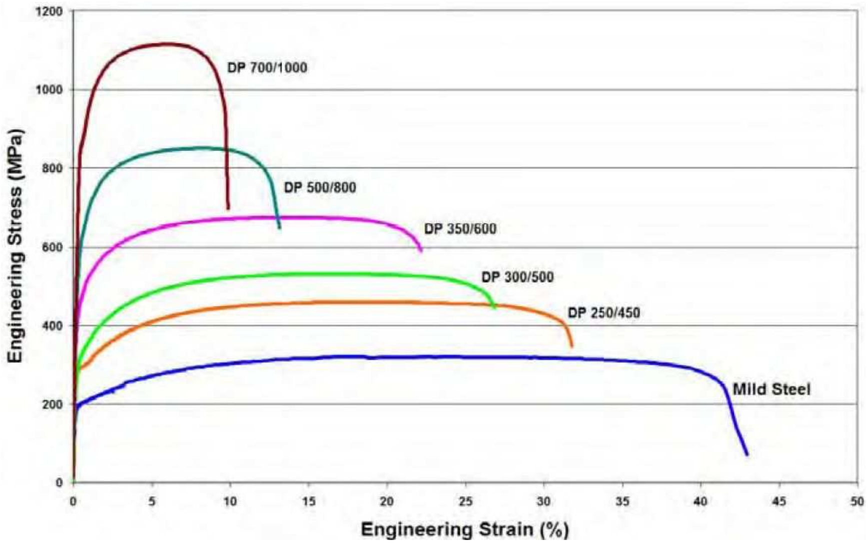

Figure 2-1. Typical engineering stress-strain curves of DP steels [3].

DP steels are made by intercritically annealing the steel, which results in a mixed microstructure of austenite and ferrite. The steel is then rapidly cooled in order to form the desired final microstructure [4,5]. The process used to carry out this heat treatment will dictate the cooling rate during quenching and the required alloy composition. When cooling rates are rapid, as occurs in a hot mill or continuous anneal line, DP steels may made with little alloying additions from a lean alloying philosophy that will not greatly increase the hardenability of the steel. Typically C, Mn and Si are the only elements used to alloy lean DP steels. However, when DP steels are processed using low cooling rates, as occurs in continuous hot-dip galvanizing, Cr and Mo additions are often needed to delay the pearlitic and bainitic transformations. Delaying these transformations allows sufficient austenite to remain in the structure during cooling to produce the desired martensite volume fraction in the final microstructure [3].

Martensitic steels have a microstructure that is almost entirely martensitic. They are usually fabricated industrially by rapidly quenching either on the run-out table in the hot mill or in a continuous annealing line [3]. To increase ductility, martensitic steels may be subjected to a small amount of tempering. Martensitic steels typically have very high strength (a YS ranging between 950 - 1250 MPa and a UTS ranging between 1200-1500 MPa [3]) and low ductility. Their strength depends on their C content [6] and any possible tempering. Typical stress-strain curves of selected martensitic steels may be seen in Figure 2-2.

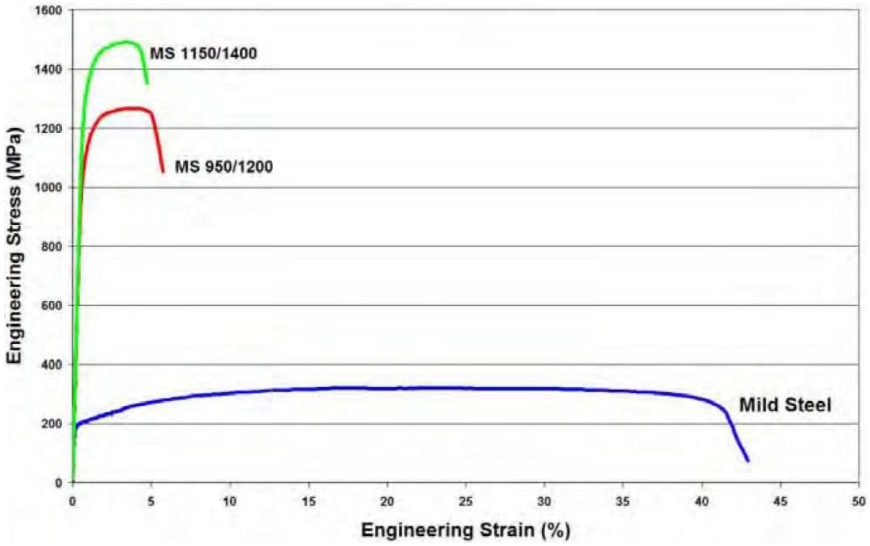

Figure 2-2. Typical engineering stress-engineering strain curves of martensitic steels [3].

2.1.1 Development of DP mechanical properties

The mechanical properties of DP steels are derived from a complex interaction between the ferrite and martensitic phases within its microstructure. The yield strength and ultimate tensile strength of DP steels increase with increasing martensite volume fraction as well as the strengthening mechanisms of other engineering materials such as grain boundary strengtheninging and cold work [5], which may be seen in Figure 2-3. Increasing C content of the martensite phase within the DP structure will also increase the strength of DP steels [4], but to a lesser degree than does increasing the martensite volume fraction [7] (see Figure 2-4) .

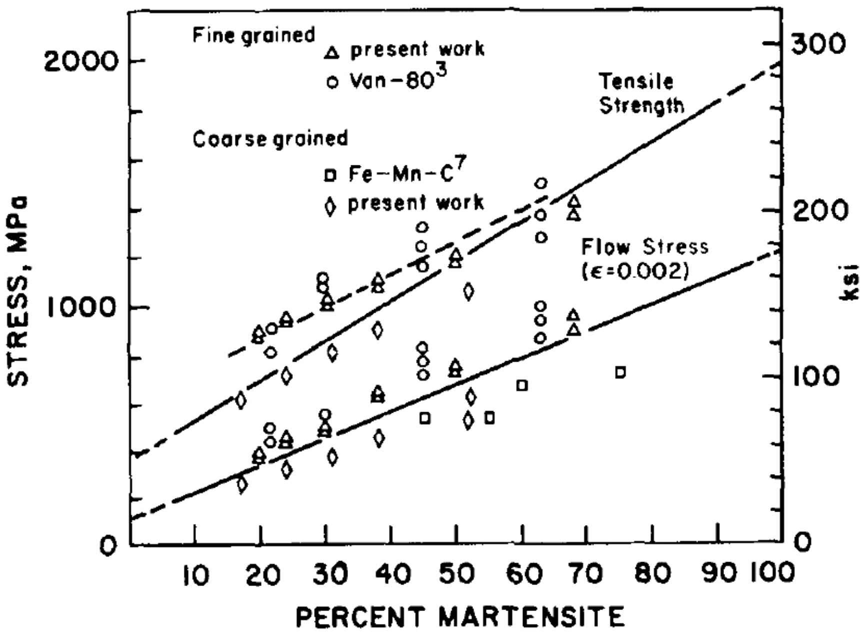

Figure 2-3. Flow stress and UTS of DP steels as a function of martensite volume fraction [5].

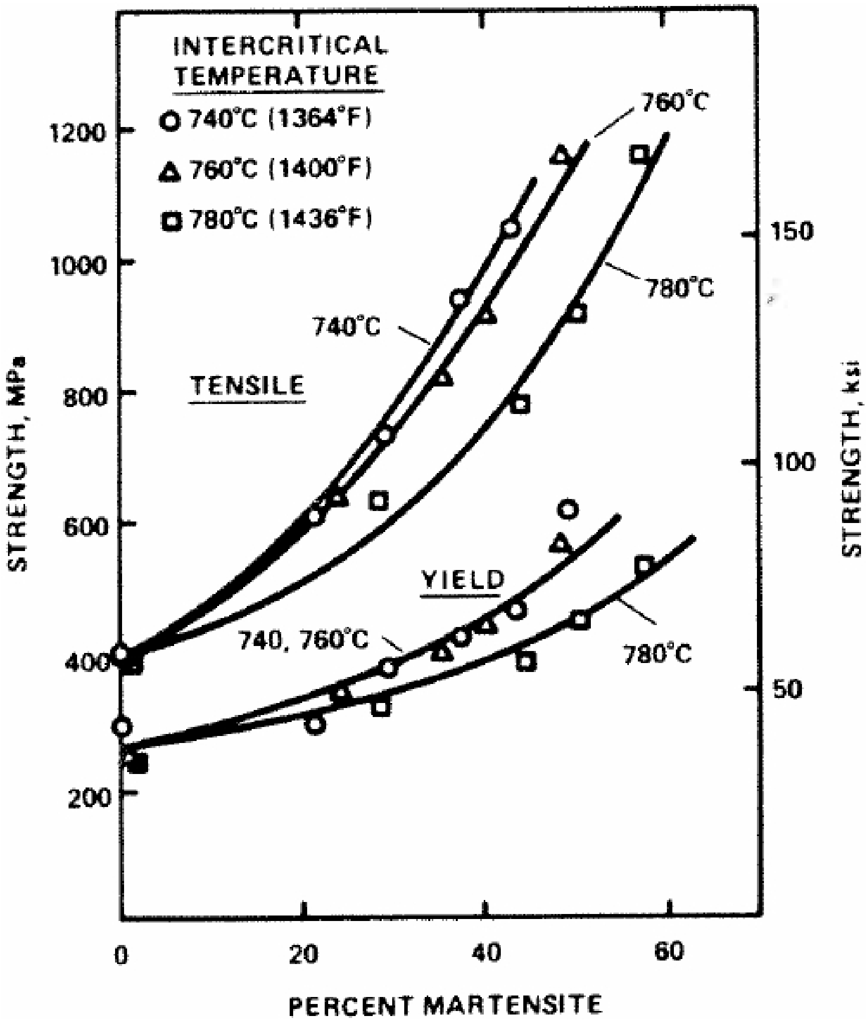

Figure 2-4. Effect of increasing intercritical annealing temperature (decreasing martensite C content) on the strength of DP steels [7].

The combination of high strength and ductility as compared to conventional steels (see Figure 2-5) and the elimination of yield point elongation (YPE) are due to the interaction of dislocations in the ferrite adjoining the martensite grains. When DP steels are quenched after intercritical annealing, the austenite transforms to martensite. As the density of martensite is lower than austenite, the material increases in volume giving rise to local residual compressive stress, which in-turn create a high density of unpinned dislocations in the surrounding ferrite, known as geometrically necessary dislocations (see Figure 2-6) [4,8]. When DP steels are strained, dislocation density rapidly increases in the ferrite adjacent to the martensite grains. This rapidly increases material flow stress without the YPE typically in conventional low C steels [4,9]. The dislocation density in the ferrite adjacent to the martensitic grains saturates at strains of approximately 0.02 [8]. At higher strain levels, dislocations within the ferrite, far from the ferrite/martensite grain boundaries slip, which increases the dislocation density within the ferrite grains, far from the grain boundaries, further increasing the flow stress by forest hardening [8]. It should be noted that to eliminate YPE, free dislocations are needed in the as-produced structure, which increase with increased martensite volume fraction. As the martensite volume fraction increases, YS decreases until a critical martensite volume fraction is reached, where YS is minimized and YPE is eliminated. Hansen and Pradhan [9] showed this by increasing cooling rate during the processing of their DP steel, which increased martensite volume fraction (see Figure 2-7). Further work showed that a minimum of 4% martensite was needed to generate sufficient mobile dislocations to minimize YS and eliminate YPE [10] (see Figure 2-8). However, if the DP steel structure contains bainite only 2% martensite volume fraction is needed to eliminate YPE [11].

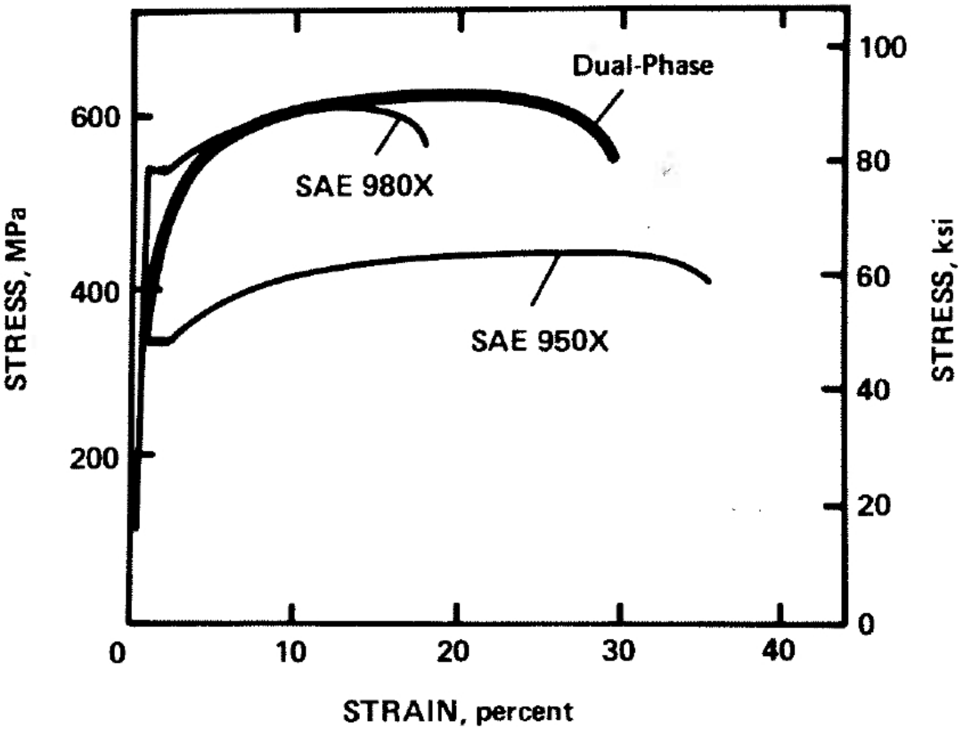

Figure 2-5. Engineering stress-strain curves of a DP and conventional steel with similar ultimate tensile strengths [7].

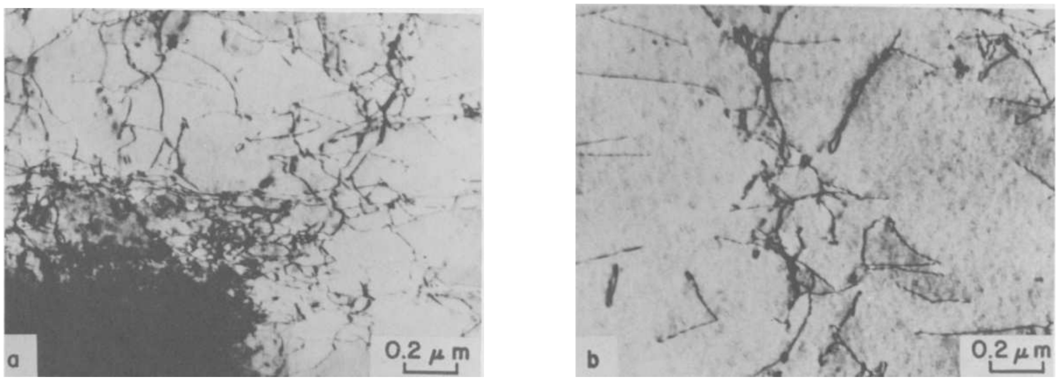

Figure 2-6. TEM micrographs showing the a) high dislocation density adjacent to martensite grains and b) the low dislocation density in the bulk of a ferrite grain in as-produced DP steel [8].

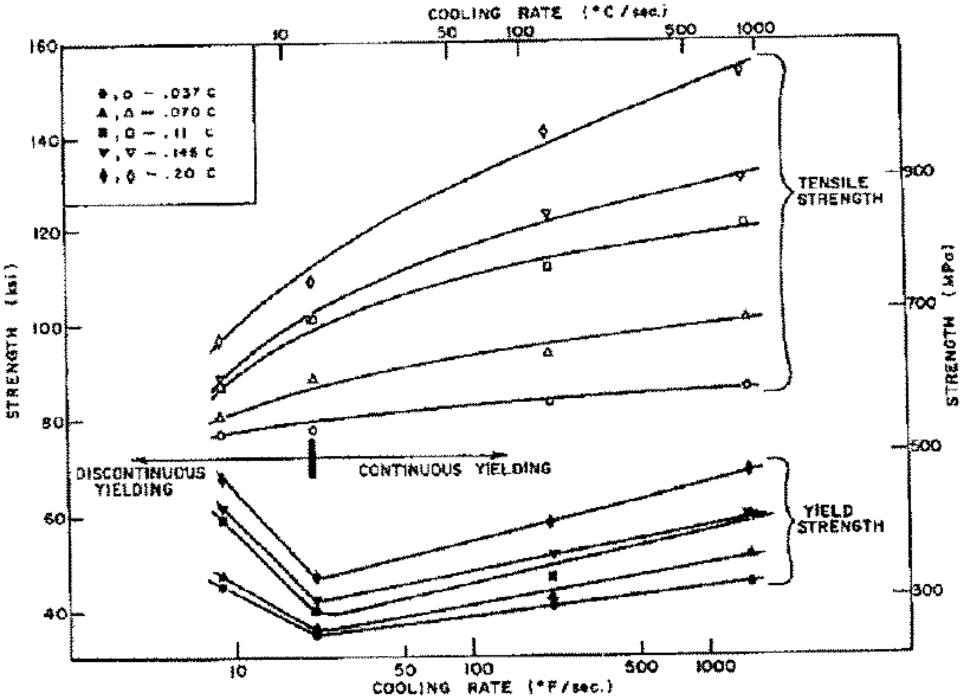

Figure 2-7. UTS and YS of various DP steels as a function of cooling rate [9].

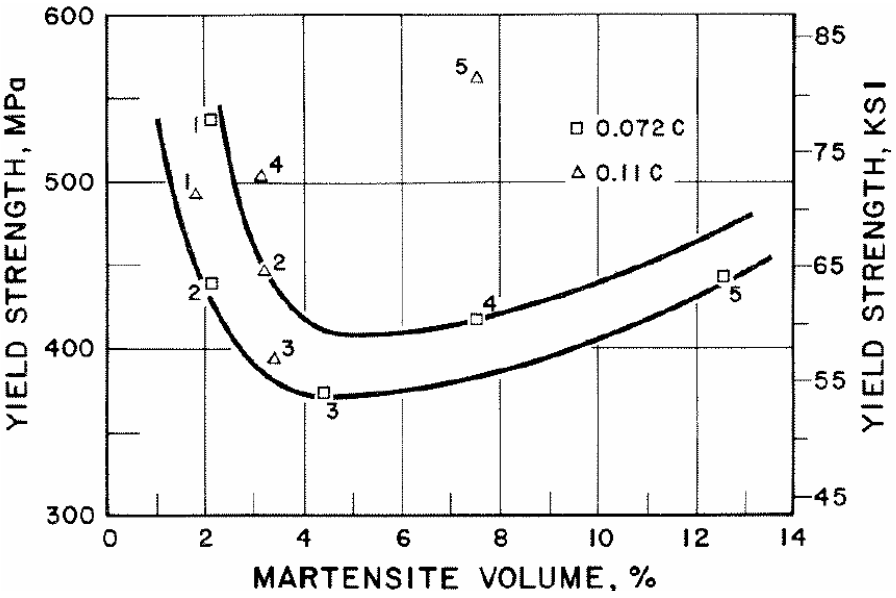

Figure 2-8. Yield strength of DP steel as a function of martensite volume fraction [10].

The relatively high elongation of DP steels when compared to conventional steels of similar UTS is due to their initial high strain hardening rate [7]. According to Considère's criterion for plastic instability, the onset of necking occurs when:

$$\frac{d\sigma_{True}}{d\varepsilon_{True}} = \sigma_{True} \tag{2-1}$$

where σ_{True} is the true flow stress and ε_{True} is the true strain of the material, and their derivative is the strain hardening rate. When the strain hardening rate increases, higher flow stress is required for the onset of plastic instability in a material. From this it follows that if two materials with the same UTS are being compared, one with a low strain hardening rate (material a from Figure 2-9) and one a high one (material b from Figure 2-9), the material with the lower strain hardening rate will have a uniform lower elongation, as its strain hardening rate will intersect with the UTS at a lower elongation value than occurs for the material with the high strain hardening rate (see Figure 2-9).

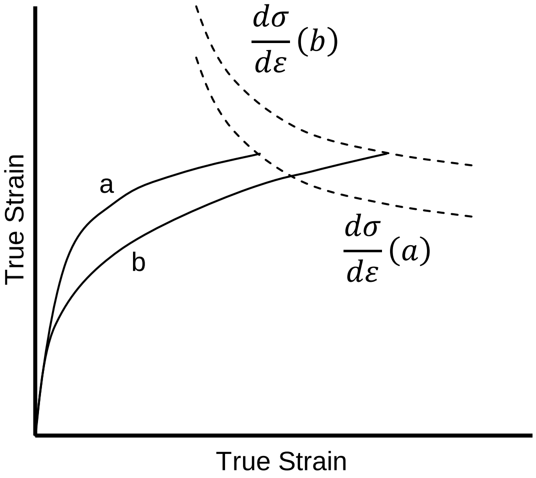

Figure 2-9. Stress-strain curves of two materials with the same UTS but different strain hardening rates.

During plastic flow in DP steels, the change in strain hardening rate can be divided into three stages. Korzekwa *et al.* [8] showed these stages by plotting the strain hardening rate against strain on a log-log scale (see Figure 2-10). During Stage I, when yielding begins (0.001 to 0.005 strain), residual compressive stresses are relieved and back stresses increase due to the mismatch in YS between the ferrite and martensite phases [4,12]. In Stage II, at strains up to about 4%, dislocation density predominately increases at the boundary between the ferrite and martensite. This results in large dislocation gradients between the ferrite centre and the edges that border martensite. During this stage, the rate of decrease in strain hardening rate decreases significantly, allowing the strain hardening rate to remain higher than would be seen in conventional steels at similar strain levels. Once the boundaries between the ferrite and the martensite are saturated with dislocations, dislocations in the centre of the ferrite grains interact, increasing dislocation density in this area. This causes the strain hardening rate to decrease at a rate that is similar to conventional steels [8]. The slowed decrease of strain hardening rate in Stage II is responsible for the initial high strain hardening rate seen in DP steels (see Figure 2-11), leading to higher relative elongation as compared to conventional steels with similar strength levels, as seen in Figure 2-5.

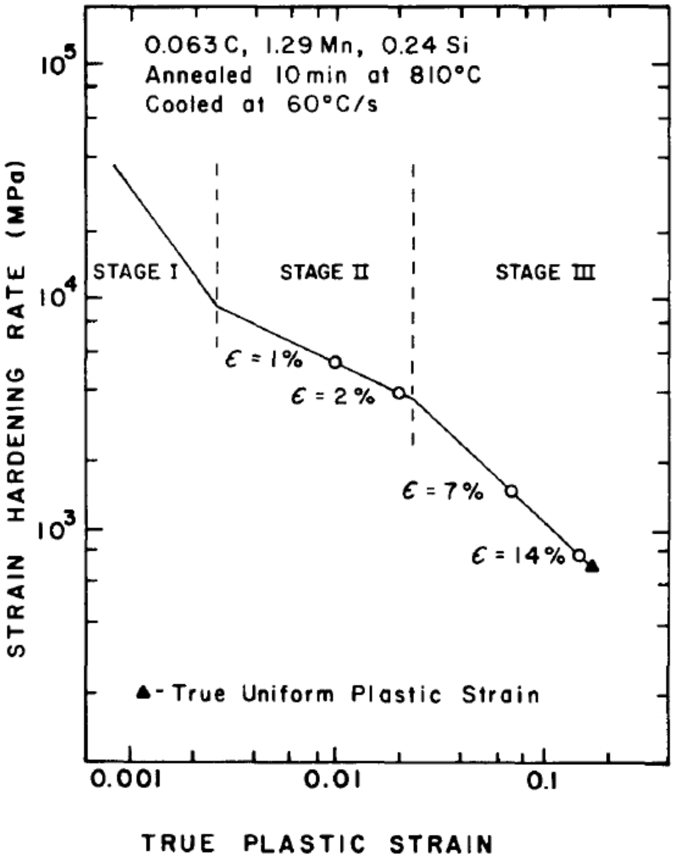

Figure 2-10. Log-log plot of strain hardening rate with increasing strain for a DP steel [8].

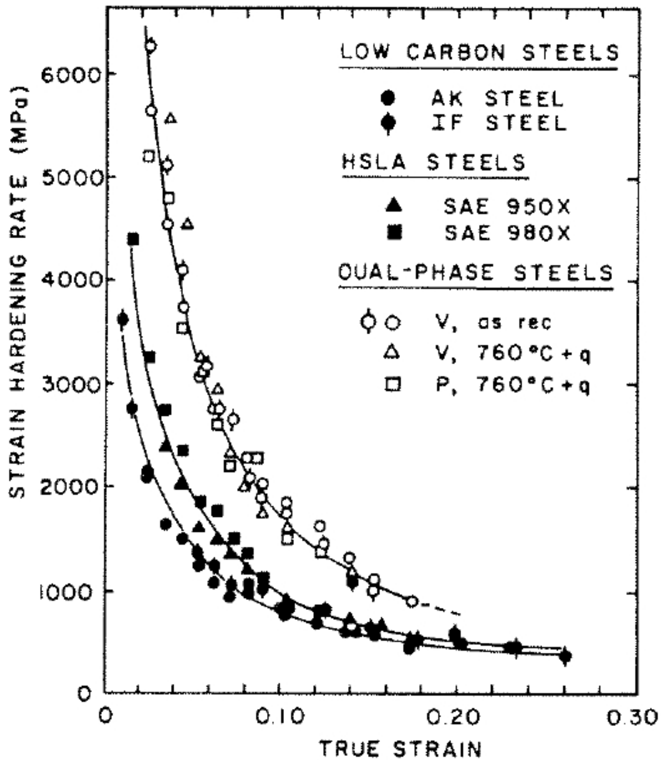

Figure 2-11. Comparison of the strain hardening rates of several steel families [7].

2.2 Welding

Welding is one of the most common joining techniques that automotive manufacturers use to connect steel parts. The vast majority of this welding is done by one of three processes: resistance spot welding (RSW), gas metal arc welding (GMAW), or laser beam welding (LBW). Each of these welding techniques has its own unique applications.

RSW is the most commonly used process of the three, with the average car having about 5000 spot welds [13]. Typically this process is used for assembly welding of sheet steels. In RSW, welds are made by overlapping the sheets of steel to be joined (typically two to four sheets) in a configuration known as a stack-up. The stack-up is then pinched between two copper electrodes with about 2-4 kN of force. After which, a current of 4-8 kA, depending on stack-up thickness and steel properties, is passed between the electrodes, which resistively heats the material between the electrodes. Heat is primarily generated at the sheet-to-sheet interfaces, which melt, forming a molten nugget that is contained within the stack-up. As the heat is generated by a point source between the electrodes, these welds are circular and the weld heat radiates away from the weld nugget (molten area of the weld pool), both through the sheet thickness into the water cooled electrodes, and radially into the base material sheet [14].

GMAW, also commonly known as metal inert gas (MIG) welding, is a higher heat input non-autogenous (requires filler metal) welding process. It is typically used to weld joints connecting higher thickness materials such as those used for frames and axles. GMAW is an arc welding process, where an electric arc is drawn between a consumable wire electrode and the work piece. The heat of the arc melts a pool into the work piece as well as the wire electrode, which incrementally melts and drops into the weld pool, adding filler material to the joint. During GMAW, the weld pool and molten droplets are shielded by a gas delivered co-axially with the electrode. This process has a linear geometry so the heat generated by the welding diffuses linearly away from the weld pool [15].

LBW may be operated over a wide range of heat inputs [16] (the energy imparted to the material to make the weld) in either autogenous or non-autogenous modes [17]. It is typically used for welding laser welded blanks (LWB) and roof ditch welds, however, it is being adopted for more assembly welding applications [18]. Like GMAW, LBW has a linear weld geometry. As LBW is very flexible with respect to heat input, it may be autogenous and is especially well suited for examining temperature dependent transformations during welding.

2.2.1 Laser Welding

Laser welding uses the energy of a laser to melt and fuse the materials to be joined. Heat input during laser welding is between that of RSW and GMAW. Typical cooling rates observed in laser welding range from 200 to 6000℃/s [16].

Lasers produce a monochromatic (single wavelength) and coherent (low dispersion) beam of light. The monochromatic nature of the laser allows it to be used to impart energy to a work-piece as its energy will not change with time because it does not contain multiple frequencies of light (as white light has for example) that may constructively and destructively interfere with each other as a function of distance and time [19]. The highly coherent nature of the laser means that it will have low dispersion allowing it to be highly focused, increasing the power density of the laser.

A laser beam is generated by energizing, or pumping, a lasing media with an energy source. The specific lasing medium depends on the type of laser. Examples of lasing media include: a CO_2, He, N mix as in the case of CO_2 lasers, a Nd:YAG crystal for Nd:YAG lasers, a Yb:YAG fibre in the case of fibre lasers, or a p-n junction in the case of diode lasers. When the lasing media is pumped (energized), the electrons within the media move between their excited and unexcited states releasing quanta of energy in the form of light when the electrons drop to their unexcited state. This energy is trapped within the lasing media by reflective ends forcing the energy to bounce back and forth within the laser cavity. This energy, and the energy released from continued pumping further energizes the electrons within the lasing medium until there is a greater population of energized electrons than non-energized electrons. When this occurs and the reflecting energy interacts with the atoms in the lasing medium, all of the energized electrons fall to their natural energy state at the same time, releasing their energy quanta in sync with each other. This results in an amplified release of energy [19]. This amplified light is then released as the laser beam.

When the beam impinges on the material surface, energy is transferred to the material in one of two transfer modes. If the power density is low and the imparted power is insufficient to increase the material temperature above its vapourization temperature, the laser energy is only absorbed at the material surface and heat is transferred to the rest of the material by conduction. In this case, the weld pool forms radially out from the point of laser impingement and the efficiency of energy transfer between the laser and the work piece is related to the absorptivity of the material surface [17,19,20]. If the power density is sufficient to heat the material temperature above its vapourization point, then the laser will vapourize the material, forming a vapour filled cavity surrounded by molten metal, known as a keyhole. In cases where the keyhole does not penetrate through the workpiece, the beam is trapped within the keyhole due internal reflections and the energy is absorbed along the depth of the cavity and is transferred radially to the surrounding material. In this welding mode nearly 100% of the laser energy is absorbed by the material, making the work piece, in-effect, a black-body [17,21]. However, at automotive sheet thicknesses (0.6-3.0 mm), the process conditions are typically set to ensure that the keyhole penetrates through sheet such that laser power is also lost by transmission through the sheet, some portion of the laser energy will escape through the bottom of the keyhole and will not be absorbed by the work piece.

The ability to weld in both keyhole and conduction modes implies that laser welds may be made with a wide variety of heat inputs. Welds made in conduction mode will require a high heat input to be transferred to the work piece per linear length of weld because much of the heat will flow away from the joint. This results in a very wide, semi-circular weld and HAZ when viewed in the direction of laser beam travel (see Figure 2-12a). Conversely, welds made in keyhole mode will require a very low heat input per linear length of weld, as energy is being absorbed through the thickness of the workpiece. Keyhole mode welding results in a very narrow and deep weld and HAZ (see Figure 2-12b).

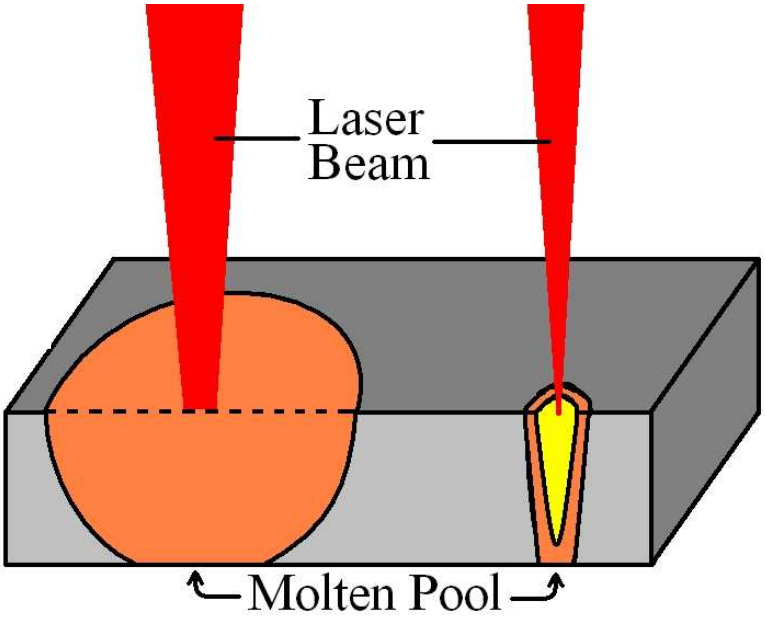

Figure 2-12. Schematic of weld pools formed from laser welding in a) conduction and b) keyhole [20].

2.2.2 Welding Transformations

In the area surrounding all welds there is a non-uniform temperature field. Every local area in the welded sample has its own unique temperature history that is dependent on the heat input and the material thermal properties. The fusion has the highest local peak temperature in the weld area (fusion zone and HAZ), and the local peak temperature then drops with increasing distance from the fusion boundary [22]. The temperature distribution surrounding a weld is controlled by the heat imparted by the welding process and conductive, convective and radiative heat transfer [23]. However, outside of the fusion zone, heat transfer is dominated by conductive heat transfer from the weld towards the colder base material [22]. As conductive heat transfer dominates outside of the fusion zone, the temperature history in the HAZ may be easily modelled analytically. This was first done by Rosenthal [24,25], who derived the temperature field surrounding a line heat source in thin plate, which is applicable to the problem of full penetration welds in sheet steels. When rearranged by Ion *et al.*[26], the instantaneous temperature around the linear heat source (the laser, for example) may be predicted as:

$$T - T_0 = \frac{Q_{net}/_{vd}}{\rho c (4\pi a t)^{1/2}} \exp\left(\frac{-r}{4at}\right) \qquad (2\text{-}2)$$

where T is the instantaneous temperature, T_0 the ambient temperature, Q_{net} the net heat input, d the sheet thickness, v the welding speed, ρ the density of the material, c the material's specific heat capacity, λ the thermal conductivity, a is the thermal diffusivity ($\lambda/\rho c$), r the distance from the heat source, and t is the time after the heat source has passed. The value Q_{net}/vd is the thickness normalized energy per unit length being transferred from the welding source to the material, normally referred to as heat input [27]. From the above description of the temperature field, the temperature surrounding the heat source rapidly increases in front of the source and then exponentially decays after the heat source passes. The heating and cooling rate during welding is the highest along the weld centreline where the temperature gradients are the highest. The heating and cooling rate then decreases with increasing distance from the weld centreline because the local peak temperature decreasing, reducing the temperature gradients during welding. An example of a Rosenthal-type temperature field around a moving source may be seen in Figure 2-13. It should be noted that as the Rosenthal Equation is purely based on conductive heat transfer it cannot accurately predict the temperature in the fusion zone where convection and fluid flow has a significant effect on the temperature field. However, if only the HAZ is considered, the Rosenthal Equation can accurately predict the temperature field.

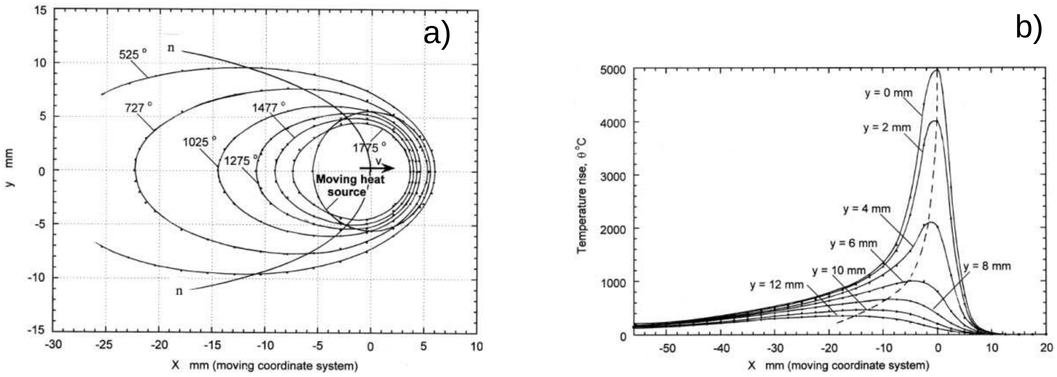

Figure 2-13. Temperature distribution of a Rosenthal type solution as measured a) on the plate surface and b) along the weld centreline [28].

The increased temperature outside of the fusion zone may also result in metallurgical transformations, depending on the local peak temperature. The area where temperatures are high enough to result in solid-state transformations is known as the heat-affected zone (HAZ) [22].

In steels, the peak temperature attained in the HAZ will result in specific metallurgical transformations based on the local phase diagram. As described above, the peak temperature is dependent on the distance from the weld centreline. Furthest from the molten area of the weld, where the peak temperature is between 250ºC and the Ac_1 temperature is the tempered area of the HAZ. Here, the base material is tempered and any existing residual stress are relaxed [22]. Closer to the weld, where the peak temperature reached is between the Ac_1 and Ac_3 temperatures, the microstructure partially transforms to austenite. This austenite, of course, will transform to new low temperature phases when the weld cools. This area of the HAZ is referred to as the partially transformed zone [22]. At temperatures just above the Ac_3 temperature, the local microstructure is entirely austenitized, refining the grain structure. When this area cools, it contains a refined grain structure of low temperature phases. It is referred to as the recrystallized zone [22]. Closest to the fusion boundary where the peak temperatures during welding were the highest, the newly formed austenite grains can grow. When they transform to low temperature phases on cooling, this area has an enlarged grain structure. It is known as the grain growth zone [22]. A schematic of how the final grain structure of these areas correlate to the peak temperature during welding as well as the phase diagram may be seen in Figure 2-14.

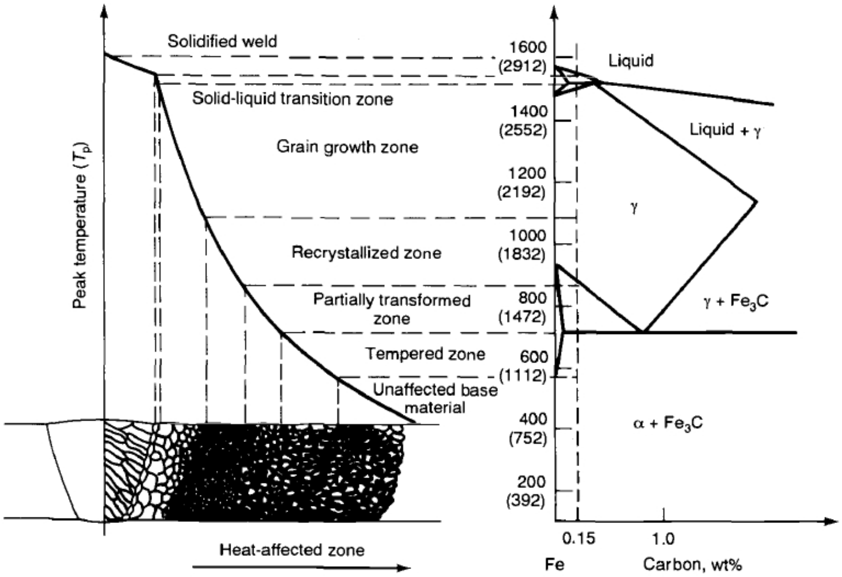

Figure 2-14. Temperature distribution of a typical steel weld and its correlation to the Fe-C phase diagram [22].

2.3 Martensite Tempering

This thesis is concerned with transformations in the tempered area of the HAZ and their effect on the local mechanical properties. Before the effects of tempering on weldment properties are discussed, tempering must be understood.

DP and martensitic steels contain martensite, which is a phase that forms through a diffusionless transformation when austensite is cooled below its martensitic start temperature [6,29]. Typically this is usually done by rapid cooling to minimize the amount of austenite that transforms to ferrite, pearlite and bainite at higher temperatures by diffusion driven transformations. As martensite forms by a diffusionless transformation, it is superstatured with C, where its carbon content is the same as the parent austenite. Martensite has a body-centred tetragonal crystal structure where the c/a ratio depends on its C content [30]. It is very hard and has low ductility and toughness compared to pearlite-ferrite structures and bainite of a similar C content [30]. When martensite is heated, the carbon that is in excess of the solubility limit diffuses from the super-saturated martensite and forms a mixture of ferrite and cementite, as predicted by the phase diagram [31,32]. Figure 2-15 illustrates how the lathe structure of the martensite transforms to a mixture of ferrite and cementite when tempered.

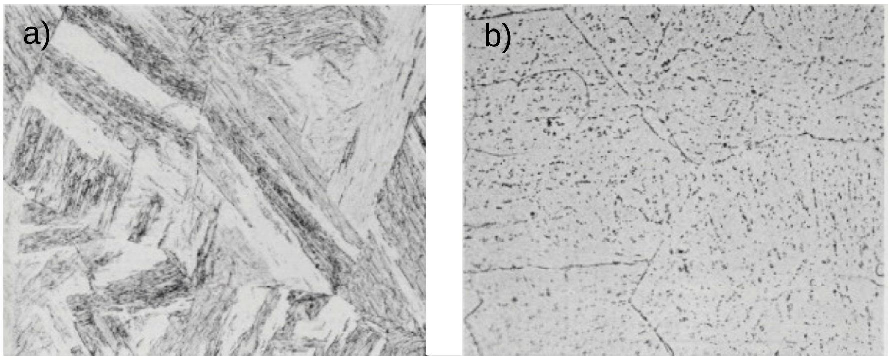

Figure 2-15. Micrographs of a) martensite and b) tempered martensite in a 0.12 wt% C steel [31].

The processes of martensite decomposition, as well as its decomposition products, are a function of both martensite C content and tempering temperature. However, it should also be noted that as tempering is a diffusion process, sufficient time must also pass at each temperature for the transformation to occur. At temperatures between 25-200ºC in martensite with less than 0.2% C, the carbon starts to migrate to dislocation sites in the martensite. In higher C martensites these dislocation sites become saturated with C and ε carbides will start to form [31]. At temperatures between 200-250ºC rod shaped carbides start to precipitate in martensite. Although, these carbides have been identified as cementite[33], it has been suggested that this is the Hägg carbide, a monoclinic carbide with stoichiometry Fe_5C_2, mistaken as cementite because of their similar crystal structures [34]. At 250ºC these rod-shaped particles and the ε carbides transform into spherical cementite (Fe_3C) [31,35]. At temperatures above 600ºC the cementite coarsens [31]. Figure 2-16 summarizes the temperatures at which these processes occur.

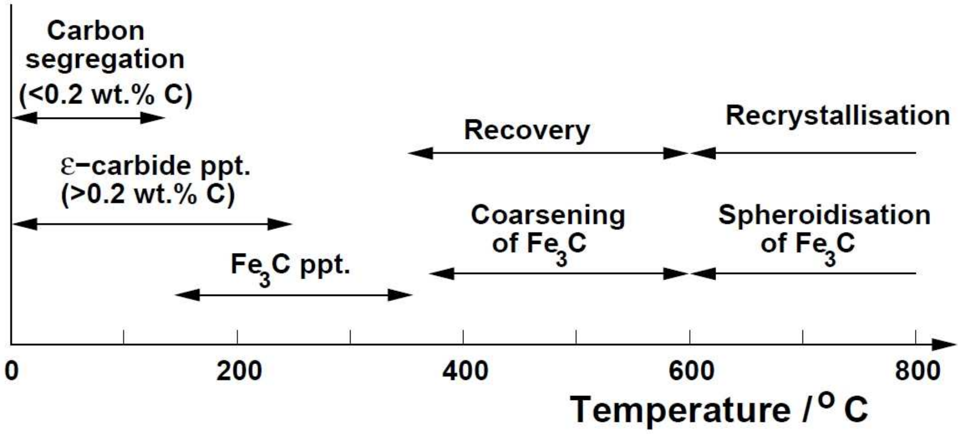

Figure 2-16. Summary of Fe-C martensite decomposition processes as a function of temperature during a one hour heat treatment [36].

At long tempering times there will be sufficient time for substitutional elements such as Cr and Mo to move through the Fe lattice. This will allow for the formation of more complex carbides that include Fe, Mn, Cr and Mo. As such, the stoichiometry of these carbides may include a combination of these elements. Common examples of these carbides include: M_2C (where M is a combination of Fe, Mn, Cr, or Mo) iron carbide which has a hexagonal structure, which may also have a high Mo content, M_7C_3 Cr rich carbides with a trigonal crystal structure, $M_{23}C_6$ Cr rich carbides which has also been observed to contain Mo, V, and Ni, and M_6C, a Mo rich carbide that has an FCC structure [37].

2.4 Softening in the HAZ of DP and Martensitic Weldments

As discussed earlier, temperatures in the outer region of the HAZ are only sufficient to temper the martensite within the material structure. In martensite-containing DP and martensitic steels, the hardness of the tempered region HAZ will decrease below that of the base material, as the martensite within the base material microstructure tempers. Martensite tempering in the HAZ of DP weldments was first noticed in the late 1970's and early 1980's when DP steels were proposed for flash welded wheel rim applications [38-40]. It was observed that after welding these flash welded DP steel joints were failing in the HAZ. These failures were attributed to the observed softening of the HAZ to a hardness below that of the base material hardness (see Figure 2-17), process was named HAZ softening [39,40]. When the microstructure of the weldment was analysed, it was noticed that the softened area of the HAZ corresponded to the area where the martensite had tempered [39,40], as seen in Figure 2-18.

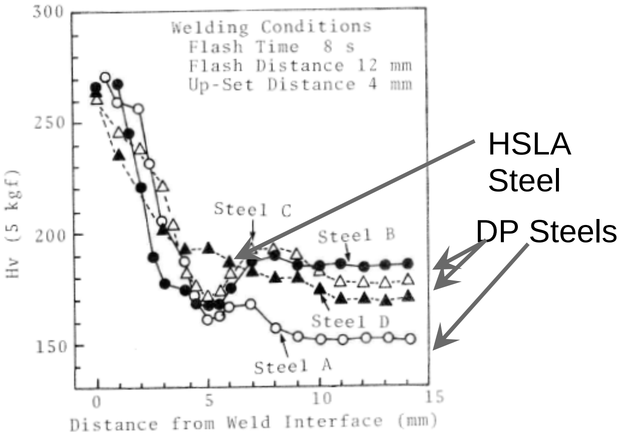

Figure 2-17. Hardness profiles from four steels [39].

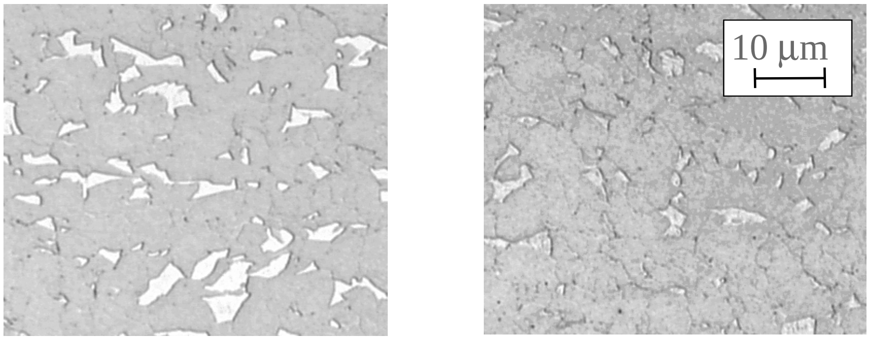

Figure 2-18. DP600 Microstructure in a) the base metal showing ferrite (grey phase) and martensite (white phase) b) and the tempered HAZ showing ferrite and tempered martnsite (light grey speckled phase). Etchant: LePera's Tint [41].

2.4.1 Effect of HAZ softening on mechanical properties

Since HAZ softening was first discovered, studies have shown that it has a profound influence the mechanical properties of the tempered region of the HAZ. Tensile tested weld specimens have clearly shown that strain localizes in the tempered HAZ [42]. This indicates that the observed decrease in hardness below that of the base material corresponds to a decrease in local strength below that of the base metal. These results drove further work where the softened HAZ was simulated by tempering both cold rolled and hot dip galvanized DP steel samples with a Gleeble. When the simulated HAZ samples were tensile tested, it was found that they exhibited a lower YS and UTS than the base material. However, the simulated HAZ samples also showed higher elongation values than the as-produced material [43]. It was also seen that after tempering, the samples exhibited yield point elongation (YPE), which as discussed previously, does not occur in DP steels. An example of the changes in stress-strain curves may be seen in Figure 2-19.

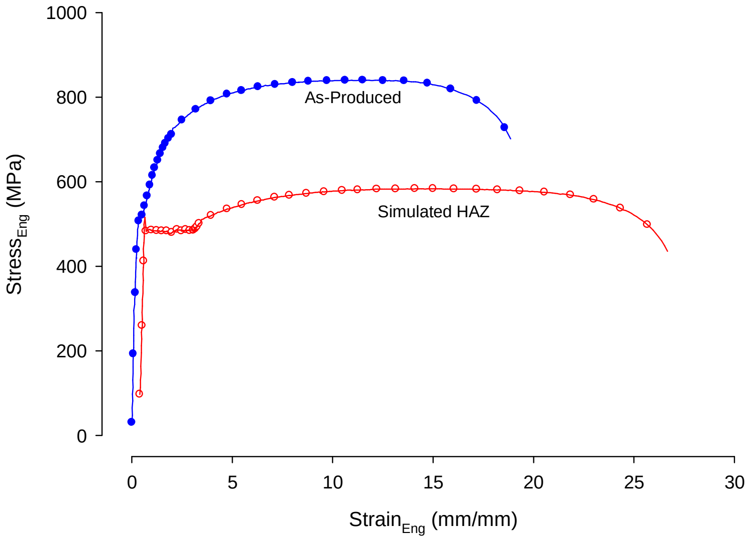

Figure 2-19. Change in stress-strain curves from the simulated tempered HAZ in DP780 [43].

A formability study on DP980 [44] showed that the decrease in mechanical properties of the HAZ decreased the formability of the entire weldment. This work showed that the limiting dome height (LDH) of a

DP980 LWB decreased as HAZ hardness decreased due to strain localization in the HAZ (see Figure 2-20).

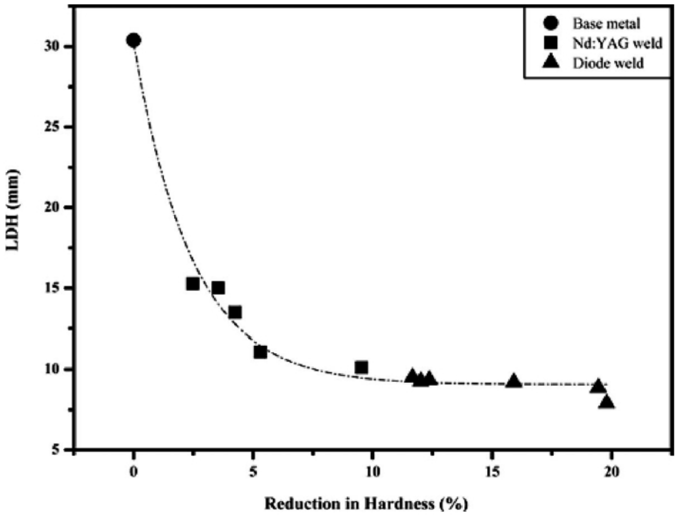

Figure 2-20. Limiting dome height of DP980 laser welded blanks made with a range of heat inputs to generate various amounts of HAZ softening [44].

2.4.2 Effect of martensite content on HAZ softening

It has long been acknowledged that different DP alloys exhibit different levels of softening after welding [27,39,41]. For example, Xia *et al.* [27] showed that softening increased in three DP steels with increasing base material UTS when laser welded with the same welding parameters (see Figure 2-21). However, these researchers then showed that softening increased linearly with increasing base material martensite volume fraction (see Figure 2-22). It was explained that the apparent correlation between HAZ softening and steel UTS was due to the linear increase UTS with martensite volume fraction [4,27]. This was further reinforced by nano-hardness measurements, which showed that softening occurred in the martensite phase, whereas the ferrite hardness did not change after welding [45].

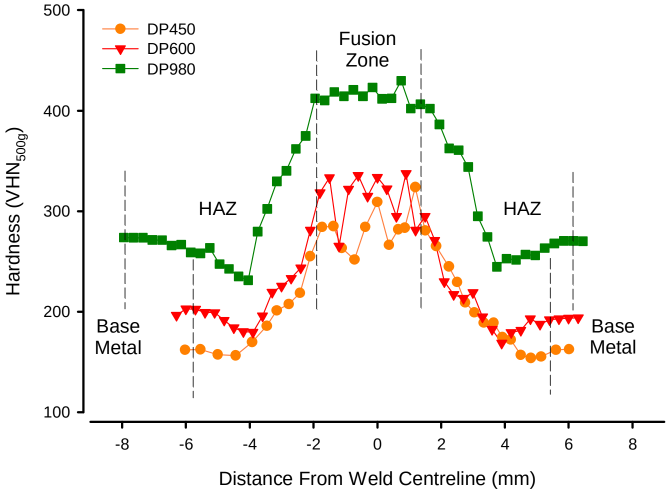

Figure 2-21. Hardness profiles through laser welds in three DP steels [27].

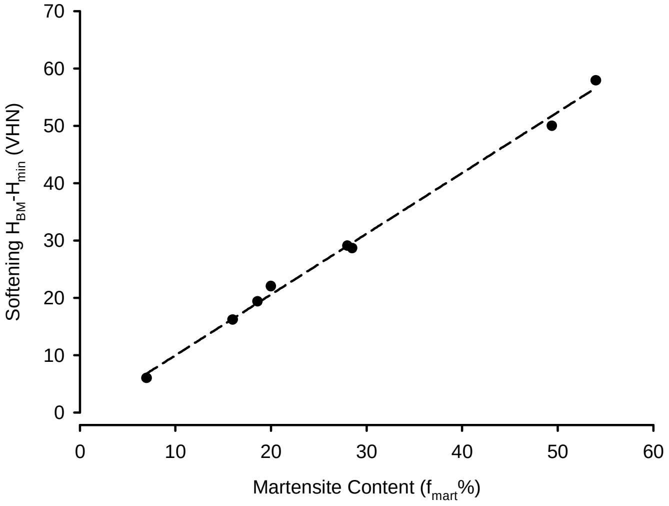

Figure 2-22. Correlation between HAZ softening and DP steel martensite volume fraction [27].

2.4.3 Effect of welding heat input on HAZ softening

Heat input also has a strong effect on HAZ softening. As martensite tempering is a diffusion-driven process [30,46], the progress of this process depends on how long the HAZ is at the tempering temperature. The maximum HAZ softening during welding always occurs at the area of the welding corresponding the Ac_1 isotherm where the local peak temperatures are the highest without inducing an austenitic transformation. When a weld is made with high heat input, it will slowly heat up and cool and it will stay near the peak temperature for a relatively long time compared to a weld made with low heat input, which will heat and cool rapidly [24,25,27]. Therefore, the martensite within the DP structure of a weld made with high heat input will have a longer time to temper, increasing the measured HAZ softening (see Figure 2-23).

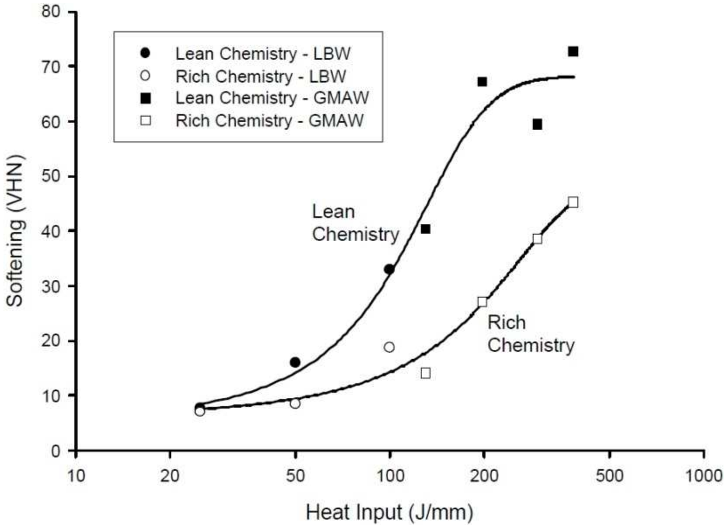

Figure 2-23. HAZ softening observed in two DP600 steels as a function of weld heat input [41].

2.4.4 Effect of DP steel chemistry on HAZ softening

DP and martensitic steels are often alloyed with elements such as Si, Cr and Mo to delay the pearlitic and bainitic reaction when steels are thermally processed using lower quenching rates (such as those during continuous hot dip galvanizing) [41,43]. Cr and Mo are strong carbide formers and Si has a low solubility in cementite, so when relatively high amounts (Cr and Mo > 0.2 wt%, and Si > 0.5 wt%) of the elements are alloyed with the steel, the martensite tempering reaction can be delayed [6,47-49]. When DP steels alloyed with these elements (rich chemistry DP steels) were welded, it was observed that these materials exhibited less softening than DP steels without these alloying additions (lean chemistry DP steels) when welded with similar heat input [41] (see Figure 2-23).

2.5 Martensite Tempering Models

As the understanding of the tempered martensite hardness is very important for tool steel or quench and temper steel applications, much work has been done to model martensite tempering. However, much of this work was done for applications where large sections were heat treated for one hour to change bulk properties. The findings and material constants are not applicable to this work where the time scale of tempering ranges from about 0.1-20 s. However, this being said, the techniques used to model martensite tempering may be still be used to understand tempering in the DP steel weldments.

The literature presents three basic approaches to modelling microstructure and property evolution during tempering. The first approach is modelling nucleation and growth of the carbides evolving from the tempering reaction [50]. Secondly, there has been work done to model tempering by curve fitting the resulting change in mechanical properties [51]. Finally, there is a semi-empirical approach where the change in properties is related to known chemical relationships between the tempering time and temperature [52].

2.5.1 Carbide nucleation and growth models

Martensite tempering may be modelled purely as the nucleation of carbides from the C supersaturated martensite and their subsequent growth. To do this, the nucleation and growth processes must be separated. The carbide nucleation rate may be expressed using classical nucleation theory [50]:

$$I = N_V \frac{k_B T}{h} \exp\left(\frac{-\left(G^* + Q^*\right)}{k_B T} \right) \tag{2-3}$$

where I is the nucleation rate, N_V the number of nucleation sites per unit volume, k_B the Boltzmann constant, h the Planck constant, G^* the activation energy to form the smallest stable particle, Q^* the energy barrier for atoms to pass from the matrix to the particle and T is temperature.

Once the nucleation rate is known carbide growth must be calculated. Carbides will grow by diffusion of C from the undecomposed martensite until all of the martensite has decomposed, and thereafter growth will occur by Ostwald ripening. This is driven by the difference in local solute solubility at the carbide-martrix boundary due to differences in the radii of the various carbides, as described by the Gibbs-Thomson effect [53]. The difference in local solubility is given by:

$$C_R = C_0 + \frac{\alpha}{r_p} \tag{2-4}$$

$$\alpha = \frac{2\sigma_{ST}}{RT} \nu C_0 \tag{2-5}$$

where C_R is the solute concentration in the matrix adjacent to the particle, C_0 the equilibrium solute concentration of the matrix, R the universal gas constant, ν the molar density of the carbide, r_p the particle radius and σ_{ST} is the surface tension at the carbide/matrix interface. The small difference in local solute contents produces a difference in chemical potentials between the large and small carbides, resulting in solute diffusion from the small to large carbides. This results in large carbides to growing at the expense of the smaller ones. Lifshitz and Slyozov [54] described the growth rate by:

$$\bar{r}^3 = \frac{4}{9} D\alpha t \tag{2-6}$$

where $\bar{r}$ is the average cementite particle radius and D is the coefficient of diffusion. For simplicity, the above relation was expressed as the growth from an arbitrary time t_0 as [55]:

$$\bar{r}^3 - \bar{r}_0^3 = k_V(t - t_0) \tag{2-7}$$

Where k_V equals $\frac{4}{9} D\alpha$ and $\bar{r}_0$ is the average carbide diameter at t_0. However, it should be noted that the growth rate described by Eq. 2-6 only relates to spherical particles growing by volumetric diffusion. If particles are growing at grain boundaries they will exhibit cylindrical growth, and growth will be controlled by grain boundary diffusion. In this case, $\bar{r}^4$ increases linearly with time. Grain boundary cementite growth may then be defined as [56,57]:

$$\bar{r}^4 - \bar{r}_0^4 = k_{GB}(t - t_0) \tag{2-8}$$

$$k_{\mathrm{GB}} = \frac{8\sigma_{ST} D_{GB} C_0 \nu^2 \delta}{3k_1 RT} \tag{2-9}$$

where D_{GB} is the grain boundary diffusion coefficient, δ is the grain boundary thickness, and k_1 is a geometrical constant. Lindsley and Marder found that not all carbides within a structure will grow with the same diffusion path. They found that some carbides grew by bulk diffusion, while others will grow by grain boundary diffusion. To describe these cases, Lindsley and Marder combined the growth rates into a single equation relating the average radius to the cementite growth using both mechanisms [55], as follows:

$$\bar{r} \propto \left(k_V t^{3/3} + k_{GB} t^{3/4} + k_{Pipe} t^{3/5}\right)^{1/3} \tag{2-10}$$

where k_{Pipe} is a constant combining the metallurgical factors affecting pipe diffusion along dislocations and is described in [55].

Although modelling the tempering reaction by modelling the nucleation and growth of carbides will give some insight into the system, it is very difficult to link to material properties. As it would be difficult to understand how tempering affects steel physical properties using this model, it is felt the use of this modelling technique is inappropriate to be used to predict the change in properties measured during HAZ softening. The difficulty in linking a nucleation and growth model to physical properties resulted in studies to develop empirical and semi-empircal techniques to model martensite tempering.

2.5.2 Empircal methods modelling hardness changes from martensite tempering

Empirical approaches have also been used to account for the use of all typical elements in steel. Grange *et al.* [51] used this approach and developed tempering diagrams for steels with C contents from 0.08-1.0 wt% 1 hour. They then developed diagrams to account for the influence of typical steel alloying elements on the tempered hardness. The final tempered hardness of the steel was calculated as:

$$H = H_{C,T} + \Delta H_{Mn} + \Delta H_{P} + \Delta H_{Si} + \Delta H_{Ni} + \Delta H_{Cr} + \Delta H_{Mo} + \Delta H_{V} \quad \text{(2-11)}$$

where H is the tempered hardness and $H_{C,T}$ is the tempered hardness of the steel of interest not accounting of the influence of non-carbon alloying additions. $H_{C,T}$ may be found on a master tempering diagram, which accounts for steel carbon content and tempering temperature (see Figure 2-24a). The ΔH terms account for the contribution of the non-carbon alloying elements on the final tempered hardness. Each ΔH term is a function of tempering temperature [51]. Examples of these tempering diagrams may be seen in Figure 2-24. This modelling technique is highly inflexible as it may only be used to predict the hardness of steels tempered for 1 hour, the time used to temper the steels in the dataset, and may not be used to sum incremental temper damage as would be needed during the non-isothermal tempering that occurs during welding. For this reason, this technique is inappropriate to model the process of HAZ softening in welds in DP and martensitic steels.

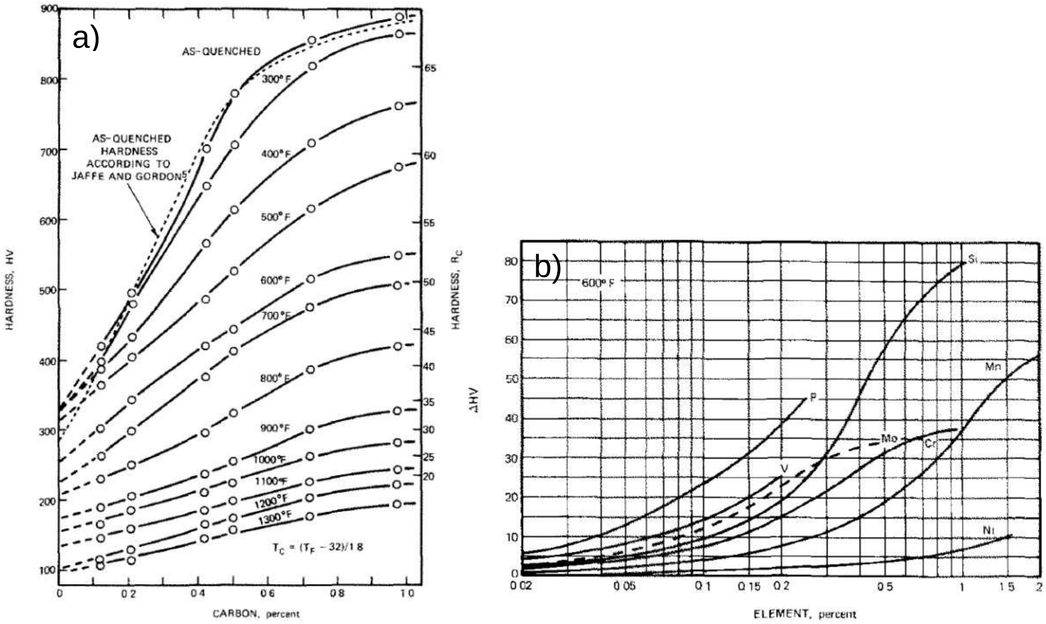

Figure 2-24. Tempering diagrams for a) carbon steel and b) the influence of various alloying elements when tempering at 600ºF [51].

2.5.3 Tempering Parameters

To address the complicated issues associated with modelling the tempering process, Hollomon and Jaffe [52] developed a semi-empirical method to predict softening in carbon steels. They proposed that tempering temperature and tempering time may be combined into a single parameter allowing them to define the tempering cycle by a single parameter instead needing both time and temperature. This combined temperature-time parameter was described as:

$$T\left(c_{H-J} + \log t\right) \tag{2-12}$$

where $c_{H\text{-}J}$ is a material constant related to martensite C content. Hollomon and Jaffe then described the tempering characteristics of several carbon steels by graphing the tempering hardness of each steel against tempering parameter for several tempering cycles with temperatures ranging from 100-700℃ and times ranging from 10 s to 24 hr on a single curve. These diagrams showed tempered hardness can be described by a tempering parameter accounting for tempering time and temperature if the tempering curve is known.

Using a tempering parameter approach has no physical basis in the transformations that occur during tempering as it requires a material specific tempering diagram to be generated before any modelling may be done. This approach will not grant further understanding into the effect of steel chemistry and microstructure on HAZ softening.

2.5.4 Johnson-Mehl-Avrami-Kolmogorov Transformation Model

The final widely used approach to model steel tempering is by employing equations used to model phase transformations in materials based on a semi-empirical modelling approach. This approach was first developed independently by Johnson and Mehl, Avrami, and Kolmogorov [58-62], who developed the equations to model time dependent increase in the volume fraction of a daughter phase from its parent in a process involving nucleation and growth. They proposed that during a transformation there will be three distinct times. First, when the volume is almost entirely made up of the parent phase, there will be nucleation events. At a future time, nucleation will continue and the previously nucleated daughter phase will grow. Finally, after further time has passed and much of the volume has transformed, grains of the daughter phase will impinge on each other, slowing transformation. Figure 2-25 shows these stages and how at long times the transformed product must be accounted for to accurately track the transformed volume.

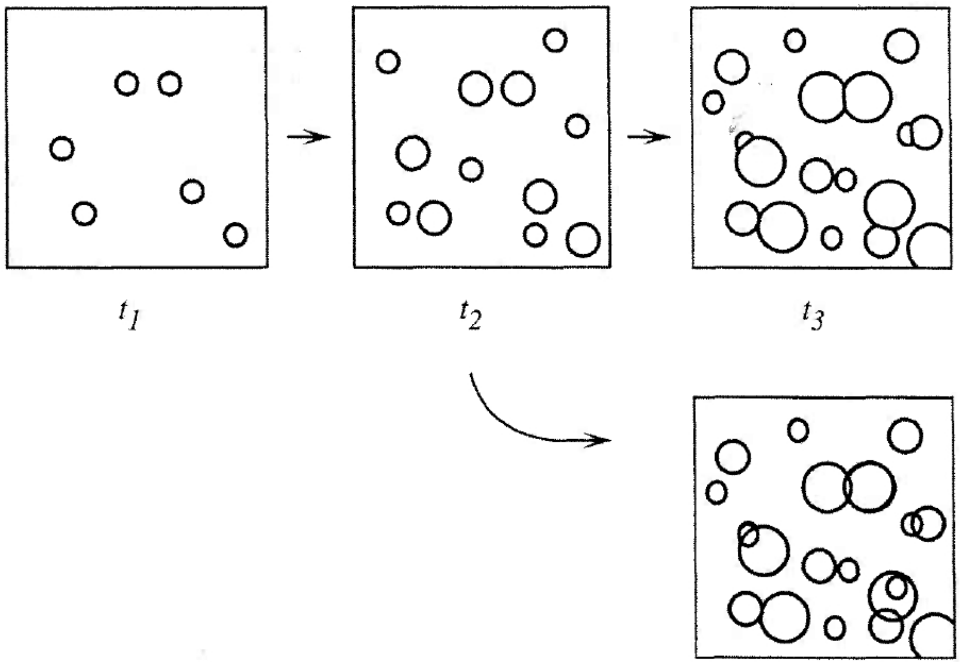

Figure 2-25. Schematic of the nucleation and growth of a daughter phase (β) from a parent phase at three points in time. At long times (t_3) kinetic models may over-predict the transformed volume if previously transformed material is not accounted for [53].

To account for the previously transformed material, the nucleation and growth rate of the daughter phase was scaled by the volume fraction of the remaining untransformed parent phase to determine the actual nucleation and growth in the system. This is expressed as follows:

$$dV^{\beta} = \left(1 - \frac{V^{\beta}}{V}\right) dV_e^{\beta} \tag{2-13}$$

where dV^{β} is the instantaneous volumetric increase in β phase formed, V is the total volume, and dV_e^{β} is the instantaneous volumetric increase in β phase that would form without accounting for the already transformed material. The progress of the reaction may then be calculated by integrating Eq. 2-13:

$$\frac{V^{\beta}}{V} = 1 - \exp\left(-\frac{dV_e^{\beta}}{V}\right) \qquad (2\text{-}14)$$

where V^{β} is the volume of daughter phase formed. In the current work the fraction V^{β}/V, the fraction of the reaction completed reaction, is referred to as ϕ.

The expression, dV_e^{β}/V or the volume normalized transformation rate from Eq. 2-13 depends on the specific system. Johnson and Mehl [59] showed that for systems with spherical particles exhibiting nucleation and growth, dV_e^{β}/V was equal to $\frac{\pi}{3}I{G_R}^3t^4$, where G_R is the particle growth rate. Similarly, Avrami [61] was able to derive that dV_e^{β}/V took on the general form $x_1 ItG_R^{x_2}t^{x_2}$, with the exact form depending on the number of nucleation sites and particle geometry. In the above generalization, x_1 was a geometry dependant constant and x_2 was 1 for rod-like particles, 2 for plate-like particles and 3 for spherical particles. From his generalization, he suggested that dV_e^{β}/V be replaced with kt^n where k represents the kinetics associated with growth and nucleation and n varied depending on the number of nucleation sites and particle shape. Avrami, therefore, concluded that n must either be 1, 2, 3, or 4 depending on the system. This led to the familiar form of the Johnson-Mehl-Avrami-Kolmogorov (JMAK) equation:

$$\phi = 1 - \exp\left(-kt^{n}\right) \tag{2-15}$$

The form of the JMAK equation results in its sigmoidal shape (see Figure 2-26). At short times the reaction is slow because transformation only occurs by nucleation. At intermediate times, the transformation rate increases as particles grow. At long times, the transformation rate slows again, as there is little untransformed material remaining and most of the daughter phase is impinging on itself.

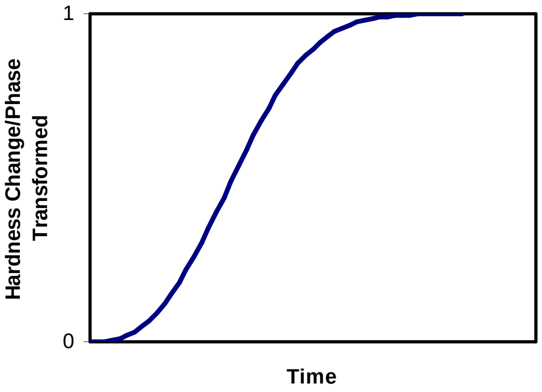

Figure 2-26. General shape of the JMAK equation.

Although developed to describe the kinetics of phase transformations, the JMAK equation has been used by many researchers to describe the progression of tempering [48,47,63-66], as it also progresses in a sigmoidal fashion. However, since the transformations involved in tempering are different that those described by Johnson, Mehl and Avrami, it is expected that the time exponent n will also be different than those predicted by Avrami. In the case of high temperature tempering, where the process starts by the nucleation of cementite, it is expected that *n* will initially be $^{2}/_{3}$, which was predicted by Harper [67]. As the JMAK equation is both flexible and links the underlying metallurgy to the tempering reaction, it is felt that it could be useful to model HAZ softening.

2.5.5 Adaption of Models to Non-Isothermal Tempering

All of the empirical and semi-empirical methods above were designed to be applied to isothermal transformations. However, by its nature, the temperature history during welding is non-isothermal. The curve fitting modelling method presented by Grange et al. [51] cannot be adapted to be used to predict non-isothermal temperature histories, but both the Hollomon and Jaffe [52] and the JMAK equation may be modified to predict tempering progression in non-isothermal heat treatments.

The Hollomon and Jaffe tempering parameter accounts for temperature directly by including it in the parameter, which makes it easy to understand how to account for various temperature heat treatments. Accounting for temperature in the JMAK equation is not as obvious. As the JMAK equation describes transformation kinetics, temperature must be included in the kinetics term. For this reason, *k* from Eq. 2-15 is usually expressed in the form of the Arrhenius equation [65,66] as follows:

$$k = k_0 \exp\left(-\frac{Q}{RT}\right) \tag{2-16}$$

where Q is the process activation energy, R the universal gas constant, T the absolute temperature and k_0 a fitting parameter representing the kinetics at an infinite temperature.

In non-isothermal heat treatments, temperature, and k by extension, is a function of time and is not constant. To determine tempering progression correctly, the tempering model must be integrated over the temperature history of the heat treatment [68]. The literature discusses two methods: a time domain method, also known as the rule of additivity [69], and a temperature domain method [70]. In the time domain method, the non-isothermal heat treatment is divided into several smaller isothermal heat treatments. The progression of the transformation is then calculated for each isothermal heat treatment as [71]:

$$\phi_{i+1} = 1 - \exp[-k_{i+1}(t_i^* + \Delta t_{i+1})^n] \tag{2-17}$$

where ϕ_{i+1} is the progression of the reaction at the end of the current isothermal section, k_{i+1} is k calculated for the current isothermal section, Δt_{i+1} is the duration of the current isothermal section and t^*_i is the adjusted time for the start of the current isothermal section, which is defined as follows:

$$t_i^* = \frac{\ln(1 - \phi_i)^{1/n}}{k_{i+1}} \tag{2-18}$$

where ϕ_i is the progression of the reaction at the beginning of the current isothermal section. Using the time domain method, the total reaction progression for any heat treatment may then be calculated by iteratively summing the contributions from each isothermal heat treatment. This will result in a final transformation progression curve similar to that seen in Figure 2-27.

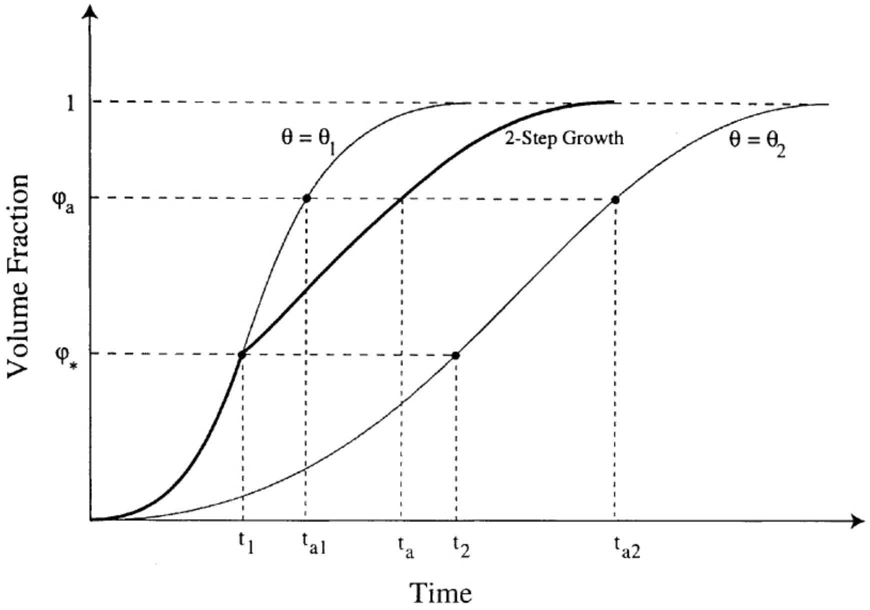

Figure 2-27. Illustration of a JMAK curve calculated from a two-temperature heat treatment using the additive method [72].

In the temperature domain method, the non-isothermal heat treatment is transformed into an isothermal heat treatment at a predetermined temperature. This is accomplished by breaking up the heat treatment into isothermal sections. The duration of each section is calculated so that the progression of the tempering process at the predetermined temperature is equal to the progression of the tempering process at the original temperature [70]. After all of the section times are calculated, they may be summed and the progression of the process may be easily calculated as an equivalent isothermal transformation. An illustration of this methodology may be seen in Figure 2-28.

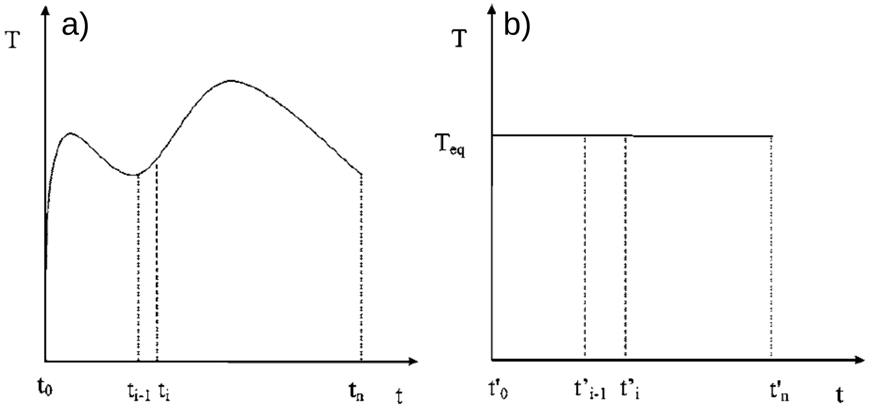

Figure 2-28. Illustration of a) general non-isothermal heat treatment and b) the equivalent isothermal heat treatment calculated using the temperature domain method [70].

Of the two methods the time domain method is significantly more popular in the literature. However, in the case of the thermal histories during welding the temperature domain method may be easier to apply. To apply the time domain method, the tempering progression must be recalculated for every case being examined. Conversely, the temperature domain method may be applied by calculating the percentage difference between the time of the isothermal tempering cycle and the welding cycle, provided peak temperature and material constants are equal. This is true because regardless of the heat input used to make a particular weld, the shape of any two weld thermal histories are similar if the peak temperatures are the same [24,25]. As all of the softening predictions in this thesis are done at the Ac_1 isotherm, the temperature domain method was used to predict the tempering progression during welding, as this reduced the number of calculations to be done.

3 Softening Kinetics in the Sub-Critical Weld HAZ

E. Biro[1,2], J.R. McDermid[3], J.D. Embury[2], Y. Zhou[4]

[1] ArcelorMittal Global Research, 1390 Burlington St., Box 2460, Hamilton, Ont., Canada, L8N 3J5

[2] Dept. of Materials Science and Engineering, McMaster University, 1280 Main St. W., Hamilton, Ont., Canada, L8S 4L8

[3] Dept. of Mechanical Engineering, McMaster University, 1280 Main St. W., Hamilton, Ont., Canada, L8S 4L8

[4] Dept. of Mechanical and Mechatronics Engineering, University of Waterloo, 200 University Ave. W., Waterloo, Ont., Canada, N2L 3G1

3.1 Abstract

Welds in dual-phase steels exhibit heat affected zone softening in which the tempered or subcritical heat affected zone exhibits a lower hardness versus that of the parent material. The rate of this softening reaction with respect to welding heat input was determined for four dual-phase steels by making several bead-on-plate laser welds using a variety of heat inputs and measuring the resulting minimum hardness. The reduction in hardness was then fit to the Avrami equation, enabling a comparison of the relative heat needed to soften each steel. It was found that the heat input required for heat affected zone softening decreased as the C content of the martensite within the dual-phase structure increased. However the presence of carbide forming alloying elements such as Cr and Mo was able to increase resistance to softening.

Keywords: HAZ softening, laser welding, dual-phase steel, martensite tempering

3.2 Introduction

With the implementation of legislation to increase automotive fuel efficiency [1], automakers are seeking a variety of means to reduce vehicle weight. One of the ways that this is being accomplished is by replacing traditional steel grades with advanced high strength steels (AHSS). This allows the steels to be down-gauged, thereby reducing overall part weight [2]. Dual-phase (DP) steels are one of the commonly used AHSS grades being adopted by automakers.

DP steels derive their strength from a composite microstructure comprising ferrite, martensite and bainite. However, as martensite is a thermally unstable phase it will tend to decompose in the heat-affect zone (HAZ), resulting in softening of the local microstructure. This phenomenon has long been recognized and is typically known as HAZ softening [3,4]. HAZ softening is unavoidable in DP steels and occurs in the tempered or sub-critical HAZ where the temperatures experienced during welding do not exceed the Ac_1 temperature of the material [4,5]. As martensite tempering fundamentally changes the DP microstructure, the mechanical properties of this area of the HAZ are characterized by a decrease in the yield and ultimate tensile strength, an increasing in ductility and the return of yield point elongation [6]. HAZ softening may also lead to strain localization and failure in the sub-critical HAZ at stresses below the base material's ultimate tensile strength [5,7].

As HAZ softening can have an adverse effect on weldment strength, much work has been done to characterise this phenomenon. It has been determined that HAZ softening is a very complex phenomenon and is affected by: microstructure martensite content, steel chemistry, heat input and prestrain [6-10]. The potential hardness difference between the softened HAZ and the base material is proportional to the steel martensite content [6,8]. Steel alloy content can decrease HAZ softening by impeding the softening rate [9]. Increasing heat input (increasing ratio of welding power to travel speed), increases HAZ softening as the local temperature of the sub-critical HAZ is elevated for longer times, further advancing the tempering reaction [7-10]. Finally prestrain has been seen to increase the overall magnitude of HAZ softening while increasing the absolute hardness of the softening region [6,9]. Although considerable work has been done to characterise the effects of different material and processing parameters on HAZ softening, there has been no systematic study examining how the chemistry and microstructure of dual phase steels affect martensite tempering reaction kinetics occurring during the short time scales of welding. This study reports on how changing heat input affected the HAZ softening in four DP steels: two DP600s and two

DP780s. The resulting softening curves from welds in all four materials were then compared by normalizing the softening data and the observed softening kinetics are related to the steel metallurgy.

3.3 Methodology

3.3.1 Materials

Experiments were carried out on four industrially produced steels: two DP600 steels and two DP780 steels. These steels were chosen as their microstructures and chemistries were significantly different from each other, allowing a determination of how these factors affected softening kinetics. Both of the DP600s had relatively rich chemistries, being alloyed with higher amounts of carbide stabilizing elements, with one alloyed with Cr and the other alloyed with both Cr and Mo. The DP780s examined represent both rich and lean chemistry philosophies. The rich chemistry was alloyed with C, Mn, Si, Cr, and Mo, whereas the lean chemistry was only alloyed with C, Mn, and Si.

All materials were produced via the conventional industrial processing route of casting, hot rolling and pickling followed by cold rolling. The two DP600 and rich DP780 materials were subsequently processed through a continuous galvanizing line, in which the materials were intercritically annealed, rapidly cooled and dipped in a conventional high Al galvanizing bath. The lean DP780 was processed in a similar manner (intercritical annealing and rapid cooling) through a continuous annealing line, but was not coated with zinc. Detailed characteristics of the as-received (base) steels may be seen in Table 3-1 where the chemistries of the steels are listed in weight percent with the atomic percent of the alloying additions in brackets. Table 3-1 also includes a summary of the microstructure of each base steel, where martensite volume percent and the sum of the martensite and bainite volume percent are listed as f_{mart} and f_{MA}, respectively. Due to C partitioning during the creation of the DP microstructure, the martensite and bainite C content was estimated separately from the steel bulk C content. This was calculated by assuming that the C content of the ferrite phase was 0.02 wt% with the remaining C being partitioned equally between the martensite and bainite phases. Finally the hardenability of the steels were compared using Yurioka's carbon equivalent equation (CE_N) [11]. The microstructures of the as-received base materials are shown in Figure 3-1. It should be noted that limited autotempering was seen in the martensite phase of all of the steels examined (inset micrographs in Figure 3-1). This autotempering likely arose from the lower cooling rates after final thermal processing. However, significant volume fractions of untempered martensite was also present in the microstructures of the DP600 steels (Figure 3-1a) and 3-1b)).

Table 3-1. Details of Base Materials Used in Study. Steel Chemistries Given in Wt Pct (At. Pct).

Grade	DP600	DP600	DP780	DP780
Design	Cr	Cr/Mo	Rich Chemistry	Lean Chemistry
Thickness (mm)	2.0	2.0	2.0	1.5
C	0.10	0.11	0.15	0.10
Mn	1.8	1.6	1.9	1.8
Si	0.14 (0.29)	0.19 (0.38)	0.23 (0.45)	0.33 (0.64)
Cr	0.34 (0.36)	0.22 (0.23)	0.32 (0.35)	0.02 (0.02)
Mo	0.01 (0.00)	0.20 (0.12)	0.11 (0.06)	0.02 (0.01)
CE_N	0.35	0.36	0.52	0.31
f_{Mart} (pct)	2.9	3.5	9.3	17.0
f_{MA} (pct)	27.4	22.8	14.7	17.0
Base hardness (VHN)	194	214	243	249
Martensite C content (calculated wt pct)	0.31	0.41	0.90	0.49

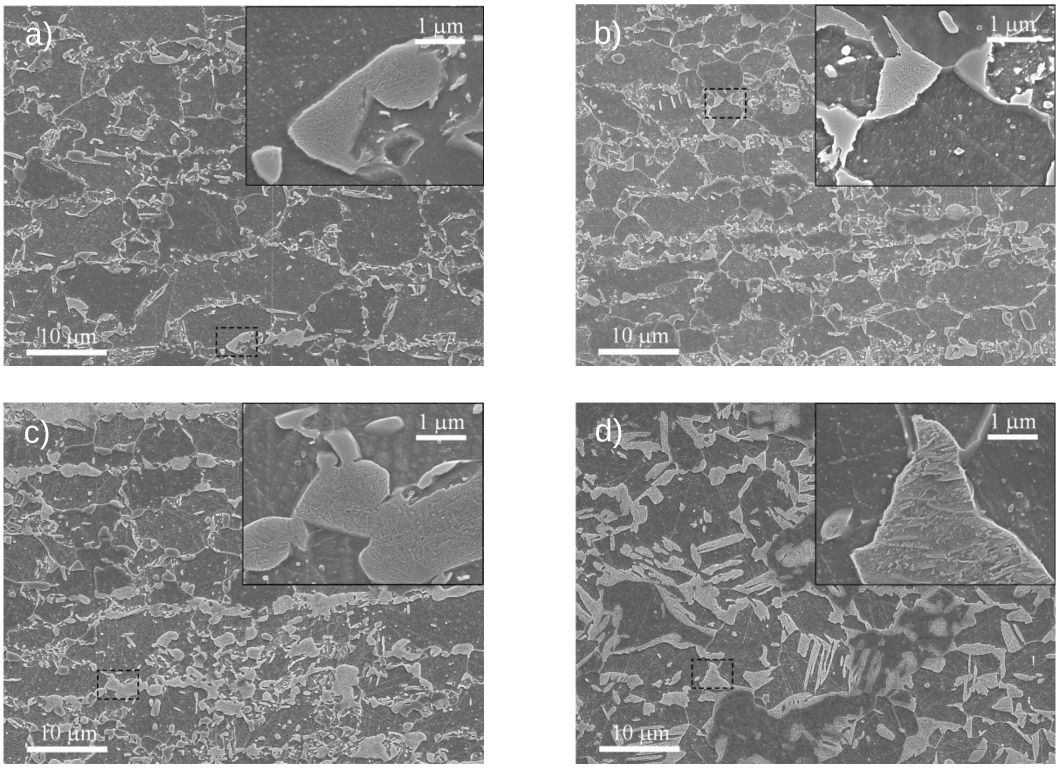

Figure 3-1. Base material microstructures of (a) Cr DP600, (b) Cr/Mo DP600, (c) rich chemistry DP780, and (d) lean chemistry DP780. Increased magnification of autotempered martensite from indicated areas are shown in the micrograph insets.

3.3.2 Welding

All samples were laser welded in the bead-on-plate orientation. High heat input welds (welds made with higher power per unit length) were made using a 4 kW diode laser and low heat input welds were made using an 8 kW CO_2 laser (operated at 80% power) in the case of the DP600s and a 1 kW Yb fibre laser in the case of the DP780s. The characteristics of all of the lasers may be seen in Table 3-2.

Table 3-2. Laser Characteristics Used for Welding.

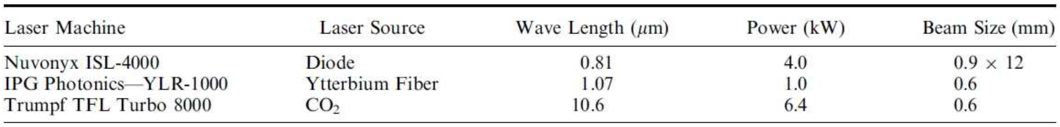

Laser Machine	Laser Source	Wave Length (μm)	Power (kW)	Beam Size (mm)
Nuvonyx ISL-4000	Diode	0.81	4.0	0.9 × 12
IPG Photonics—YLR-1000	Ytterbium Fiber	1.07	1.0	0.6
Trumpf TFL Turbo 8000	CO_2	10.6	6.4	0.6

3.3.3 Measuring Welding Heat Input

Although three lasers were used to create the welds used in this study, the softening results for each experimental condition were compared on the basis of welding heat input. To avoid determining the influence of beam diameter, material absorptivity and welder efficiency, heat input was calculated directly from the HAZ microstructure per the methodology of Xia *et al.* [8]. This technique involves measuring the distance from the weld centreline to both the fusion boundary and to the edge of the intercritical zone, where the peak temperatures reached during welding were the steel's melting point and Ac_1 temperatures, respectively (see Figure 3-2). Using these measurements, the heat input could be calculated using Rosenthal's 2-D solution for weld zone temperature [8]:

$$\frac{Q_{net}}{vd} = \frac{\rho c_p (r_{Ac_1} - r_m)(2\pi e)^{\frac{1}{2}}}{\left(\frac{1}{T_{Ac_1} - T_0} - \frac{1}{T_m - T_0}\right)} \tag{3-1}$$

where Q_{net} is the welding power, v the welding speed, d the plate thickness, the material density, c_p the material specific heat capacity, and T_{Ac1}, T_m, and T_0 are the Ac_1, melting and ambient temperatures respectively.

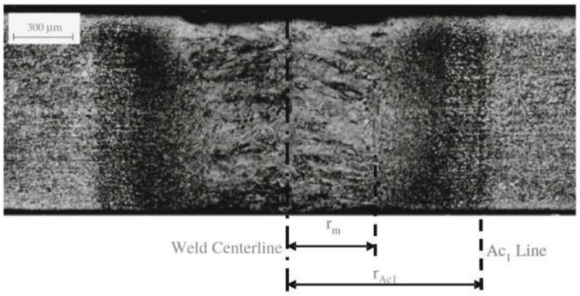

Figure 3-2. Cross section of a typical weld showing the distance from the centreline to the fusion boundary (r_m) and the edge of the intercritical zone (r_{Ac1}) (taken from Ref. 8).

To impart a physical meaning to the heat input, it was converted into a time constant similar to that used by Ashby and Easterling [12]. In the present case, the time constant represents the time to heat a point in the weld HAZ from ambient temperature to its Ac_1 temperature. Therefore, if a weld is made with a high heat input (slow welding speed) it will require significant time for the HAZ to reach the Ac_1 temperature, resulting in a large time constant, and the opposite is true if a weld is made with a low heat input. The time constant, as defined by Xia *et al* [8], is given by:

$$\tau = \frac{1}{4\pi e \lambda \rho c_p} \frac{\left[Q_{net}/(vd)\right]^2}{\left(T_{Ac_1} - T_0\right)^2} \qquad (3\text{-}2)$$

where τ is the time constant and λ the thermal conductivity of the base material. Thus, weld heat input increases as the value of τ increases.

3.3.4 Sample Preparation

All samples for metallurgical analysis were similarly prepared. Transverse cross-sections were cut from each weld well away from both the weld start and crater. Samples were then hot-mounted and polished using standard metallographic techniques to a 1 μm diamond finish using an automatic polishing system (Struers RotoPol-31, Struers RotoForce-4 and a Struers Multidoser, Ballerup, Denmark).

3.3.5 Microhardness

Microhardness measurements were carried out on etched (2% nital) metallographic samples using a Vickers indenter with a 200g load and a 15 s dwell time. All reported measurements are the average of three points measured in the through-thickness direction of the sample cross-section and base material measurements are an average of 9 measurements. The error bars represent one standard deviation of the hardness readings. The trend lines presented are mathematical best fits.

3.3.6 Electron Microscopy

Scanning electron microscopy (SEM) was used to characterise the base material and identify the state of decomposition of the martensite within the HAZ after welding. The microstructure of the materials was revealed by etching the mounted and polished samples with 2% nital for 2 s. All SEM images were taken using a JEOL-7000F field emission SEM with an acceleration voltage of 15 keV.

The decomposition products of the tempered martensite were imaged and identified from extraction replicas with a Philips CM-12 transmission electron microscope (TEM) using an acceleration voltage of 120 keV. Replicas were prepared by etching the cross-sectioned and polished samples with 2% nital for about 1 sec to reveal the weld microstructure. After etching, all areas of the samples with the exception of the sub-critical HAZ were masked with stop-off lacquer. The samples were then carbon coated using vapor deposition. After coating the carbon film was cut and then lifted from the sample surface by immersing the sample in 5% nital. When the films floated from the sample surface they were transferred to a dilute solution of methanol in water, where they were picked up on a 200 mesh Cu TEM grid. All images were taken in bright field mode. Select area diffraction (SAD) patterns were generated using a beam diameter of 700 nm and various camera lengths depending on the pattern. The camera constant may be found on each SAD pattern.

3.4 Results

3.4.1 Softening in DP Steels

For all experimental welds, the minimum weldment hardness was found to be significantly less than the base material hardness (see Figures 3 and 4). The minimum weldment hardness was a function of weld heat input, where softening increased as the time constant (τ) increased (i.e. higher heat input) until a minimum hardness was reached, which matches with past work [8,9]. However, when the hardness/time constant relation for each material pair were overlaid, it was difficult to compare the heat needed to soften the steels as either the initial or the final hardness observed for each material was different. This is to be expected, as all of the materials in this study had different martensite contents, which determines the maximum possible hardness drop [8]. However, if the rate of reduction in hardness for the materials is to be compared, then the curves must be normalized such that they represent the progress of the softening reaction rather than reduction in material hardness.

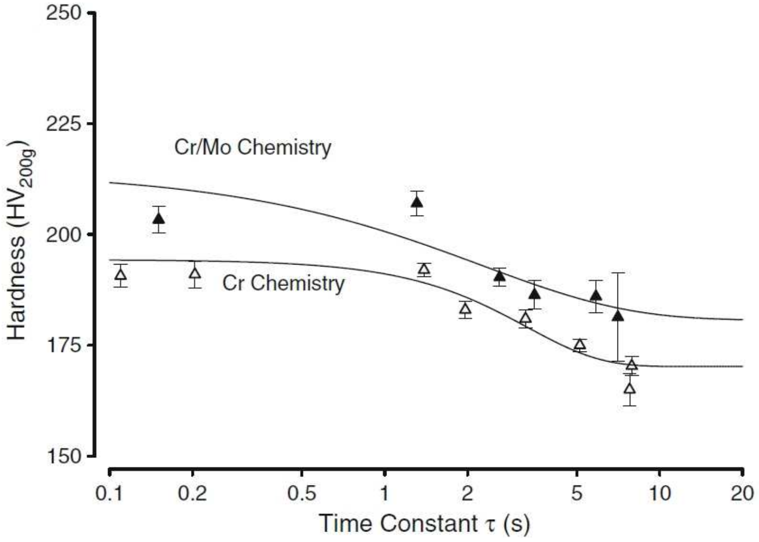

Figure 3-3. Minimum HAZ hardness *vs* time constant for DP600 materials. Note that weld heat input increases with increasing τ, per Eq. [3-2].

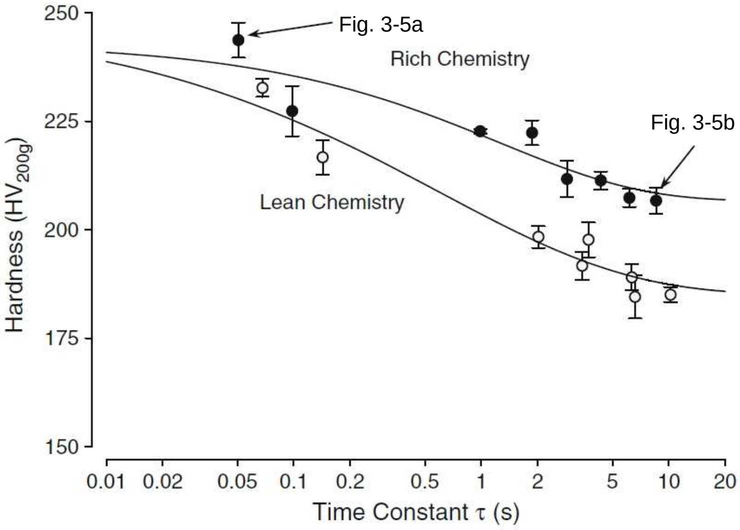

Figure 3-4. Minimum HAZ hardness *vs* time constant for DP780 materials and the time constants of the welds examined in Fig. 5. Note that weld heat input increases with increasing τ.

3.4.2 Decomposition Products in Low and High Heat Input Welds

Before a transformation may be applied to the hardness data, the martensite decomposition products formed in the HAZ of the welds as a function of weld heat input and alloy chemistry needs to be characterised to determine if it was the same for all experimental conditions. Under SEM imaging it was revealed that not all of the martensite decomposed immediately. After welding with low heat input, a patchwork of martensite decomposition was seen within some martensite grains (see Figure 3-5(a)). When the heat input was high enough, massive decomposition of the martensite throughout the microstructure was observed (see Figure 3-5(b)).

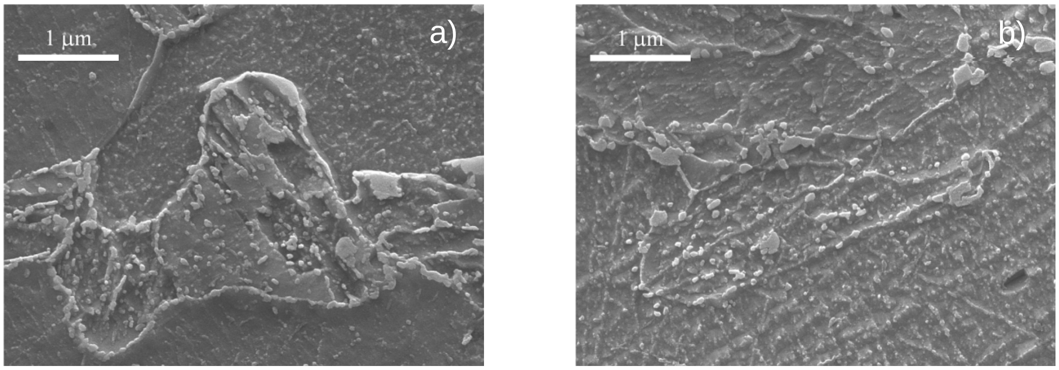

Figure 3-5. Martensite phase found in the softened HAZ from a) low and b) high heat input welds from the lean DP780 steel.

TEM examination of the decomposition products using extraction replicas revealed that the martensite decomposition products from all conditions were irregularly shaped (see Figure 3-6 and 3-7). In general, the particles found in the HAZ of welds made with high heat input were significantly larger (via 95% confidence intervals of the image analysis results) than those found in the HAZ of welds made with low heat input. SAD patterns obtained from these particles revealed that the decomposition products were cementite [13]. This matches results by Jung *et al.* [14] who observed that during non-isothermal tempering of martenistic steels, although ε carbides formed at low temperature, only cementite remained after tempering near the Ac_1 temperature. From the TEM observations of the replicas on the two DP780s and Jung *et al.*'s [14] results, it is assumed that cementite will be the only martensite decomposition product present in the subcritical HAZ of the DP600 welds after welding, as the latter steels were similar to the rich DP780 steel in alloying philosophy and similar to the lean DP780 in CE_N.

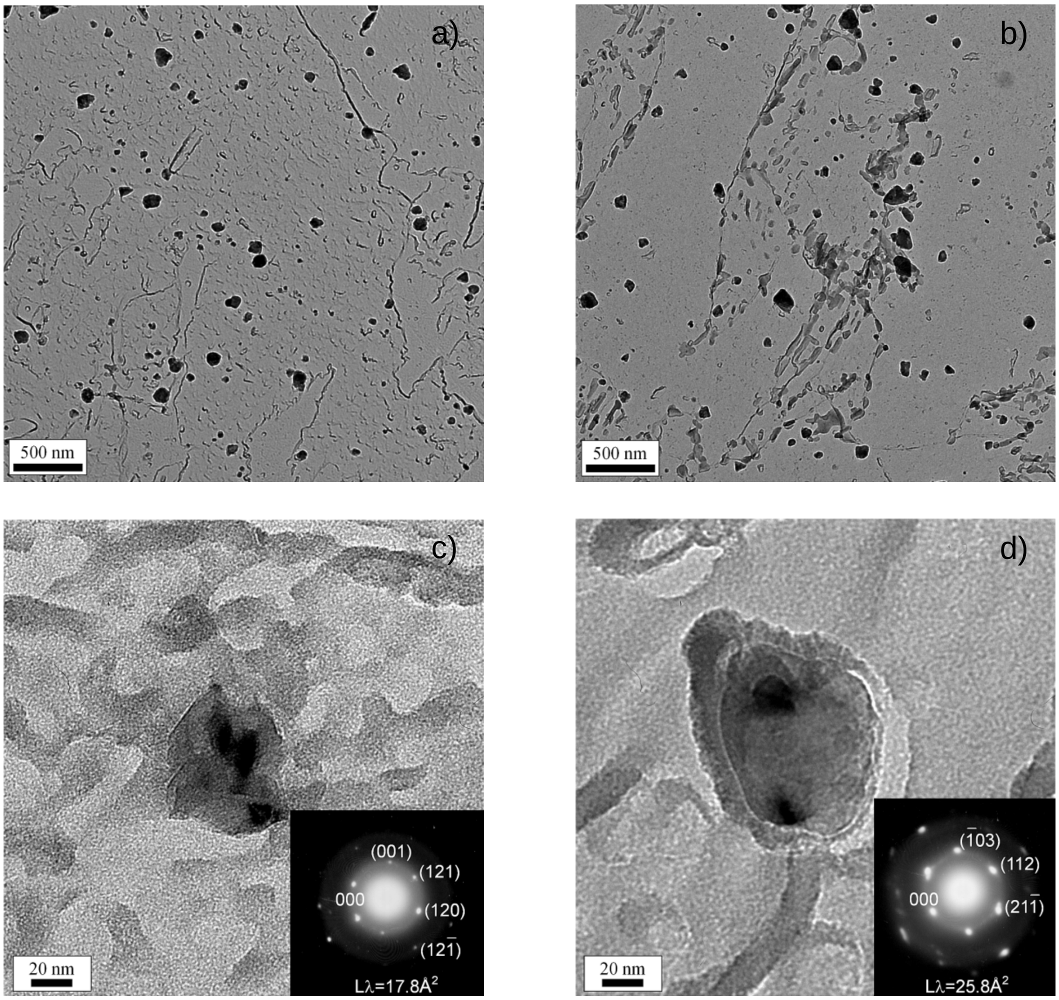

Figure 3-6. TEM images of cementite particles found in the sub-critical HAZ of the lean chemisty DP780 welded with a) low and b) high heat input as well as examples of individual particles and their SAD patterns from the welds made with c) low and d) high heat input.

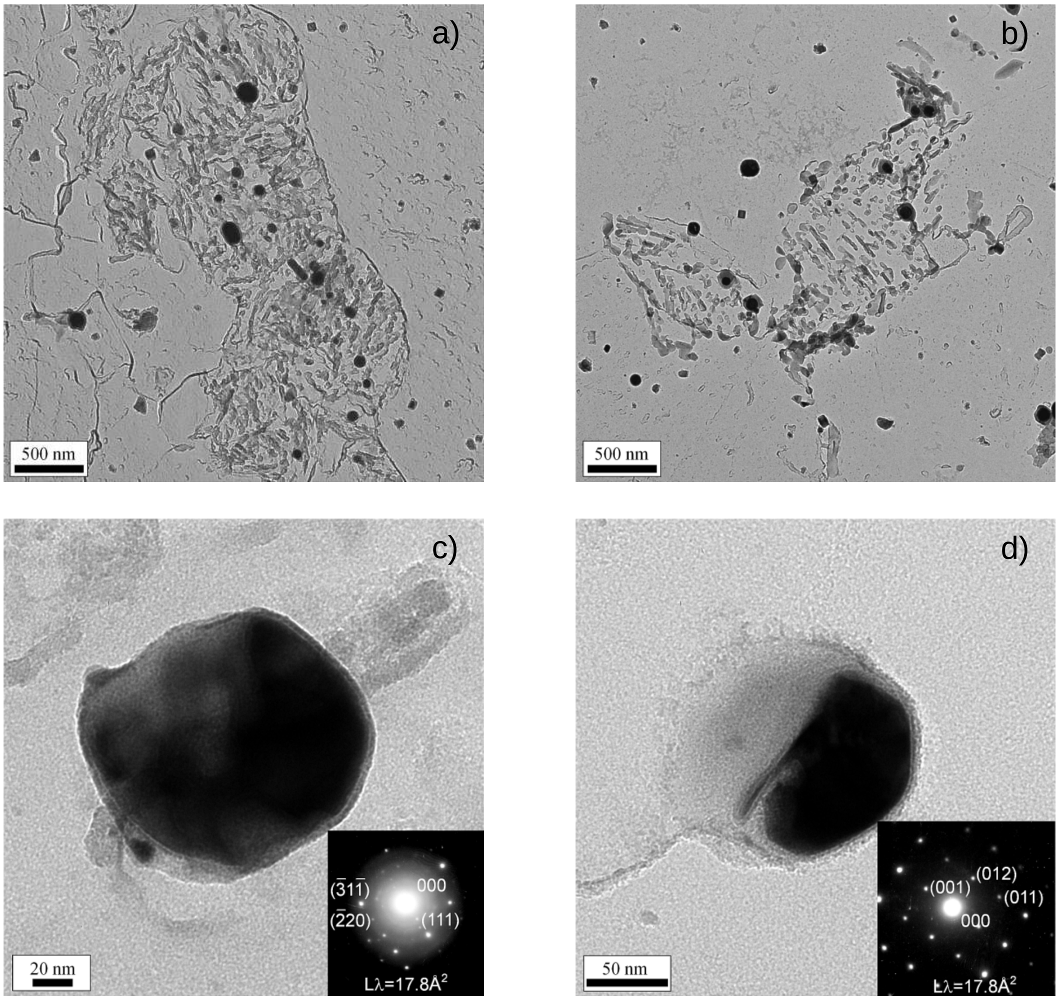

Figure 3-7. TEM images of cementite particles found in the sub-critical HAZ of the rich chemisty DP780 welded with a) low and b) high heat input as well as examples of individual particles and their SAD patterns from the welds made with c) low and d) high heat input.

3.5 Discussion

3.5.1 Comparison of Softening Kinetics

The analysis of the softened HAZ revealed that the martensite within the base material structure decomposed to cementite. Although it is possible that ε carbide formed during the initial stages of heating, they were not observed in the sub-critical HAZ after welding. This is consistent with the work of Wang *et al.* [15] who modelled martensite decomposition and found that ε carbides grow and dissolve quickly and showed that cemenite formation and growth may be modelled independently of ε carbide. Furthermore, it was seen in the present results that the martensite did not immediately decompose after the material reached the Ac_1 temperature. Instead, when the material was tempered for short times the martensite partially decomposed and this transformation progressed as the time that the weld was held at the tempering temperature (τ) increased. Finally, after the carbide particles formed they grew with increasing tempering time until the martensite was fully decomposed. This pattern of local nucleation, growth and saturation of a transformation product may be well described by the Avrami equation of transformation [16]

$$\phi = 1 - \exp\left(-kt^n\right) \tag{3-3}$$

where ϕ is volume fraction of martensite that has been transformed, k is a fitting parameter representing the energy barrier to the tempering transformation, t is the tempering time (τ is used in this study), and n is a fitting parameter related to the rate of the transformation.

To describe martensite decomposition using the Avrami equation, a parameter ϕ was defined such that ϕ equals zero when the material is in its base state (*i.e.* the as-received base materials, as described in Figure

3-1 and Table 3-1) and is defined as being equal to one when the material has been fully tempered or is at its minimum hardness, as was done by Mittemeijer *et al.* [17]. ϕ was calculated using the following equation:

$$\phi = \frac{H_{Base} - H}{H_{Base} - H_{\min}} \tag{3-4}$$

where H_{Base} is the hardness of the base metal, H_{min} is the minimum hardness value measured in the HAZ for a given material, and H is the sample hardness. The use of the ϕ parameter is based on the assumption that the material hardness is an average of the hardness of the individual phases weighted by their respective volume percentages in the steel microstructure. Thus, the change in hardness observed in the sub-critical HAZ is assumed to be due only to the changing volume percentages of the martensite, ferrite, and tempered martensite phases as the material tempers. However, it may also be possible that during tempering the high internal stresses present in the DP steels are relieved. If this is the case, then changes in internal stresses will also be incorporated into the ϕ parameter. This must be confirmed with further work.

3.5.2 Fitting Softening Kinetics to the Avrami Equation

When all of the hardness data was transformed using Eq. [3-4], the softening kinetics of the DP600 and DP780 steels could be readily fit to the Avrami equation. The fits for all four steels were good, having adjusted r^2 values ranging between 0.81-0.92 (see

Table 3-3). It is also interesting to note that the *n* parameter that was fit to the four materials was much lower than the range of 3 to 4 predicted by Avrami for pure particle nucleation and growth of a polyhedral particle [16]. However, it should be noted that the value of the *n* parameters for the DP780 materials were similar to those measured by Luppo and Ovejero-García [18] and Roberts *et al.* [19] who measured this parameter as 0.36 and 0.3, respectively. Roberts *et al.* [19] showed that if particle nucleation does not occur as Avrami described, but instead if the martensite phase decomposes as a receding front behind which the daughter products are formed (low carbon martensite and ε carbide in their case, and ferrite and cementite in the present case) then the *n* parameter should be approximately 0.5, which matches the value measured for the DP780 steels. This appears to correlate with the observations in this study, where martensite decomposed in a patchwork instead of at random and evenly distributed nucleation sites. However, in the case of the DP600 steels, where the n parameter was measured to be 1.6 and 1.7, it is possible that less of the martensite within these steels was autotempered, and there were nucleation sites available for the formation of cementite in the martensite within the as-received microstructure. So, cementite formed as a result of both the recession of the martensite front and nucleation created new cementite particles, resulting in an increase of the *n* parameter from that of the DP780 steels.

Table 3-3. Fitting constants for the Avrami Equation.

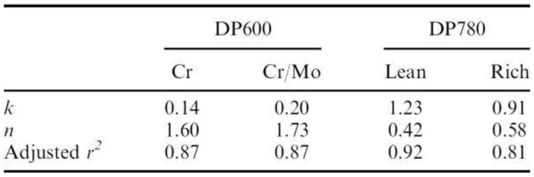

	DP600		DP780	
	Cr	Cr/Mo	Lean	Rich
k	0.14	0.20	1.23	0.91
n	1.60	1.73	0.42	0.58
Adjusted r^2	0.87	0.87	0.92	0.81

Now that the hardness data has been normalized with the ϕ parameter and fit to the Avrami equation, the progression of the tempering reactions for the four steels may be compared. It may be seen that the Cr/Mo DP600 softens at slightly shorter time constants than the Cr DP600 and the lean chemistry DP780 softens more rapidly than the rich chemistry DP780 (see Figure 3-8 and 3-9). When the curves from both steel grades are overlaid, general observations may be made on the softening kinetics as a function of overall steel chemistry (see Figure 3-10). Although it has been suggested in the past that a high carbon equivalent indicates resistance to softening [9], this was not observed in the present case. Figure 3-10 shows that the lean DP780 chemistry had the lowest resistance to softening, although its carbon equivalent was similar to the two DP600s (see Table 3-1), and the rich chemistry DP780 softened at a rate between that of the lean DP780 and the DP600s despite its CE being the highest of the materials examined (Table 3-1). However, with the exception of the lean DP780, the resistance to softening increased as the martensite C content decreased.

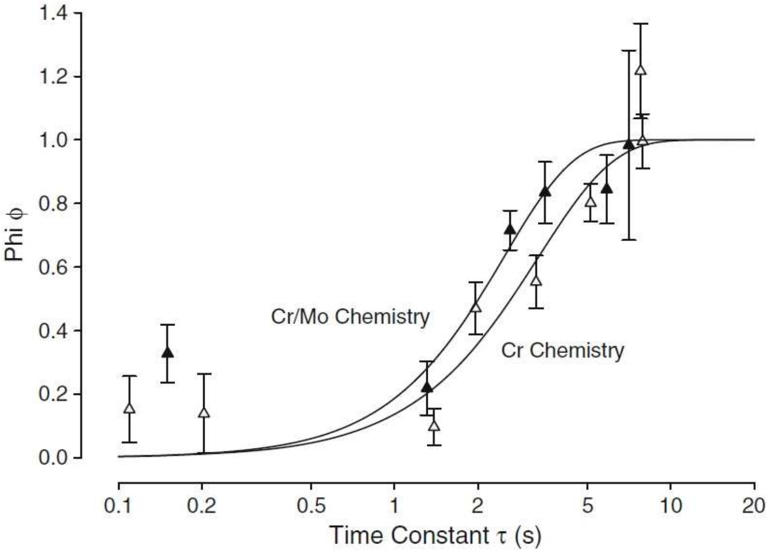

Figure 3-8. Progression of martensite decomposition in DP600 steels with increasing heat input.

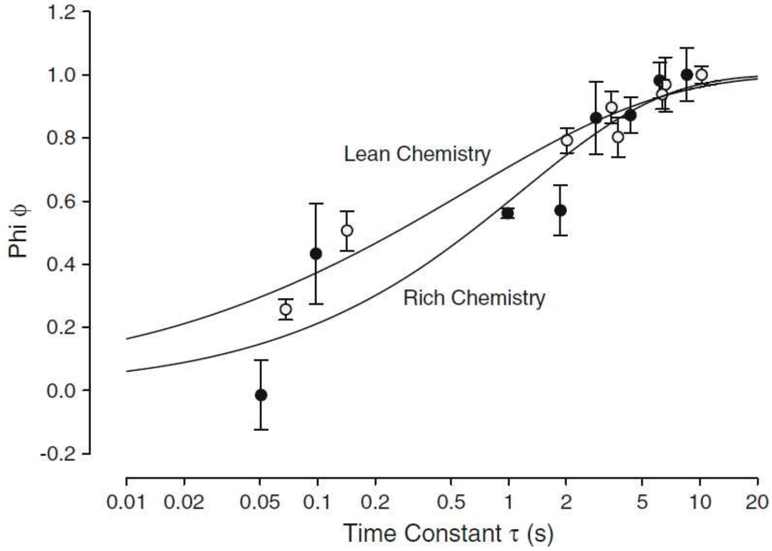

Figure 3-9. Progression of martensite decomposition in DP780 steels with increasing heat input.

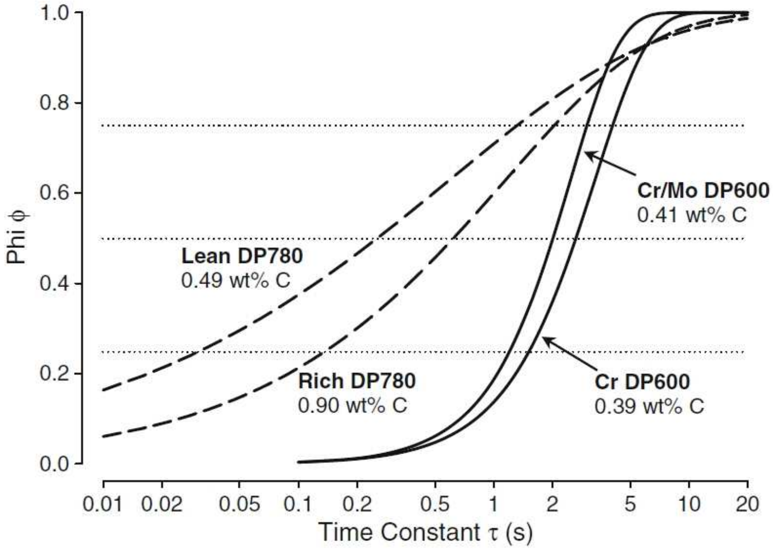

Figure 3-10. Comparison between the softening kinetics of all steels examined. The compositional information is the calculated martensite C content, per Table 3-1.

The effect of steel chemistry on the rate of martensite decomposition may be further illustrated using the *k* parameter from Avrami equation (equation (3)), where it can be seen that an increase in *k* results in a decrease in the time to initiate the tempering reaction. Thus, *k* can be thought of as representing the energy barrier to initiate HAZ softening, where higher values of *k* indicate a low energy barrier and relatively easy initiation of HAZ softening and visa versa for lower values of *k*.

When the *k* parameters for the steels were compared, it was seen that *k* was proportional to the martensite C content for the three steels alloyed with carbide forming elements, with the lean DP780 *k* value being considerably above this curve (see Figure 3-11). This disagrees somewhat with the results of Roberts *et al.* [19] who showed that *k* is only a function of martensite C content. However, in that study none of the steels were alloyed with carbide forming elements. In the present case, Figure 3-11 indicates that martensite decomposition is a function of both martensite C content and alloying chemistry, unfortunately as only one steel was alloyed without Cr and Mo we cannot know the relationship between *k* and martensite C content for this steel family without testing more materials.

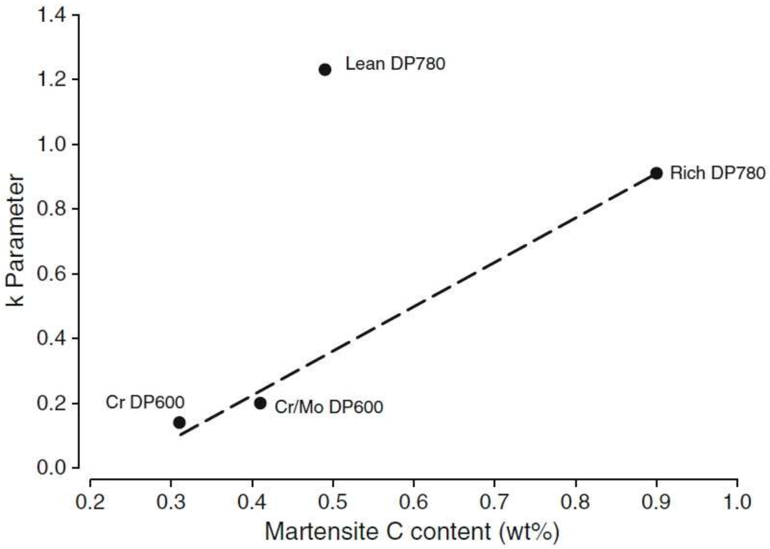

Figure 3-11. Avrami *k* parameter *vs* martensite C content for all experimental steels.

It is logical that martensite C content controls the rate of the tempering reaction, as tempering is a diffusion driven process where the C within the martensite diffuses into the surrounding material. As the martensite C content increases, the driving force for this reaction increases, speeding the tempering transformation. It is thought that the lean chemistry DP780 does not fit this model because it was alloyed without strong carbide formers such as Mo and Cr. These additions stabilize the martensite [20] retarding the tempering reaction and resulting in the lean DP780 tempering with much lower welding heat when compared to materials with similar martensite carbon content.

3.6 Conclusions

Bead-on-plate welds were made on two DP600 and two DP780 steels with different chemistries. After welding, the hardness of the sub-critical zone was measured and the following can be concluded about the heat-affected zone (HAZ) softening observed:

1. The minimum HAZ hardness for all of the steels decreased as heat input increased until a minimum value was observed. Further increases in heat input had no further effect on subcritical HAZ hardness.
2. The martensite decomposition product in the sub-critical HAZ for all welds was cementite.
3. Because HAZ softening by martensite tempering is a function of cementite nucleation, growth and saturation, HAZ softening kinetics could be fit to the Avrami equation.
4. The heat required for HAZ softening decreased as the martensite C content increased in steels with similar amounts of carbide forming

alloying additions (ie. Cr and Mo). This is consistent with diffusion mechanism driving martensite decomposition.

5. The lean DP780 alloyed without Cr and Mo softened with lower heat input than its martensite C content would suggest when compared to the other steels. This was attributed to its lack of carbide forming alloying elements that stabilized the martensite, thereby slowing the tempering reaction.

3.7 Acknowledgements

The authors would like that the staff of the Canadian Centre for Electron Microscopy and Dr. X. Wang who assisted with the preparation and the analysis of the TEM images and SAD patterns. The authors also wish to thank ArcelorMittal for providing the experimental materials used and for permission to publish this work.

3.8 References

1. *Federal Register*, 2009, Vol. 74, pp. 49454-49789.
2. W. Gan, S.S. Babu, N. Kapustaka, R.H. Wagoner: *Metall. Mater. Trans A*, 2006, Vol. **37A**, pp. 3221-3231.
3. S. Hashimoto, S. Kanbe, and M. Sudo: *T Iron steel I Jpn*, 1981, vol. 21, pp. B-497.
4. N. Yamauchi, T. Taka, K. Kunishige, and N. Nagao: *T Iron steel I Jpn*, 1982, vol. 22, pp. B-107.

5. T. Taka, K. Kunishige, N. Yamauchi, and N. Nagao: *ISIJ Int*, 1989, vol. 29, pp. 503-510.
6. E. Biro and A. Lee: *Sheet Metal Welding Conference XII*, AWS, 2006, Livonia, MI, May 9-12, paper 7-1.
7. P.K. Ghosh, P.C. Gupta, Ramavtar, and B.K. Jha: *Weld J.*, 1991, vol. **70**, pp. 7s-14s.
8. M. Xia, E. Biro, Z. Tian, Y.N. Zhou: *ISIJ Int*, 2008, vol. 48, pp. 809-814.
9. E. Biro and A. Lee: *Sheet Metal Welding Conference XI*, AWS, 2006, Sterling Heights, MI,May 11-14, paper 5-2.
10. P.K. Ghosh, P.C. Gupta, O.M. Pal, R. Avtar, B.K. Jha, V. Sagar Dwivedi: *ISIJ Int.*, 1993,vol. 33, pp. 807-815.
11. N. Yurioka, H. Suzuki, S. Ohshita, and S. Saito, *Weld. J.*, 1983, vol. 62, pp. 147s-153s.
12. J.C. Ion, K.E. Easterling, and M.F. Ashby, *Acta Metall.*, 1984, vol. 32, pp. 1949-1962.
13. K.W. Andrews, D.J. Dyson, and S.R. Keown: *Interpretation of Electron Diffraction Patterns*, 2nd ed., Plenum Press, New York, NY, 1971, pp. 181-191.
14. M. Jung, S-J Lee, and Y-K Lee: *Metall. Mater. Trans. A.*, 2009, vol. 40A, pp. 551-559.

15. Y. Wang, S. Denis, B. Appolaire, and P. Archambault: *J. Phys. IV France*, 2004, vol. 120, pp. 103-110.
16. J.W. Christian: The theory of Transformations in Metals and Alloys, Part I, Equilibrium and General Kinetic Theory, 2nd ed., Pergamon Press, Oxford, 1975, pp.19-20.
17. E.J. Mittemeijer, A. Van Gent, and P.J. Van der Schaaf: *Metall. Trans. A.*, 1986, vol. 17A, pp. 1441-1445.
18. M.I. Luppo and J. Overjero-García: *Mater. Charact.*, 1998, vol. 40, pp. 189-196.
19. C.S. Roberts, B.L. Averbach, and M. Cohen: *Trans. ASM*, 1953, vol. 45, pp. 576-603.
20. E.C. Bain: *Alloying Elements in Steel*, 1st ed. American Society for Metals, Cleveland, OH,1939, pp. 146-260.

4 Predicting Transient Softening in the Sub-Critical HAZ of DP and Martensitic Steels

E. Biro[1,2], S. Vignier[1], C. Kaczynski[1], J.R. McDermid[3], E. Lucas[1],

J.D. Embury[2], Y. Zhou[4]

[1] ArcelorMittal Global Research, 1390 Burlington St., Box 2460, Hamilton, Ont., Canada, L8N 3J5

[2] Dept. of Materials Science and Engineering, McMaster University, 1280 Main St. W., Hamilton, Ont., Canada, L8S 4L8

[3] Dept. of Mechanical Engineering, McMaster University, 1280 Main St. W., Hamilton, Ont., Canada, L8S 4L8

[4] Dept. of Mechanical and Mechatronics Engineering, University of Waterloo, 200 University Ave. W., Waterloo, Ont., Canada, N2L 3G1

4.1 Abstract

To improve vehicle fuel economy and crash worthiness the automotive industry has been redesigning parts from advanced high strength steels such as dual-phase and martensitic steels. These steels have high strengths with the higher formability characteristics when compared to lower strength conventional steels of similar ductility. These steels derive their unique properties from their complex microstructures containing ferrite and martensite. During assembly welding, the martensite within the sub-critical region of the heat-affected zone tempers, which locally reduces mechanical properties. Although this phenomenon is well studied, it has yet to be quantified. The present work proposes a technique to measure the softening kinetics of dual-phase and martensite steels using rapid isothermal tempering. The resulting model was then validated by predicting the heat-affect zone softening that occurs in laser and resistance spot welds as well as by comparing the microstructures of the rapid tempered samples to the microstructures found in the sub-critical heat-affected zone of welded samples.

Keywords: HAZ softening, laser welding, resistance spot welding, JMAK Equation, Avrami Equation, dual-phase steel, martensite tempering

4.2 Introduction

With the environmental issues surrounding the build-up of greenhouse gases and their contribution to global warming, new standards are coming into force requiring the automotive industry to improve the fuel economy of their vehicle fleets [1]. One of the means being chosen by automotive manufacturers to fulfil these regulations is by decreasing vehicle weight. To achieve the necessary weight reductions without compromising passenger safety, conventional low C and high strength low alloy (HSLA) steels commonly used in vehicles ten years ago are being replaced with new higher strength, multiphase advanced high strength steels (AHSS). One of the families of AHSS being adopted for structural applications in significant quantities are the dual-phase (DP) steels [2].

DP steels have a composite microstructure comprising martensite islands within a ferrite matrix, where the strength of the steel generally increases with increasing volume fractions of martensite [3]. DP steels derive their strength from the interactions between boundary dislocations in the ferrite interacting with the martensite islands, which increases the kinematic hardening contribution to the overall flow stress and their high initial strain hardening rate [4]. This mechanism is one of the primary contributors to the relatively high ultimate tensile strengths (UTS) combined with reasonable uniform elongations characteristic of DP steels as compared to low C and HSLA steels [5].

However, because the unique mechanical properties of DP steels arise from a multi-phase microstructure containing significant volume fractions of martensite, their mechanical properties will degrade when the martensite is tempered [6], which occurs in the tempered area of a weldment heat affected zone (HAZ). This phenomenon, known as HAZ softening, was first reported when DP steels were flash butt welded for wheel rim applications [7,8]. In these situations, it was reported that failures were occurring in the softer tempered or sub-critical area of the HAZ.

Since this phenomenon was first observed, some work has been done to characterise it. Xia *et al.* showed that the softening measured within the HAZ of a DP steel weld was a sigmoidal function of the welding heat input and the maximum possible HAZ softening was a linear function of the steel martensite content [9]. Baltazar Hernandez *et al.* showed that in welds exhibiting HAZ softening, only the martensite phase softened and no significant decrease in hardness was observed in the ferrite phase [10], implying that the observed HAZ softening was solely a product of martensite decomposition. Although this work characterised the mechanisms of HAZ softening in weldments, the kinetics were not described.

Work has been done to quantify the martensite tempering rate in DP steels using the Johnson-Mehl-Avrami-Kolmogorov (JMAK) equation for both long [11] and short tempering times, the latter using welding data [12]. Both of these studies advanced the literature where the long tempering time study was able to precisely characterise the activation energy for all tempering stages and the welding study demonstrated that the tempering rate increased with martensite C content and was retarded by the presence of carbide-forming alloying elements. However, neither of these approaches were able to provide data that could be used to model HAZ softening. In particular, the long time tempering data did not reflect the welding cycle time scale, where tempering occurs over 0.1-5 s and the welding study did not decouple the effects of temperature and time, meaning that data from this study could not be used to model a generic welding cycle.

The present study seeks to characterise the kinetics of HAZ tempering during the welding cycle by carrying out a series of rapid iso-thermal tempering heat treatments on several DP and martensitic steels. This data will be used to characterise the alloy softening kinetics. This approach will be validated by predicting the HAZ softening observed in laser and resistance spot welds (RSW) made using a range of heat inputs, as well as. showing that the microstructures of isothermally tempered DP steels match those found in the non-isothermally tempered (welded) HAZ

4.3 Methodolgy

The study was carried out on seven steels. Four of these steels had a DP microstructure and three were fully martensitic. All of the steels were industrially produced using the following processing route: casting, hot rolling, cold rolling, annealing and quenching. During the annealing heat treatment, the DP steels were intercritically annealed while the martensitic and hot stamped boron steels were fully austenitized and water quenched. The steels used in this study represent a range of steel chemistries and martensite contents. It should be noted that all of the experimental DP steels had a ferrite-martensite microstructure as opposed to a ferrite-martensite-bainite microstructure. Alloy chemistry, Yurioka carbon equivalent (CE_N) [13], martensite volume fraction (f_{MART}) (determined by image analysis of scanning electron microscope (SEM) micrographs) and the as-received hardness for all experimental materials may be found in Table 4-1.

Table 4-1. Details of experimental materials (chemistry listed in wt%)

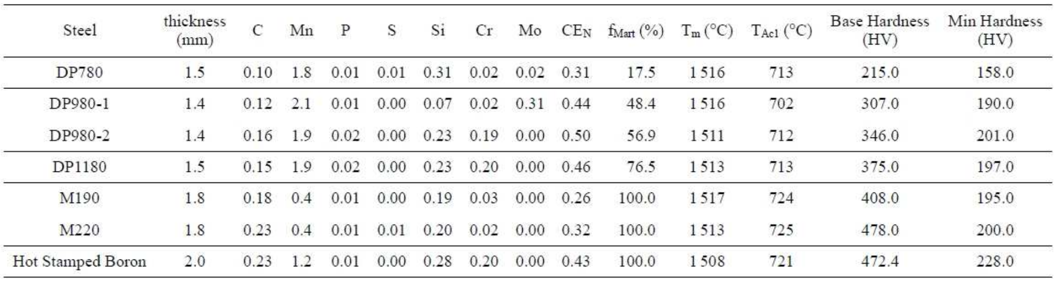

Steel	thickness (mm)	C	Mn	P	S	Si	Cr	Mo	CE_N	f_{Mart} (%)	T_m (°C)	T_{Ac1} (°C)	Base Hardness (HV)	Min Hardness (HV)
DP780	1.5	0.10	1.8	0.01	0.01	0.31	0.02	0.02	0.31	17.5	1 516	713	215.0	158.0
DP980-1	1.4	0.12	2.1	0.01	0.00	0.07	0.02	0.31	0.44	48.4	1 516	702	307.0	190.0
DP980-2	1.4	0.16	1.9	0.02	0.00	0.23	0.19	0.00	0.50	56.9	1 511	712	346.0	201.0
DP1180	1.5	0.15	1.9	0.02	0.00	0.23	0.20	0.00	0.46	76.5	1 513	713	375.0	197.0
M190	1.8	0.18	0.4	0.01	0.00	0.19	0.03	0.00	0.26	100.0	1 517	724	408.0	195.0
M220	1.8	0.23	0.4	0.01	0.01	0.20	0.02	0.00	0.32	100.0	1 513	725	478.0	200.0
Hot Stamped Boron	2.0	0.23	1.2	0.01	0.00	0.28	0.20	0.00	0.43	100.0	1 508	721	472.4	228.0

Material softening kinetics were characterised by rapid iso-thermal tempering using a Gleeble 3500 (Dynamic Systems Inc., Poestenkill, NY, USA). All samples were 100 mm x 12 mm with the rolling direction parallel to the long side. During the tempering cycle, samples were heated with average heating and cooling rates of 2190℃/s and 4140℃/s, respectively. Sample heating was more consistent than cooling, having standard deviations of 250℃/s and 3220℃/s, respectively. It should be pointed out that the minimum cooling rate measured was 820℃/s. It is believed that these rates were sufficient to assume an isothermal tempering kinetic. An example of a typical tempering cycle may be seen in Figure 4-1.

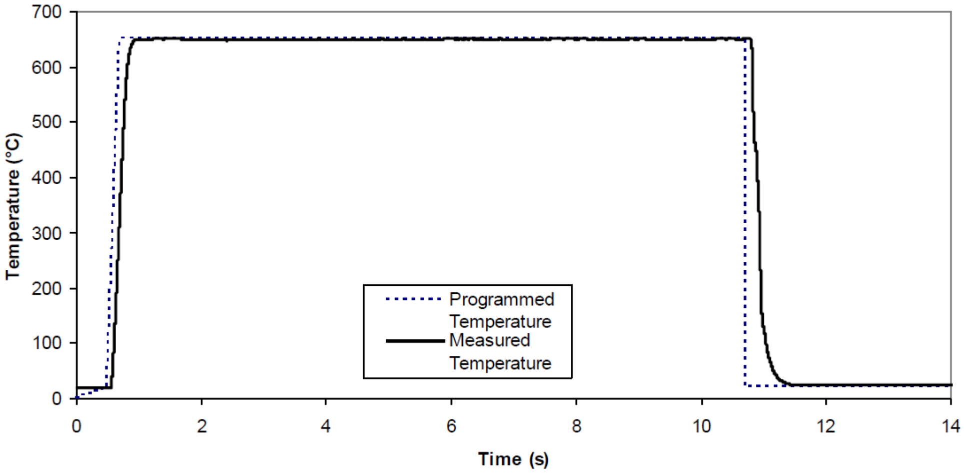

Figure 4-1. Typical Gleeble heat treatment cycle (taken from a 650℃ peak annealing temperature cycle).

Samples were tempered for times ranging from 0.2 s to 10 s to simulate typical times that the sub-critical HAZ would be at elevated temperature during welding. All experimental tempering temperatures and times are listed in Table 4-2. To determine the minimum tempered hardness of each material, all steels were subjected to a 1 hr (3600 s) furnace temper for all annealing temperatures listed in Table 4-2. After furnace tempering, samples were immediately water quenched to prevent further alterations to the microstructure.

Table 4-2. Tempering parameters for experimental steels.

Temperatures	Times
400°C, 500°C, 600°C, 650°C	0.2 s, 0.5 s, 1 s, 2 s, 5 s, 10 s, 3 600 s

Microhardness measurements were conducted to monitor the softening of the experimental steels arising from the tempering trials. All hardness measurements presented are the average of between 10-12 measurements taken through the sheet thickness. The large number of data points were intended to smooth the through-thickness hardness variation commonly observed in DP steels [14]. All hardness measurements were performed per ASTM E384-11 [15] using a 500 g load with a 15 s dwell time and were spaced more than 2.5 indentation spacings apart. Error bars on the hardness plots represent the 95% confidence interval (CI) of the average hardness value.

Welds were made using both laser and resistance spot welding. Laser welding was carried out using a 4 kW Nd:YAG laser. The spot diameter was approximately 400 μm and welding speeds were varied between 3-8 m/min. All laser welds were shielded with Ar gas flowing at 30 L/min. Spot welds were made using a 50 Hz AC pedestal welding machine per ISO 18278-2 [16].

Heat input to the work piece from the laser welding process was determined by the method of Xia *et al*. [9], who calculated it from measurements taken from the weld cross-section using a modified version of Rosenthal's equation for two dimensional heat transfer [17]. As spot welds are axisymmetric, heat input for these welds could not be evaluated using this equation. In this case, the heat input was calculated numerically with SORPAS (SWANTEC Software and Engineering ApS, Lyngby, Denmark) by matching the simulation results with the cross-sectional weld geometry. Minimum hardness values for all welds were taken from hardness maps measured across the weldments. Each map was separated into lines through the sheet thickness and the minimum hardness value on each profile represented the minimum hardness value at the specific depth the hardness profile was measured. All of the hardness values selected (10-18 depending on sheet thickness) were then averaged to determine the minimum hardness value of a particular weld.

Standard transmission electron microscopy (TEM) thin foils were used to examine the microstructure of all samples except for those taken from the low heat input laser weld, where the thin foils were prepared using focused ion beam (FIB). Standard thin foils were ground to between 60-80 µm using standard metallographic techniques, from which 3 mm diameter TEM sample discs were punched. The samples were thinned by electrolytic jet polishing using a 15℃ acetic acid solution with 5% perchloric acid at 70 V with 60 mA. FIB thin foils were cut from a cross-sectioned mount using Ga^+ ions. The thin foils were then attached to a Cu grid, thinned using Ga^+ ions and cleaned with Ar. All samples were viewed using a Philips CM12 TEM (Royal Philips Electronics, Amsterdam, The Netherlands) at an acceleration voltage of 120 keV. The TEM images presented below are representative of between 5 to 10 imaged areas, depending on the sample, with the exception of the low heat input laser weld where only two areas could be imaged due to the FIB preparation technique. All TEM samples examined were taken from the DP780 grade listed in Table 4-1.

4.3.1 Softening Kinetics Model

Per the methodology of Biro *et al.* [12], material softening during isothermal tempering was modelled using the Johnson-Mehl-Avrami-Kolmogorov (JMAK) equation [18-21]:

$$\phi = 1 - \exp\left(-kt^{n}\right) \tag{4-1}$$

where ϕ represents the fraction of the softening reaction completed, t is time, n is a fitting parameter representing the reaction rate and k is a fitting parameter characterizing the energy barrier to softening. As softening in DP steels is due to martensite tempering [10,12,22], where the tempering rate is temperature dependant, k was modelled using the Arrhenius equation:

$$k = k_0 \exp\left(\frac{-Q}{RT}\right) \tag{4-2}$$

where k_0 is a fitting parameter, Q is the activation energy for softening, R the universal gas constant and T the absolute temperature. As mentioned above, reaction progress was monitored by changes in material hardness. It is understood this may not be directly proportional to the progress of the tempering reaction, but it is of interest when considering how post-welding HAZ mechanical properties differ from those of the base material. The progress of the softening reaction (ϕ) was defined as follows:

$$\phi = \frac{H_{BM} - H}{H_{BM} - H_{\infty}} \tag{4-3}$$

where H_{BM} is the hardness of the base material, H the measured hardness of the sample at the point of interest, and H_{∞} the minimum hardness, defined in the present case as the hardness of the material after tempering 1 hour (3600 s) at 650℃.

4.3.2 Modelling of Weld Temperature History

During welding the temperature history in the sub-critical HAZ was assumed to be parabolic, per Ion *et al.* [23]. This assumption greatly simplified modelling the weld softening. Use of this assumption is believed to be appropriate because the parabolic temperature profile fits the actual welding temperature history very well near its peak temperature, where the majority of the tempering occurs (see Figure 4-2). The temperature history for each weld was defined as follows:

$$T = \left(T_{Ac1} - T_0\right)\left[-\left(\frac{t-\tau}{\tau}\right)^2\right] + T_{Ac1} \tag{4-4}$$

where T is temperature, T_{Ac1} the alloy Ac_1 temperature and T_0 the ambient temperature. τ is a time constant, representing the time for the sub-critical HAZ to heat from ambient temperature to its peak temperature, the Ac_1 temperature in this case (see Figure 2). For the laser welds in this study, τ was calculated using the equation of Xia *et al.* [9]:

$$\tau = \frac{\left(Q_{net} / vd \right)^2}{4\pi e \rho c_p \lambda \left(T_{Ac1} - T_0 \right)^2} \tag{4-5}$$

where Q_{net} is the heat input, v the welding speed, d the sheet thickness, ρ the density of steel (7860 kg/m^3), and c_p and λ the steel constant pressure heat capacity (680J/Kg/K) and thermal conductivity (30 W/m/K), respectively. The normalized heat input (Q_{net}/vd) was calculated by determining the heat input necessary to result in the observed distance between the fusion boundary and boundary of the sub-critical HAZ using the Rosenthal equation:

$$Q_{net} / vd = \frac{\rho c_p \left(r_{Ac_1} - r_m \right) \left(2\pi e \right)^{1/2}}{\left(\frac{1}{T_{Ac_1} - T_0} - \frac{1}{T_m - T_0} \right)} \tag{4-6}$$

where r_m and r_{Ac1} are the distances measured (taken from weld cross-sections) from the weld centreline to the fusion boundary and the isotherm corresponding to the Ac_1 temperature, respectively, and T_m is the melting temperature of the steel. It should be recalled that, because the spot welds are axisymmetric, τ for these welds was calculated using SORPAS.

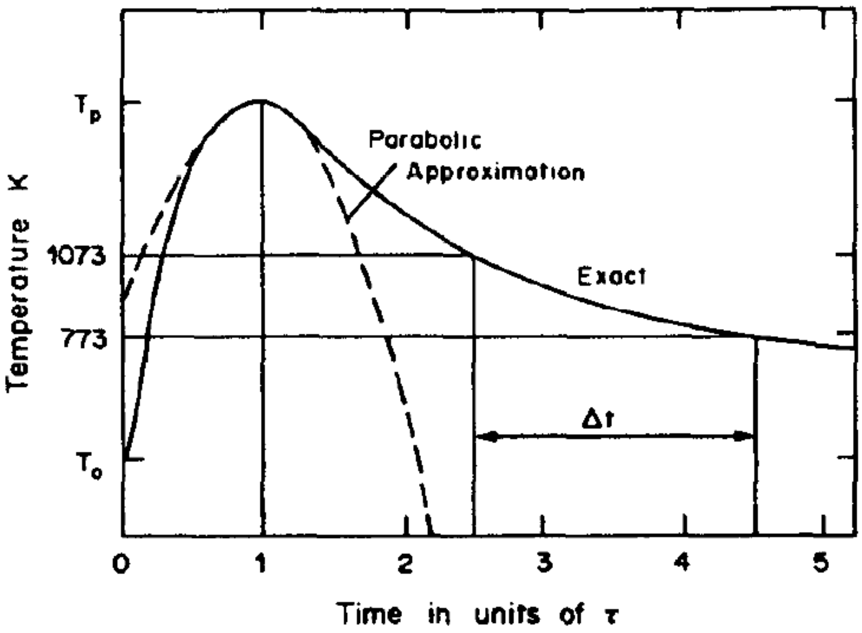

Figure 4-2. Comparison between the exact temperature history during welding and that of the parabolic temperature history for an arbitrary area within the HAZ (taken from [Ref. 23]).

4.4 Results and Discussion

4.4.1 Tempering Kinetics Quantification

When the hardnesses of the tempered samples were plotted against their respective tempering times, it was seen that hardness decreased sigmoidally with time in all cases. Furthermore, as would be expected, the hardness of the samples decreased as tempering temperature increased for similar tempering times. Examples of these general trends are shown for the dual phase DP780 and M220 martensitic steels in Figure 4-3 and 4-4, respectively. It should be noted that the increase in hardness above the base metal value seen at short tempering times for the DP780 samples tempered at 400℃ was not seen in any of the other samples. As this was unique to the DP780 tempered at 400℃ and did not change the sigmoidial nature of the hardness change with tempering time it was not investigated further. When the hardness values were converted to ϕ using Eq. 4-3 and plotted versus tempering time, the softening results took on the classic JMAK form (Figure 4-5 and 4-6). It should be noted that only the samples tempered at 650°C approached 1 because of how ϕ was defined relative to the reference hardness, H_∞.

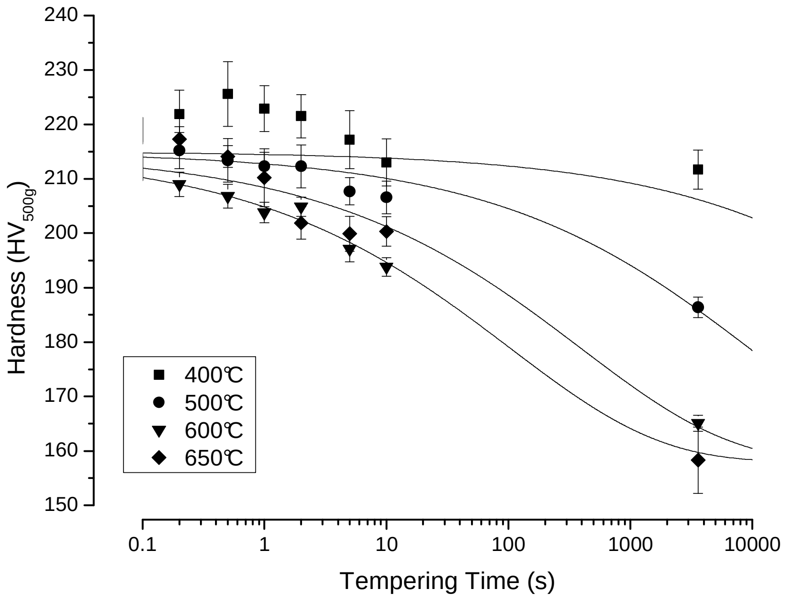

Figure 4-3. Hardness of tempered DP780 as a function of tempering time and temperature.

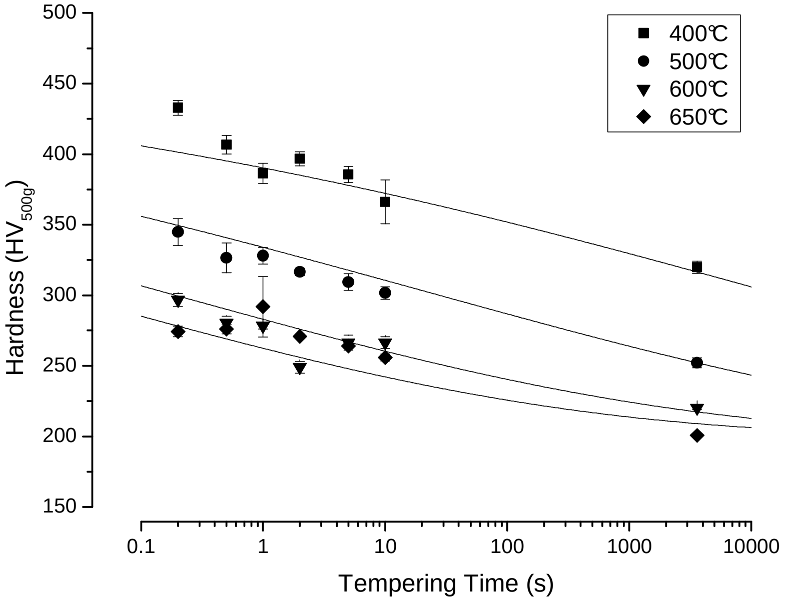

Figure 4-4. Hardness of tempered M220 as a function of tempering time and temperature.

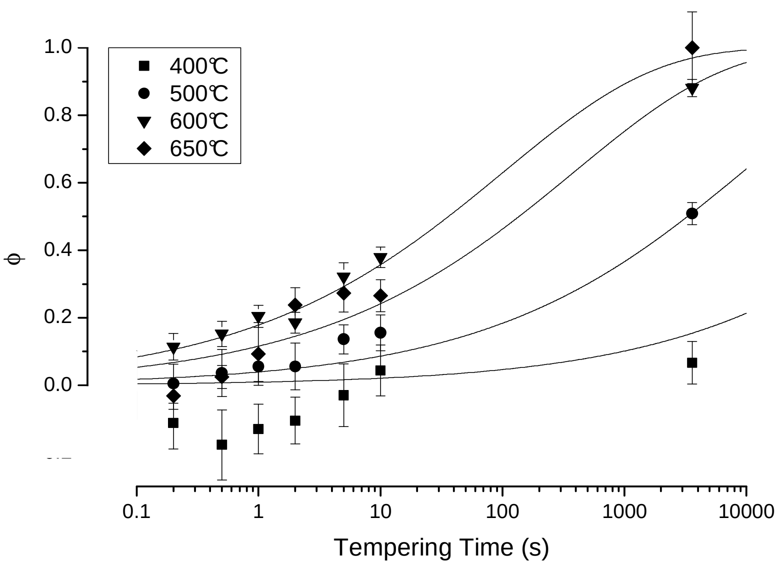

Figure 4-5. Calculated fraction of softening completed for DP780 as a function of tempering time and temperature.

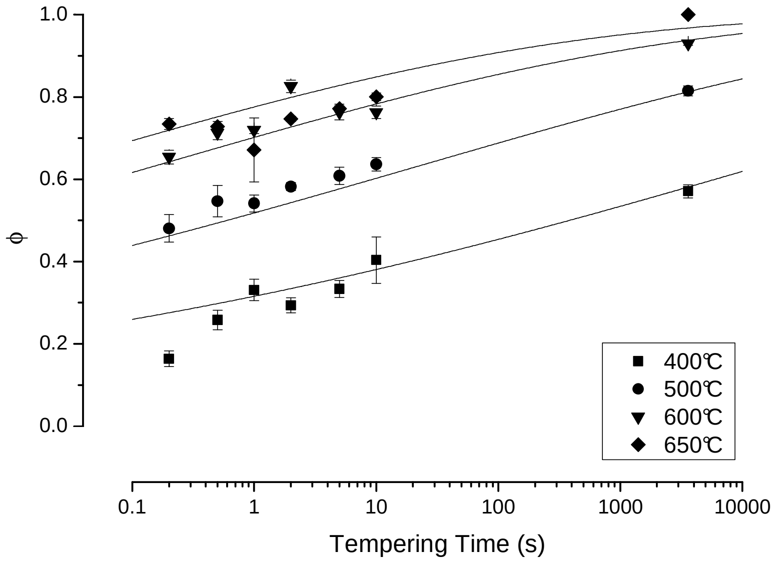

Figure 4-6. Calculated fraction of softening completed for M220 as a function of tempering time and temperature.

All of the softening data were fit to the JMAK equation by standard non-linear regression, the results of which are summarized in Table 4-3. It should be noted that the general goodness-of-fit for the data, as characterized using the adjusted R^2 parameter, exceeding 0.9 in all cases except for the DP780 samples, where the R^2 value was 0.79 (see Table 4-3). Although the fits were generally very good, the errors associated with the k_0 parameter values were high and in the case of the DP780 sample, the k_0 value was not significant (Table 4-3).

Table 4-3. JMAK fitting parameters and model goodness of fit measurement for experimental steels.

Steel	Q (kJ/mol)		k_0		n		Adj R^2
	Value	*95% CI*	Value	*95% CI*	Value	*95% CI*	
DP780	62.8	*13.72*	700.7	*1 245.0*	0.351	*0.048*	0.79
DP980-1	54.3	*3.90*	613.3	*320.3*	0.189	*0.012*	0.93
DP980-2	39.4	*2.10*	144.8	*42.3*	0.150	*0.010*	0.94
DP1180	39.2	*2.02*	167.7	*47.7*	0.139	*0.010*	0.94
M190	47.9	*2.61*	687.0	*254.2*	0.151	*0.013*	0.95
M220	28.3	*1.39*	59.9	*12.4*	0.101	*0.009*	0.94
Hot Stamped Boron	43.3	*1.84*	458.6	*122.2*	0.118	*0.010*	0.96

The values fit for Q and n (Table 4-3) were significantly different from the typical values associated with martensite tempering using the JMAK equation. In general, the literature reports much higher activation energies (177 to 270 kJ/mol [24-28]) for stage III tempering (i.e cementite formation) for the temperature ranges tested in the present case, although a value as low as 82 kJ/mol has been reported [29]. However, it should be noted that the above literature measured the activation energy using dilatometry, which is a more direct measurement of this transformation than the hardness measurements used in this work. When the current activation energies are compared to the results of work that measured tempering progression using hardness measurements, the current results are more comparable. For example, Takahashi and Bhadeshia [30] measured an activation energy of 33.5 kJ/mol and Hollomon and Jaffe [31] measured activation energies ranging from 50 to 209 kJ/mol, depending on the initial hardness of the martensite. It should be further noted that the values of n from the present work do not match the classic JMAK values of 3-4 for spherical particles [32]. However, it should be understood that the use of the JMAK equation in the present case does not represent the conditions under which it was derived, where a daughter phase was nucleated into a parent phase and grew until their transformation was complete. In the case of tempering, carbides are formed and grow until an equilibrium size is reached. The results presented here are agree with Takahashi and Bhadeshia [30], who also found that the value of n was below 3-4, determining n to be 0.62. However, this value is approximately 2-6 times greater than the values measured in this study. The value of k_0 was not compared to literature values because the units are dependent on the value of n.

Although the JMAK parameters presented in this work agree with the data presented from other studies where tempering kinetics were evaluated using hardness measurements [30,31], it is believed that the values derived for Q and n cannot give any specific insight into the underlying mechanisms responsible for the observed softening. For example, the observed softening can be attributed to a number of processes occurring simultaneously during both the rapid heat treatment and in the HAZ during welding thermal cycles, including martensite tempering (including carbide growth, the effect of alloy chemistry on carbide growth and formation of new ferrite), relaxation of residual stresses and the recovery and recrystallization of deformed grains with its attendant reduction of dislocation density. Thus, it is believed that the present values of the activation energy (Q) and time exponent (n) are actually an apparent activation energy and time exponent which are combinations of all of the above processes. Thus, the apparent disagreement between the values of Q and n with the classic tempering literature, which largely agree with the activation energy for C diffusion, can only be resolved through de-convolution of the terms comprising the derived apparent activation energies and time exponents. This exercise is beyond the scope of the present study and will be addressed in a subsequent contribution.

However, the evidence in Table 4-3 concerning the goodness of fit parameter (adjusted R^2) clearly indicates that the present form of the JMAK equation is a convenient mathematical representation of the combined mechanisms leading to the observed the HAZ softening. Furthermore, it can be seen that this mathematical form can be applied across a variety of chemistries and starting martensite contents across this class of alloys and can be used as an empirical predictor of the softening kinetics and material properties in the sub-critical HAZ.

4.4.2 Using the JMAK equation to describe non-isothermal tempering during welding

To compare the hardness change during isothermal Gleeble tempering to the non-isothermal tempering cycle found in welds, the tempering damage over the entire welding cycle must be summed. However, because of difficulties associated with integrating the nested exponentials found within Eq 4-1 this is very difficult. To overcome this issue, other researchers have changed Eq 4-1 such that the term within the exponential became $-(kt)^n$ [25,26], which greatly simplifies the integration. However, this approach was not followed here. Instead, it was decided to convert the thermal history experienced during welding to an equivalent isothermal temperature heat treatment with a tempering temperature equal to the alloy Ac_1 temperature (Table 4-1). This was done by equating Eq 4-1 evaluated at the alloy Ac_1 temperature to Eq 4-1 evaluated at the instantaneous HAZ temperature during the welding cycle and integrating this expression from t=0 to t=2τ(the time for the complete weld cycle). This resulted in the following expression:

$$t_{Ac1} = \int_{t=0}^{t=2\tau} \exp\left[\frac{Q}{Rn}\left(\frac{1}{T_{Ac1}} - \frac{1}{T}\right)\right] dt \qquad (4\text{-}7)$$

where t_{Ac1} is the equivalent isothermal tempering time at the Ac_1 for the subject welding cycle. Although this equation may applied to any general welding cycle, in this study, the parabolic assumption from Figure

4-2 was used. Once t_{Ac1} was calculated, equivalent T_{Ac1} isothermal HAZ softening may be predicted using Eq 4-1. It is understood that calculating HAZ softening using the isothermal equivalent from Eq 4-7 assumes that the final hardness for a tempered material will be temperature independent for long tempering times. From Figure 4-3 and 4-4 this is not certain. However, as Hollomon and Jaffe [31] showed that tempered hardness is a function of a tempering parameter combining the effects of temperature and time and not temperature alone, it is felt that the above assumption is justified considering that t_{Ac1} is effectively a tempering parameter representing the equivalent tempering time for the welding cycle if it was entirely carried out at the Ac_1 temperature.

4.4.3 Predicting the hardness of laser and spot welds at r_{Ac1}

With the conversion factor to compare the non-isothermal temperature cycles of welding to the isothermal cycle needed for the JMAK equation (Eq. 4-7), the hardness at r_{Ac1} or minimum HAZ hardness (H, Eq. 4-3) for a given set of welding conditions may be predicted by rearranging Eq 4-3 such that:

$$H = H_{BM} - \phi\left(H_{BM} - H_{\infty}\right) \qquad (4\text{-}8)$$

To validate whether the proposed JMAK equation could be used to predict the minimum HAZ hardness, a series of high and low heat input laser and resistance spot welds were made from the materials examined in this study. The welding time constants, describing the thermal history of each weld (from Eq 4-4. and 4-5), may be found in Table 4-4. Other material properties used in these calculations (e.g. base material hardness) can be found in Table 4-1. The minimum hardness values measured in these welds were then compared to the minimum HAZ hardness predicted using the isothermal T_{Ac1} annealing time (t_{Ac1}, Eq. 4-7). When the predicted and measured hardness values were compared, it was found that the average absolute error was 16.2±5.6 HV, which translates to an error of 6.2±2.1% when normalized against the base material hardness (see Figure 4-7). These hardness predictions were then subtracted from the base material hardness to predict maximum softening ($H_{BM} - H$), where these results showed stronger agreement with the measured values (Figure 4-8). It should also be noted that although the absolute error from the hardness predictions appear large, the predicted hardness values were within 10% of the measured hardness values and are felt to be as accurate as may be reasonably expected within the context of the process variations inherent in the welding process. Thus, these results imply that the data generated through isothermal annealing experiments can be successfully used to predict the HAZ softening characteristics of DP and martensitic steels through proper transformation of the non-isothermal temperature profiles characteristic of welding to the isothermal processes characteristic of those described using the JMAK equation.

Table 4-4. Minimum hardness and time constants of weld samples to validate JMAK softening model (Figs. 4-7 and 4-8).

Steel	Laser Welding				Resistance Spot Welding	
	High Heat Input		Low Heat Input			
	τ (s)	Hardness ($HV_{500\,g}$)	τ (s)	Hardness ($HV_{500\,g}$)	τ (s)	Hardness ($HV_{500\,g}$)
DP780	0.104	211	0.049	216	0.650	210
DP980-1	0.147	264	0.045	267	0.820	252
DP980-2	–	–	–	–	0.640	277
DP1180	–	–	–	–	0.640	275
M190	0.063	246	0.036	256	0.770	236
M220	0.058	235	0.032	262	0.770	238
Hot Stamped Boron	0.031	251	0.040	261	0.770	282

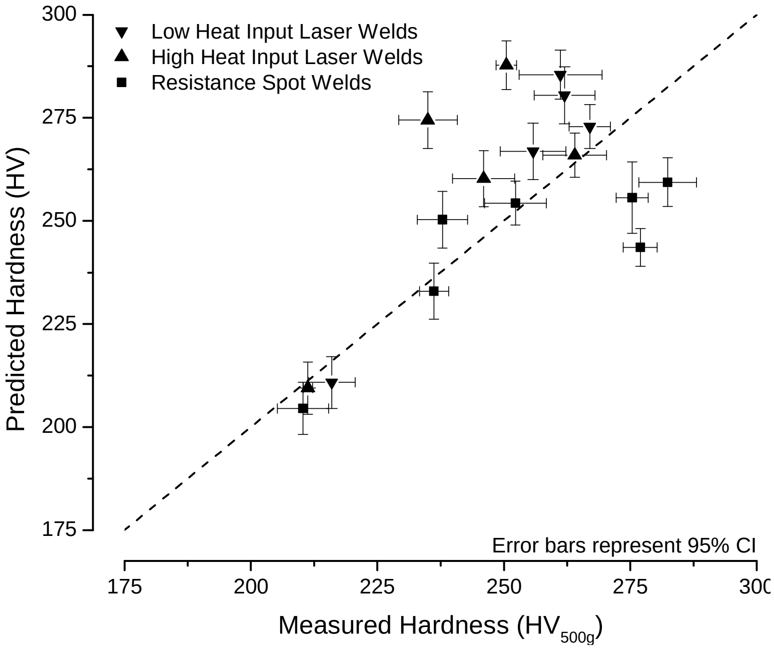

Figure 4-7. Comparison between the measured hardness and the hardness predicted by the JMAK equation using the parameters listed in Table 4-3.

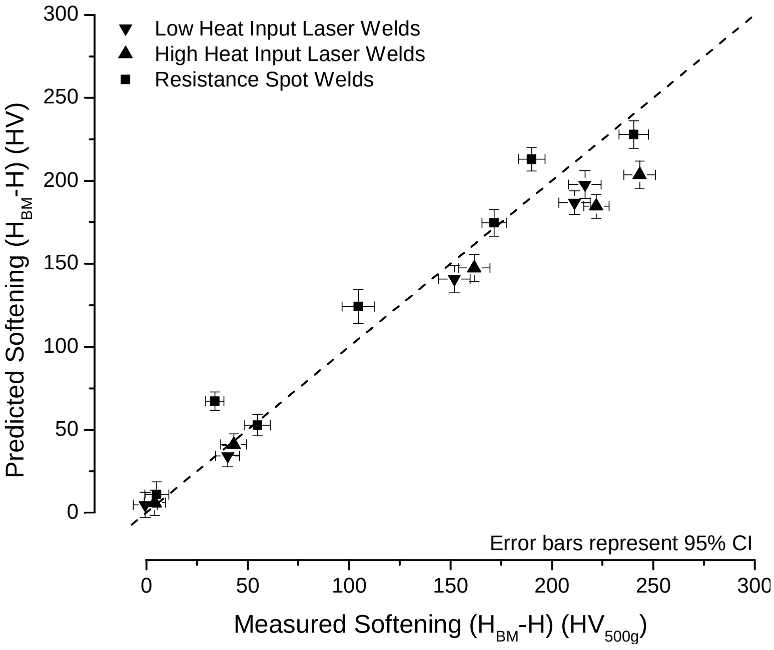

Figure 4-8. Comparison between the measured HAZ softening and the HAZ softening predicted by JMAK equation using the parameters listed in Table 4-3.

4.4.4 Microstructural comparison of sub-critical weld HAZ and Gleeble samples

Microstructural analysis was carried out to verify that the isothermal tempering treatments produced the same transformations in the experimental steels as the non-isothermal welding tempering cycle which occurs in the sub-critical HAZ. For this purpose, a TEM analysis comparing the sub-critical HAZ of laser welded DP780 using high heat input (τ = 6.8 s and t_{Ac1} = 3.0 s) and low heat input (τ = 0.045 s and t_{Ac1} = 0.020 s) to Gleeble samples tempered at 650°C for 10 and 0.5 s was carried out. The relative t_{Ac1} and ϕ values for these samples may be compared in Table 4-5. As part of this analysis, the as-received base material was examined, which revealed the expected mixture of ferrite and martensite as well as the high dislocation density typically associated with DP steel microstructures (Figure 4-9).

Table 4-5. Relative t_{Ac1} and ϕ values of samples used for TEM examination.

Sample	t_{Ac_1} (s)	ϕ
High Heat Input Weld	3.00	0.39
Long Isothermal Tempering Time	2.24	0.36
Low Heat Input Weld	0.02	0.08
Short Isothermal Tempering Time	0.11	0.10

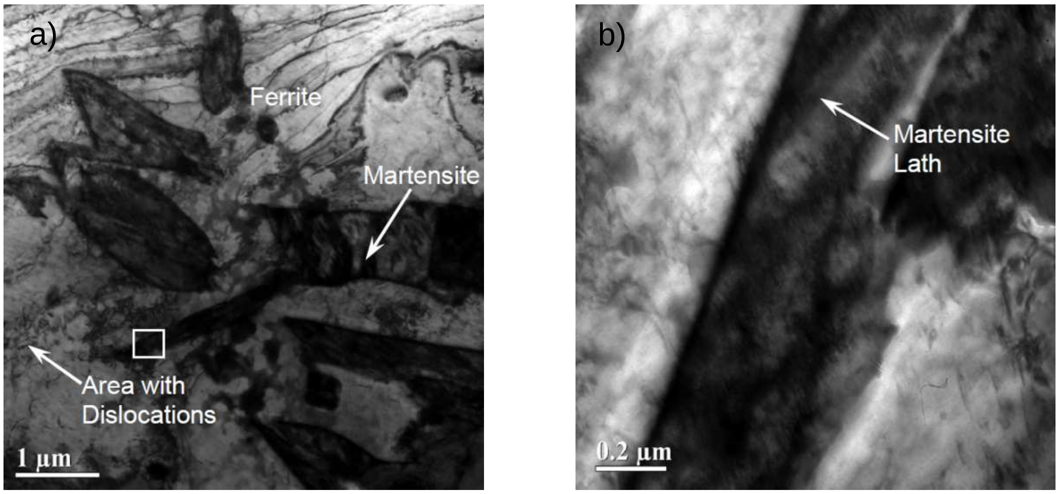

Figure 4-9. Structure of the as-received DP780 at (a) low and (b) high magnification.

Figure 10 shows the microstructure of the DP780 sample welded using high heat input (i.e. τ= 6.8 s). It can be clearly seen that the martensite had decomposed to ferrite and carbides approximately 50 nm in diameter. It can also be seen that the boundary of the original martensite grain was still visible (Figure 4-10). When the Gleeble heat treated samples were viewed (Figure 4-11), the martensite laths could no longer be discerned and some of the carbide particles had grown to approximately 100 nm in diameter (Figure 4-11). This difference is not surprising as the tempering time of the Gleeble tempered sample was almost twice that of the t_{Ac1} from the welded sample. However, the two samples are similar enough that it may be said that their respective decompositions followed a similar progression as the cementite particle sizes seen in both sample are of the same order of magnitude and the ferrite grains are lacking the dislocations seen in the base material structure.

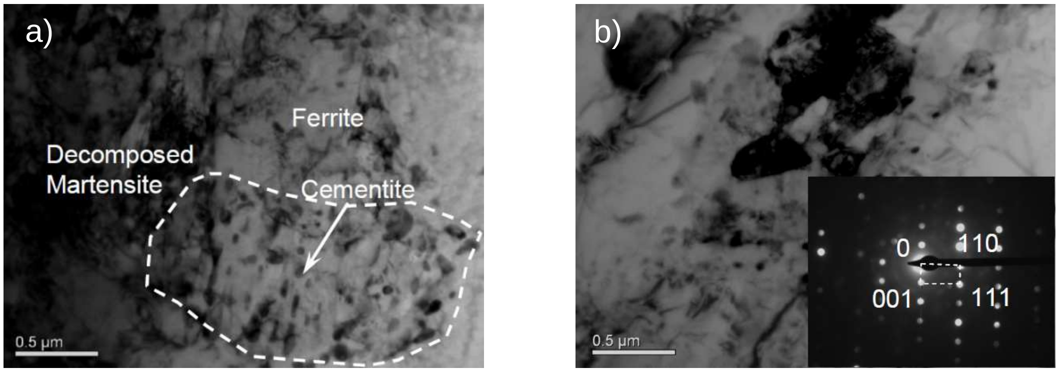

Figure 4-10. Tempered HAZ of DP780 welded with high heat input showing (a) the decomposed microstructure and (b) an area with large carbides along with the SAD pattern of the carbides found in the decomposed martensite.

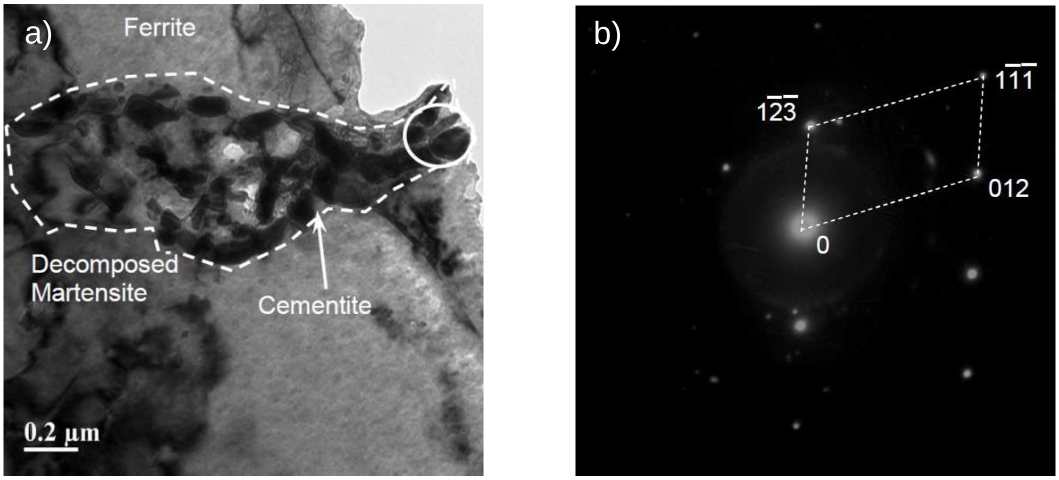

Figure 4-11. DP780 heat treated in the Gleeble at 650℃ for 10 s showing (a) the decomposed microstructure and (b) the SAD pattern of the carbides found in the decomposed martensite from the indicated area.

Although the higher heat input samples were similar, this was not the case for the low heat input samples. The welded sample (Figure 4-12) appears to be an early state of martensite decomposition. Although decomposed martensite was found, non-decomposed martensite grains were also seen. All of the cementite appears rod-like in shape whereas in the Gleeble tempered sample (Figure 4-13), all of the martensite decomposed with the cementite clearly forming on the lath boundaries. Also it should be noted that the cementite in the Gleeble samples had already spherodized contrary to what was seen in the welded sample (Figure 4-12). The difference between the samples should not be surprising considering that the tempering time of the Gleeble samples was over an order or magnitude larger than the welded samples, which was unavoidable as the Gleeble was not capable of tempering samples as quickly as could be done in the low heat input welds.

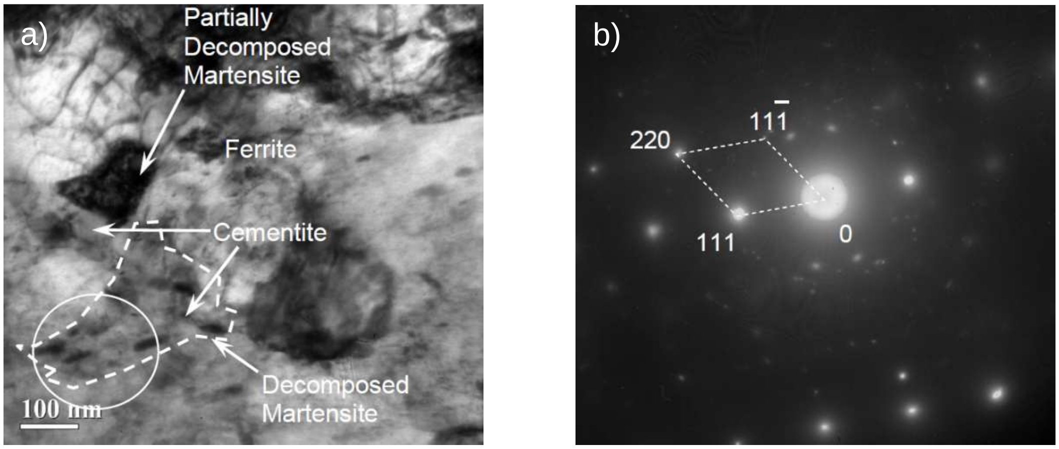

Figure 4-12. Tempered HAZ of DP780 welded with low heat input showing (a) the partially decomposed microstructure and (b) the SAD pattern of the carbides found in the decomposed martensite.

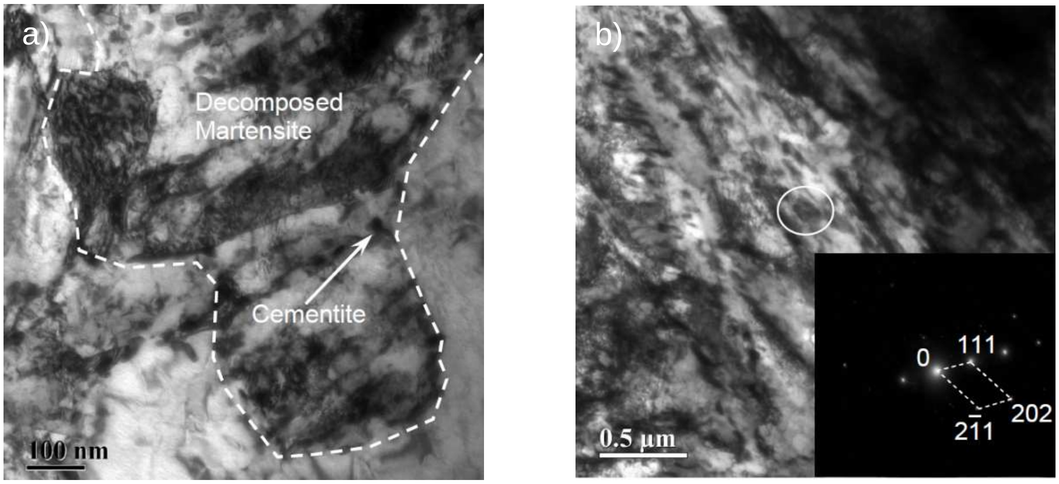

Figure 4-13. DP780 heat treated in the Gleeble at 650°C for 0.5 s showing (a) the decomposed microstructure (b) an area with large carbides along with the SAD pattern of the carbides found in the decomposed martensite.

Although the Gleeble and weld tempered samples were not comparable in all cases, it was still seen that the samples decomposed to the same products. Furthermore, if the samples are viewed in order of increasing heat input, it may be seen that they all follow the same tempering progression where the martensite decomposed to cementite and ferrite, the cementite spherodized on lath boundaries and finally the cementite coarsened and the underlying martensitic structure was eliminated. These observations coincide with those of Baltazar *et al*. [22] who saw similar changes in martensite and carbide morphology and location as well as the observed changes in ferrite dislocation structure. The microstructural analysis emphasised two conclusions. Primarily, although the Gleeble was not fast enough to reproduce the tempering response seen in welds made with very low heat input, it is believed that all of the samples underwent the same reaction path, regardless of whether tempering occurred during the isothermal Gleeble tempering or during the non-isothermal welding cycle. Furthermore, the microstructural changes reveal the complex metallurgical and mechanical changes responsible for the observed softening. This reinforces the earlier statement that the apparent activation energy and n parameters in the present JMAK form describing the process kinetics are a combination of a number of underlying processes. Thus, it should not be surprising that the values for Q and n derived in the present work differ from those expected.

4.5 Conclusions

Rapid isothermal tempering was performed on four dual-phase (DP) and three martensitic steels to characterise their tempering characteristics. The material's post-tempered hardness values were measured and modelled with the JMAK equation. The results of the iso-thermal tempering treatments were compared to hardness measurements and microstructural observations from welds to determine if this technique may be used to model the non-isothermal tempering that occurs in the sub-critical weld HAZ. From this study the following conclusions were drawn:

1. Gleeble isothermal rapid tempering can produce a tempering response that allows the effects of time and temperature on tempering to be separated.
2. The change in hardness from rapid iso-thermal tempering could be modelled using the JMAK equation with the effects of temperature accounted for by the Arrhenius equation.
3. The activation energy for softening did not match the literature values for stage III tempering measured from dilatometry experiments, but did match literature values from hardness experiments. It is suspected that JMAK parameters derived from the changes in the hardness after isothermal rapid tempering characterised several

complex metallurgical and mechanical changes within the samples, and could not be attributed to any single process.

4. The non-isothermal temperature history in welding can be converted to an equivalent isothermal temperature history using the activation energy derived from the isothermal tempering experiments.
5. The maximum HAZ softening in welds made under a variety of conditions could be accurately predicted using the JMAK equation.
6. The microstructural changes of the Gleeble and weld tempered samples followed the same progression and matched observations seen in the literature. However, the Gleeble was not capable of the very low heat input/high temperature tempering possible in welding. Even though this low heat input regime could not be reproduced, it is believed that the Gleeble can accurately reproduce the tempering reaction seen in the sub-critical HAZ.

4.6 Acknowledgements

The authors would like to acknowledge Olivier Bouaziz, Patrick Barges, and Colin Scott from ArcelorMittal Global R&D Maizières, Annick Willems from OCAS as well as Dr. Sashank Nayak from the Centre for Advanced Materials Joining at the University of Waterloo for their input and guidance. Furthermore we would like to thank ArcelorMittal for granting us permission to publish this work.

4.7 References

1. *Federal Register*: **74**(2009), 49454.
2. W. Gan, S.S. Babu, N. Kapustraka, and R.H. Wagoner: *Metall. Mater. Trans. A*, **37A** (2006), 3221.
3. R.G. Davies: *Metall. Trans. A.*, **9A** (1978), 671.
4. J. Gerbase, J.D. Embury, and R.M. Hobbs, *Structure and Properties of Dual-Phase Steels*, Ed. R.A. Kot and J.W. Morris, Metallurgical Society of the AIME, Warrendale (1979), 118.
5. D.K. Matlock, F. Zia-Ebrahimi, and G. Krauss, *Deformation, Processing, and Structure*, Ed. G. Krauss, American Society for Metals, Metals Park, OH, (1982), 47.
6. R.G. Davies, *Fundimentals of Dual-Phase Steels*, Ed. R.A. Kot and B.L. Bramfitt, Metallurgical Society of the AIME, Warrendale (1981), 265.
7. N. Yamauchi, T. Taka, K. Kunishige, and N. Nagao: *Trans. ISIJ*, **22** (1982), B-107.
8. T. Taka, Kunishige, N. Yamauchi, and N. Nagao: *ISIJ Int.*, **29** (1989), 503.
9. M. Xia, E. Biro, Z. Tian and Y.N. Zhou, *ISIJ Int*., **48**(2008), 809.
10. V.H. Baltazar Hernandez, S.K. Panda, Y. Okita, and N.Y. Zhou: *J. Mater Sci*, vol. **45** (2010), 1638.

11. T. Waterschoot, K. Verbeken, and B.C. De Cooman: *ISIJ Int.*, **46** (2006), 138.
12. E. Biro, J.R. McDermid, J.D. Embury, and Y. Zhou, *Metall. Mater. Trans. A*., **41A**, (2010), 2348.
13. N. Yurioka, H. Suzuki and S. Ohshita: *Weld. J.*, **62** (1983), 147s.
14. T. Burns, Weldability of a Dual-Phase Sheet Steel by the Gas Metal Arc Welding Process, Thesis, University of Waterloo, 2010.
15. E-384-11e1 Standard Test Method for Knoop and Vickers Hardness of Materials, ASTM International, West Conshohocken (2011).
16. ISO 18278-2 Resistance Welding – Weldability – Part 2: Alternative Procedures for the Assessment of Sheet Steels for Spot Welding, International Organization for Standardization, Geneva (2004).
17. D. Rosenthal: *Weld. J.*, **20** (1941), 220s.
18. W.A. Johnson and R.F. Mehl: Trans Am Inst Miner Metall Eng., **135** (1939), 416.
19. M. Avrami: *J. Chem. Phys.* **7** (1939), 1103.
20. M. Avrami: *J. Chem. Phys.* **8** (1940), 212.
21. M. Avrami: *J. Chem. Phys.* **9** (1941), 177.
22. V.H. Baltazar Hernandez, S.S. Nayak, and Y. Zhou, *Metall. Mater. Trans. A.* **42A** (2011), 3115.
23. J.C. Ion, K.E. Easterling, and M.F. Ashby: *Acta Metall.*, **32** (1984), 1949.

24. R.W. Balluffi, M. Cohen, and B.L. Averbach, *Trans. ASM*, **43** (1951), 497.
25. L. Cheng, C. M. Brakman, B.M. Korevaar, and E.J. Mittemeijer: *Metall. Trans. A*, **19A** (1988), 2415.
26. E.J Mittemeijer, L. Cheng, P.J. van der Schaaf, C.M. Brakman, And B.M. Korevaar: *Metall. Trans. A.*, **19A** (1988), 925.
27. T. Waterschoot K. Verbeken, and B.C. De Cooman: *ISIJ Int.*, **46** (2006), 138.
28. M. Jung, S-J. Lee, and Y-K Lee: *Metall. Mater. Trans. A.*, **40A** (2009), 551.
29. Tomita: *Mater. Sci. Technol.*, **4** (1988), 977.
30. M. Takahashi and H.K.D.H.: Bhadeshia, *Mater. Sci. Technol.*, **6** (1990), 592.
31. J.H. Hollomon and L.D. Jaffe: Trans Am Inst Miner Metall Eng, **162** (1945), 223.
32. J.W. Christian, Theory of Transformations in Metals and Alloys, Part I Equilibrium and General Kinetic Theory, Second Edition, Peregamon Press, Oxford, UK (1975).

5 Decoupling of the Softening Processes during Tempering of a Martensitic Steel

Elliot Biro[1,2], Joseph R. McDermid[3], Samuel Vignier[1],
Y. Norman Zhou[4]

[1] ArcelorMittal Global Research, 1390 Burlington St., Box 2460, Hamilton, Ont., L8N 3J5, Canada.

[2] Dept. of Materials Science and Engineering, McMaster University, 1280 Main St. W., Hamilton, Ont., L8S 4L8, Canada.

[3] Dept. of Mechanical Engineering, McMaster University, 1280 Main St. W., Hamilton, Ont., L8S 4L8, Canada.

[4] Dept. of Mechanical and Mechatronics Engineering, University of Waterloo, 200 University Ave. W., Waterloo, Ont., N2L 3G1, Canada.

5.1 Abstract

The increased adoption of martensite-containing advanced high strength steels, such as martensitic and dual-phase steels, into automotive applications has led to concerns among practitioners with respect to softening during rapid tempering cycles, characteristic of processes such as laser welding. Past studies on rapid tempering have successfully modelled the rapid tempering process; however, the activation energies and softening rates calculated did not match the classic literature values associated with martensite tempering. The present study examined rapid tempering data for a martensitic steel and separated the softening process into two stages: carbide nucleation and carbide coarsening. The activation energies calculated for each process matched classic values from the literature.

Keywords: Martensite, Tempering, Transformation kinetics, Precipitation hardening, HAZ softening

5.2 Introduction

Automotive companies are widely required by legislation to improve vehicle fuel economy [1]. One of the solutions being pursued is to reduce the weight of vehicle structures by reducing the steel gauge. However, in order to meet structural requirements while reducing material gauge, automakers are replacing lower strength conventional steels with higher strength advanced high strength steel (AHSS) grades such as martensitic, dual-phase (DP) and transformation induced plasticity (TRIP) steels [2].

AHSS derive their high strengths from complex microstructures comprising mixtures of various volume fractions of martensite, ferrite, bainite and retained austenite [3,4]. Although these alloys all exhibit excellent strength for their respective ductility, they all contain phases that decompose at higher temperatures. In automotive assembly, this is observed in the tempered area of weld heat affected zones (HAZ), where the martensite and retained austenite typically decompose during welding and the local mechanical properties drop [4,6]. This phenomenon, known as HAZ softening, was first observed in flash-butt wheel rim welding applications [7,8]. Since its initial characterization, a number of authors have investigated this phenomenon. Some initial studies concluded that HAZ softening was a strong function of the length of time the material temperature was elevated [9-11]. In these studies, HAZ softening was reduced by increasing the cooling rate after welding, thereby reducing the overall time the weldment was at an elevated temperature. Further work into this phenomenon has shown that HAZ softening is also related to material chemistry and initial microstructure. For example, the maximum HAZ softening possible in DP steels has been shown to be linearly dependant on martensite volume fraction [12] as the observed hardness decrease was due to martensite decomposition whereas no significant hardness changes were observed in the ferrite matrix [13]. Other authors have shown that softening kinetics are affected by alloy chemistry. For instance, increasing the martensite C content was found to increase the softening rate due to the increased driving force for C diffusion arising from the increased C potential between the tempered martensite and surrounding ferrite [6]. Conversely, alloying with carbide forming elements (e.g. Cr, Mo) has been shown to slow softening by either retarding cementite precipitation or growth, thereby minimizing the size of the cementite within the tempered martensite [6,14,15].

Limited work has been done on quantifying the effects of thermal history, microstructure and steel chemistry on martensite softening kinetics [16-18]. These studies used a characteristic equation, such as the Johnson-Mehl-Avarmi-Kolmogorov (JMAK) equation [19-22], to characterise the softening kinetics. In these cases, the softening kinetics were derived from a series of rapid isothermal tempering experiments designed to allow for the calculation of the tempering activation energy and rate exponent. Although these studies did show that transient softening could be quantified and predicted, the derived tempering activation energies and rate constants did not agree with those of the classic martensite tempering literature [16]. As it has been widely reported that martensite tempering is responsible for HAZ softening [6,7,9-11,13,15,16,23], it was expected that the activation energy for the softening process would be approximately 80-123 kJ/mol, the activation energy for C diffusion in ferrite [24,25], and the JMAK exponent would be approximately 0.67, the value associated with the precipitation of particles on dislocations [26]. Instead, the activation energy and rate exponent derived were approximately 28.3 kJ/mol and 0.10, respectively, for the M220 alloy [16], both of which are significantly lower than the classic literature values. Biro *et al.* [16] suggested that this disagreement was due to several processes being combined within the rapid tempering data, namely: martensite tempering, cementite precipitation and growth, ferrite recrystallization, and grain growth. Unfortunately, without a clear understanding of the underlying processes responsible for HAZ softening, it cannot be modelled or predicted phenomenologically. Thus, the current study will re-examine the data of Biro *et al.* [16] and expand the previous rapid tempering study of a fully martensitic steel in order to more fully determine and decouple the metallurgical processes responsible for softening during rapid tempering as applied to HAZ softening in advanced steels.

5.3 Experimental Methods

All experiments were carried out using an industrially fabricated 1.8 mm thick M220 grade martensitic steel. The as-received microstructure was produced using a continuous annealing line. The M220 chemical composition and as-received hardness can be found in Table 5-1.

Table 5-1. Chemistry (in wt%) and hardness of M220 experimental steel.

C	Mn	P	S	Si	Cr	Mo	Base Hardness (HV)	Min Hardness (HV)
0.23	0.4	0.01	0.01	0.20	0.02	0.00	478.0	200.0

All rapid tempering heat treatments were carried out using a Gleeble 3500 (Dynamic Systems Inc., Poestenkill, NY, USA). Samples comprised 100mm × 12mm coupons with the rolling direction parallel to the sample long axis. During tempering, average sample heating and cooling rates were approximately 2200°C/s and 4100° C/s, respectively. These heating and cooling rates allowed the rapid tempering cycles to be considered isothermal. Experimental tempering times and temperatures are listed in Table 5-2. However, it should be noted that tempering times of 20 s and 50 s were used only for tempering temperatures of 420°C or less.

Table 5-2. Temperatures and times used for experimental rapid tempering heat treatments.

Temperatures	Times
360°C, 380°C, 400°C, 420°C, 500°C, 600°C, 650°C	0.2s, 0.5s, 1s, 2s, 5s, 10s, 20s, 50s

All microhardness measurements were made using a Vickers indenter and a 500 gf load and 15 s dwell time. Indentations were separated by at least three indentation widths in accordance with ASTM E384-11 [27]. All microhardness data presented are the average of at least ten measurements. Error bars on the microhardness measurements represent the 95% confidence interval (CI) of the average microhardness value. In cases where data are presented without visible error bars, the 95% CI was smaller than the size of the plot symbol.

The microstructures of selected samples were examined using optical (OM) and scanning electron microscopy (SEM). In all cases samples were sectioned, mounted, and polished using standard metallographic methods. SEM samples were etched with 2% nital and gold coated before imaging with a JEOL JSM-6460LV SEM (JEOL Ltd., Tokyo, Japan) using an acceleration voltage of 20 keV. Optical microscopy samples were etched with Marshall's reagent. Grain size measurements utilized the linear intercept method [28].

All carbide equivalent diameters were measured from carbon replicas viewed in a transmission electron microscope (TEM). Replicas were made using standard methods, as described in 6, and were observed using a Philips CM12 TEM (Royal Philips Electronics, Amsterdam, The Netherlands) at an acceleration voltage 120 keV. Carbides were identified manually and their equivalent circular diameter determined using Clemex Vision – Professional Edition ver. 5.0.008e (Longueuil, Quebec, Canada) image analysis (IA) software. In this case, the equivalent circular diameter is defined as the diameter of a circle with the equivalent area of the measured carbide. The carbide size distribution from each tempering cycle was fit to a log-normal distribution to determine the average carbide diameter and sample standard deviation. A minimum of nine fields were viewed per sample, with the number of carbides per sample ranging between 1200-2500.

5.4 Johnson-Mehl-Avrami-Kolmogorov Softening Kinetics Model

From past work it has been shown that softening in DP and martensitic steels can be modelled using a sigmodal curve starting at the as-received alloy hardness and transitioning to a minimum hardness as heat input, temperature or tempering time increase [12]. By applying a simple transformation to the hardness data, the softening progression, ϕ, can be determined *via* [6,16]:

$$\phi = \frac{H_{BM} - H}{H_{BM} - H_{\infty}} \tag{5-1}$$

where H_{BM} is the as-received (base material) alloy hardness, H is the instantaneous measured hardness and H_{∞} is the minimum hardness, defined as the alloy hardness after a 1 hr furnace heat treatment at 650℃. From this definition, ϕ progresses from 0 in the as-received condition with no softening, to 1, the final hardness where tempering has been completed. In this form, the softening progression may be modelled using the Johnson-Mehl-Avrami-Kolmogorov (JMAK) equation [19-22]:

$$\phi = 1 - \exp\left(-kt^{n}\right) \tag{5-2}$$

where t is time, n the reaction rate exponent and k the energy barrier to softening as described by the Arrhenius equation:

$$k = k_0 \exp\left(-\frac{Q}{RT}\right) \tag{5-3}$$

where Q is the activation energy for softening, R the universal gas constant, T temperature, and k_0 a fitting parameter. Although the JMAK equation was developed to describe the growth of a daughter phase within a parent phase, it has been found to be suitable for the modeling of softening data with some minor modification [16]. In the case of the M220 steel used in this study, the JMAK equation (equation (5-2)) was used successfully by the present authors to model isothermal tempering hardness data [16]. However, the JMAK kinetics derived by Biro et al. [16] were not able to accurately predict the low temperature (i.e. $T \leq 400°C$) data added to the data set (see Figure 5-1).

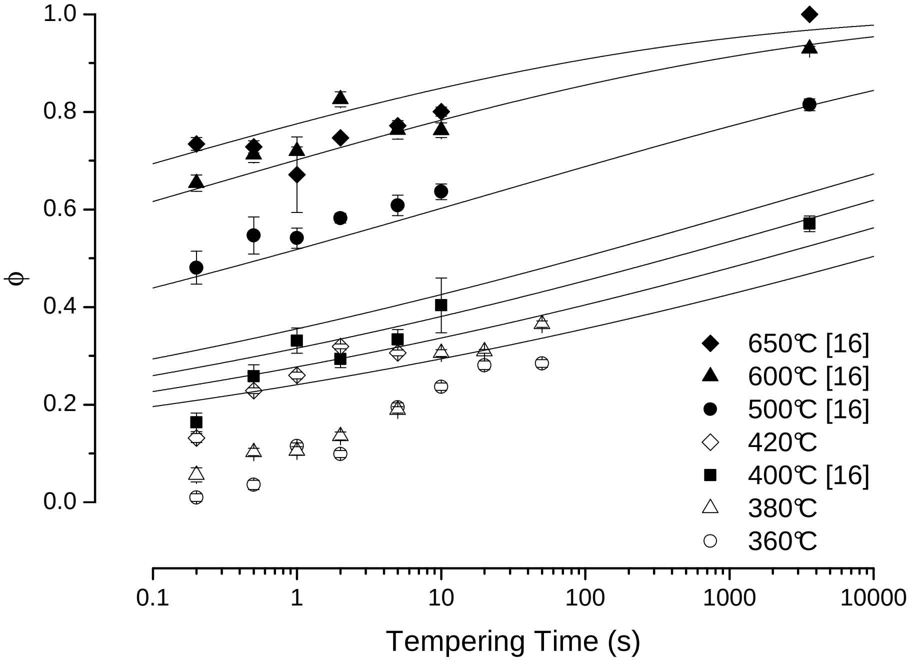

Figure 5-1. Softening progress (ϕ) versus tempering time for experimental M220 alloy.

5.5 Results

5.5.1 Tempering Data Analysis

Although the JMAK equation was used previously by the present authors to successfully model M220 softening data, two issues were identified with respect to its use in modelling HAZ softening. First, the values derived for Q and n (equations (5-2) and (5-3)) were 28.3 kJ/mol and 0.10, respectively [16]; values significantly lower than the established Q and n values of 80 – 123 kJ/mol [24] and 0.67 [26], respectively, associated with martensite tempering in the classic ferrous metallurgy literature. Second, the JMAK model was unable to adequately model the low temperature softening data. It was advanced that these discrepancies were due to multiple processes occurring during tempering [16].

In order to determine if multiple processes occurred during softening, which would affect the derived Q and n values [16] and accurate prediction of low temperature softening, the softening data were re-plotted as $\ln[-\ln(1-\phi)]$ versus $\ln(t)$ curves, as presented in Figure 5-2. By transforming equation (5-2) in this manner, n and k may be calculated directly from the slope and y-intercept of the $\ln[-\ln(1-\phi)]$ versus $\ln(t)$ plot. From this analysis, it can be seen that there are two distinct regions in the softening data, as characterised by the significant change in the slope of the curves of the 360°C – 420°C data, suggesting that two distinct processes were operating for shorter and longer tempering times. These are referred to as Stage I and Stage II softening in Figure 5-2 and in the subsequent discussion. A more detailed examination of Figure 5-2 will reveal that the slopes of the stage I portions of the curves are approximately parallel as are the slopes of the curves for stage II, indicating that similar processes are operating in both process regimes. In addition, the transition from Stage I to Stage II, as characterised by the time of the curve knee points, decreases significantly with increasing tempering temperature and could not be experimentally captured for temperatures higher than 420°C. This latter is consistent with softening being a thermally driven process.

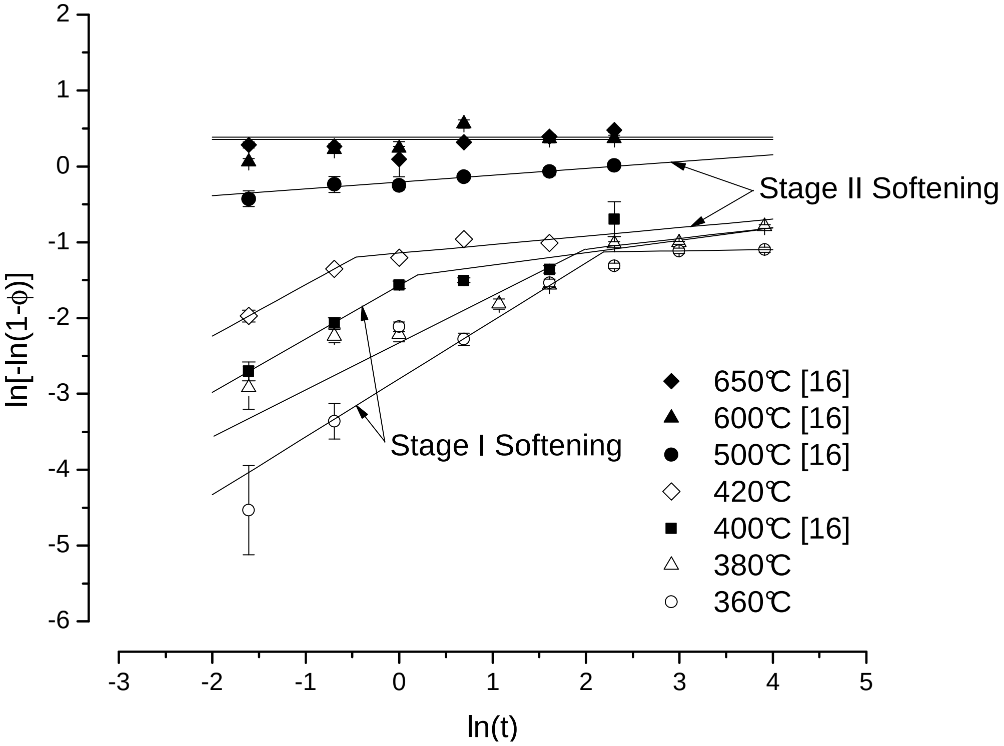

Figure 5-2. Transformed M220 softening data.

To determine the relationship between the two process regimes highlighted in Figure 5-2 and the microstructural evolution of the samples as a function of tempering time, the microstructures of the as-received material and samples tempered at 400℃ and 500℃ we re viewed *via* the SEM. The as-received base material comprised both non-tempered and tempered martensite grains, indicating that the as-received material had undergone some degree of autotempering during thermal processing (Figure 5-3a). When tempering at 400℃ for times of 1 s or less, the microstructures were quite similar to that the base material, as can be seen in Figures 5-3b and 5-3c. These observations, combined with the kinetic data from Figure 5-2, imply that martensite tempering had not been completed for these microstructures and that the tempering reaction was on-going. In the classic tempering process sequence, this would correspond to stage 3 of tempering [25]. At longer times and higher temperatures (Figures 5-3c - 5-3g) the microstructures comprised tempered martensite with a significant population of carbides. These observations and the change in slope observed for the softening data in Figure 5-2 suggest that nucleation was complete and that carbide coarsening underway. This corresponds to stage 4 of the classic tempering sequence [25]. The kinetics of each stage will be discussed separately in the below text.

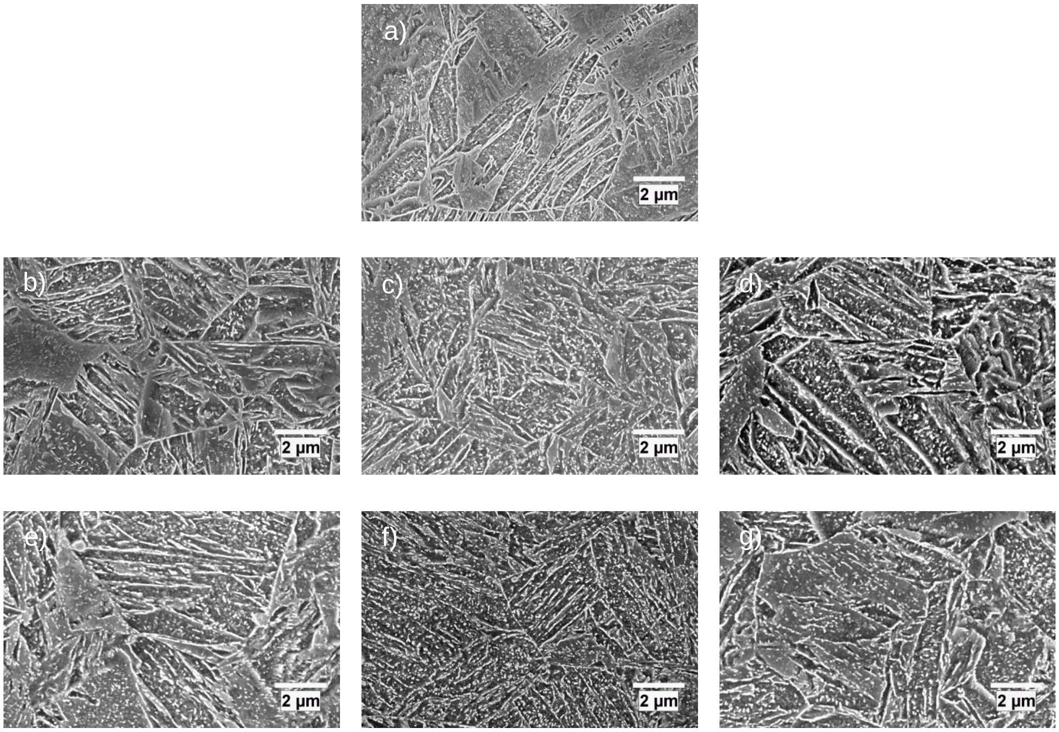

Figure 5-3. SEM microstructures of the a) as-received M220 and after tempering at 400˚C for b) 0.2 s, c) 1 s d) 2 s and at 500˚C for e) 0.2 s, f) 1 s and g) 2 s.

5.5.2 Stage I Softening – Carbide Nucleation

From the analysis of Figure 5-2, it was determined that the average JMAK exponent (n) value for the 360°C – 420°C stage I softening data was 0.659±0.003, which is in good agreement with the literature value for particle nucleation on dislocations of 0.67 [26]. To determine the activation energy for stage I softening, an Arrhenius plot (Figure 5-4) was constructed using the k values derived from the 360°C – 420°C short-time tempering data in Figure 5-2, from which an activation energy, Q, of 113±7 kJ/mol was calculated. This value is in good agreement with the activation energy of C diffusion in ferrite of 80 – 122 kJ/mol [24,25].

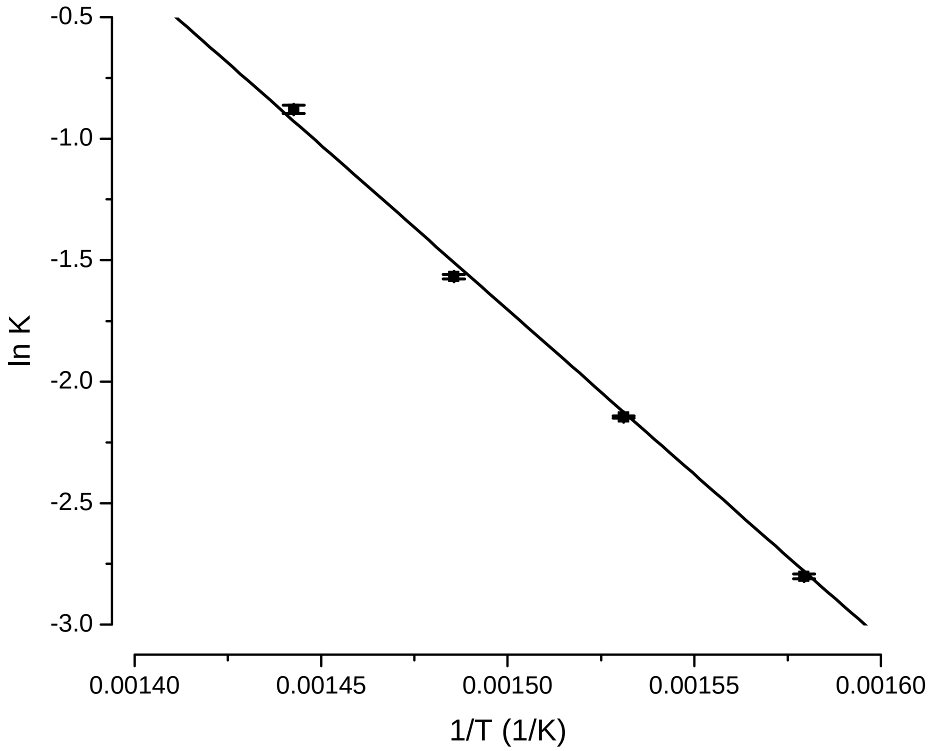

Figure 5-4. Arrhenius plot of *k* verus *1/T* for Stage I softening data (Figure 5-2) for samples tempered between 360-420˚C.

It is interesting to note that the degree of softening (i.e. ln[-ln(1-ϕ)]) value for the samples tempered at 360-420℃ was approximately -1.15, corresponding to a ϕ value of 0.27±0.05 at the curve knee point in Figure 5-2. Using a simple regression model, it may be calculated that for samples tempered at 500℃, Stage I softening would be completed at approximately 0.06 s (see Table 5-3). Timescales of this order are very difficult to capture experimentally and explain the lack of a visible Stage I softening stage from the experiments conducted with tempering temperatures greater than 420°C (see Figure 5-2).

Table 5-3. Time required to complete Stage I softening for tempering temperatures between 360℃-650℃.

Temperature (°C)	Tempering Time (s)
360	26
380	9
400	3.5
420	1.4
500	0.055
600	0.0023
650	0.0006

5.5.3 Ferrite Grain Size

After the carbide nucleation stage was completed, Figures 5-1 and 5-2 show that the steel continued to soften. This could be due to a combination of any three mechanisms: ferrite recrystallization, grain growth or softening associated with carbide growth. To investigate whether ferrite grain recrystallization or grain growth were responsible for further softening, samples tempered at 500℃ for 0. 2 s and 600℃ for 10 s were examined to determine if the grain structure changed during the tempering heat treatments. These microstructures are presented in Figure 5-5. Both samples exhibited a fine-grained, equiaxed microstructure where the average grain size for the samples tempered at 500℃ and 600℃ were 3.1±0.1 µm and 2.5±0.2 µm, respectively. The significantly smaller ferrite grain size of the sample tempered at 600℃ may be attributed to recrystallization, as reported by Speich [29]. However, it is believed that this slight reduction in grain size is not sufficient to have contributed significantly to the hardness changes observed in Figure 5-1.

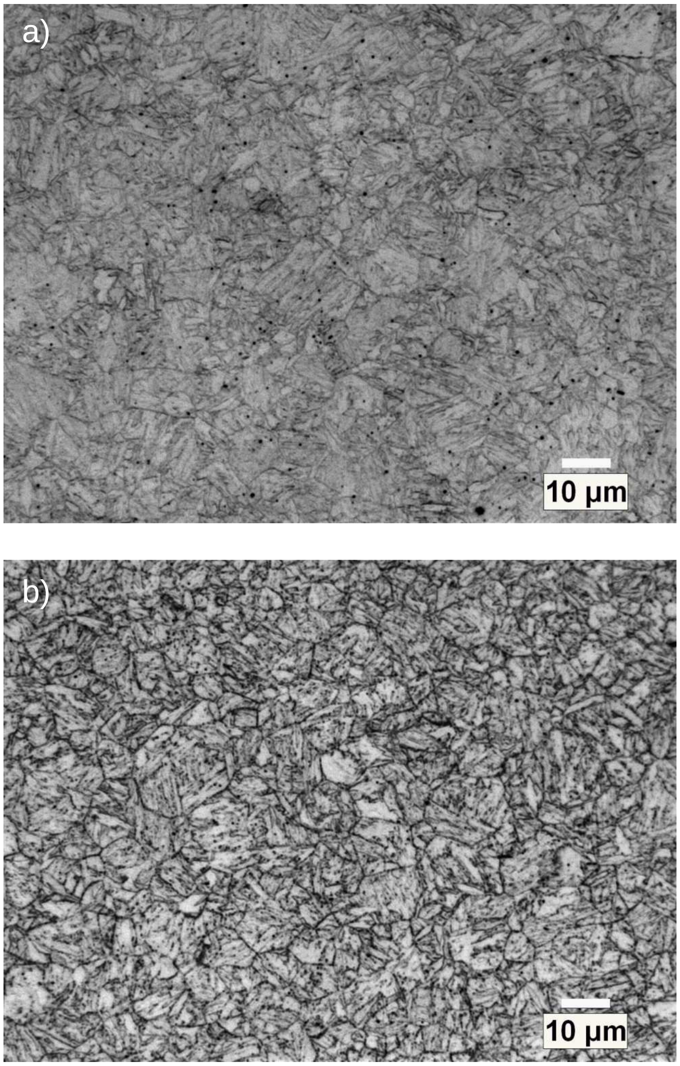

Figure 5-5. Optical microstructures of samples tempered at a) 500℃ for 0.2s and b) 600℃ for 10s.

5.5.4 Stage II Softening – Carbide Coarsening

From the above, it can be concluded that changes in the ferrite grain structure did not contribute significantly to Stage II softening (Figure 5-2). From Figure 5-3d-g and Figure 5-5, it may be seen that these microstructures exhibited large populations of carbides. These carbides can block dislocation movement through a precipitation hardening mechanism [30], the effectiveness of which a function of particle size and the inter-particle distance, as described by the Ashby-Orowan equation [31].

The carbides observed in the tempered M220 were identified as cementite for all TEM replicas examined [16]. Carbide size measurements were taken from tempered samples produced at 500°C and 600°C and their size and size distribution determined with the objective of deriving the role they played in the softening process. This data is presented in Figure 5-6 as plots of average cementite equivalent diameter versus tempering time and temperature. As would be expected, it can be seen that cementite in samples tempered at 600℃ grew more rapidly than those tempered at 500℃.

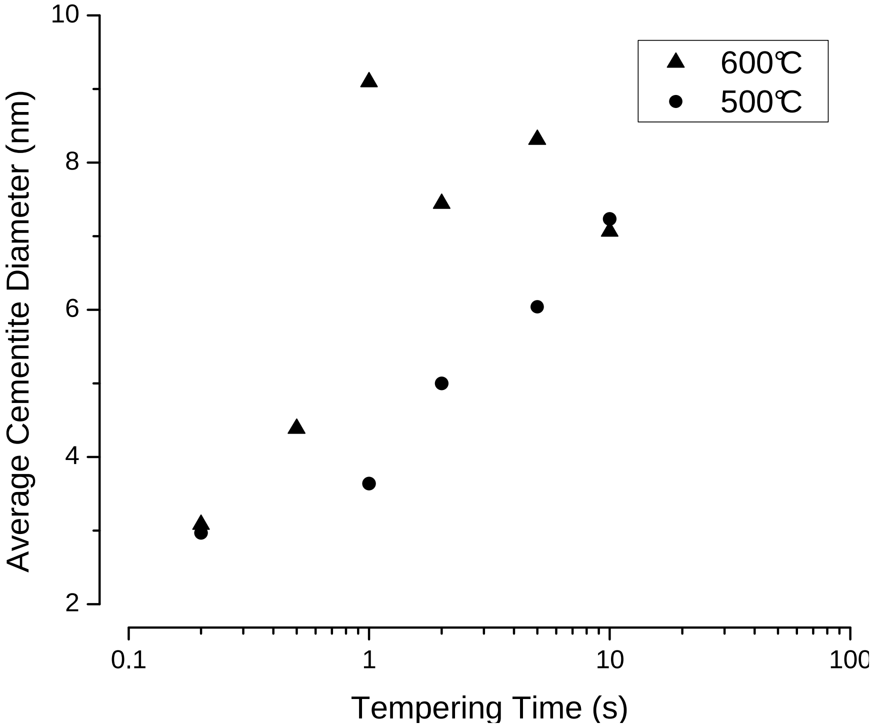

Figure 5-6. Average carbide equivalent diameter versus temping time for samples tempered at 500℃ and 600℃.

Cementite coarsening was consistent with the trends observed in the hardness data (Figure 5-1), where particle size increased with increasing time and temperature, thereby leading to a drop in precipitate density and decreased hardness. The contribution of carbide coarsening to the overall sample hardness can be calculated from this data using a modified version of the Ashby-Orowan equation arising from Guo and Sha [31]:

$$\Delta H = 0.84 \frac{1.2 G b M_T}{2 \pi q L} \ln \frac{d_p}{2b} \tag{5-4}$$

where ΔH is the change in hardness associated with precipitation hardening, G the ferrite shear modulus (81 GPa, [31]), b the Burgers vector (0.248 nm, [31]), M_T the Taylor factor (2.75, [31]), q the conversion factor between Vickers hardness and yield strength (2.9 MPa/HV [32]), d_p the carbide equivalent diameter and L the inter-particle spacing. The values of d_p and L were taken directly from the carbide size measurements and may be found in Table 5-4. The base hardness of the microstructure was assumed to be 92 HV from the hardness of ferrite plus contributions from solution strengthening alloying elements [33,34].

Table 5-4. Cementite equivalent diameter and densities with associated inter-particle distance and ΔH from samples tempered at 500℃.

Tempering Time (s)	Diameter (nm)	Particle Density (1/nm^2)	Inter-Particle Distance (nm)	Calculated ΔH (HV)
0.2	2.97	1.72E-03	24.1	258
1	3.64	1.84E-03	23.3	309
2	5.00	6.13E-04	40.4	200
5	6.04	3.69E-04	52.0	166
10	7.23	3.68E-04	52.1	182

The influence of cementite particle size on hardness was calculated using equation (5-4) for samples tempered at 500℃ as the carbide size data for samples tempered at 600℃ was too noisy for a confident evaluation of its effect (Figure 5-6). When the calculated hardness due to carbide coarsening was compared to the measured hardness values for samples tempered at 500°C, it can be seen that predictions followed the softening trend reasonably well (Figure 5-7). The average error from this prediction was 11%, which is reasonable considering the wide size distribution of the particles measured. The agreement between the precipitation hardening model and the measured hardness values suggests that carbide coarsening dominated Stage II softening.

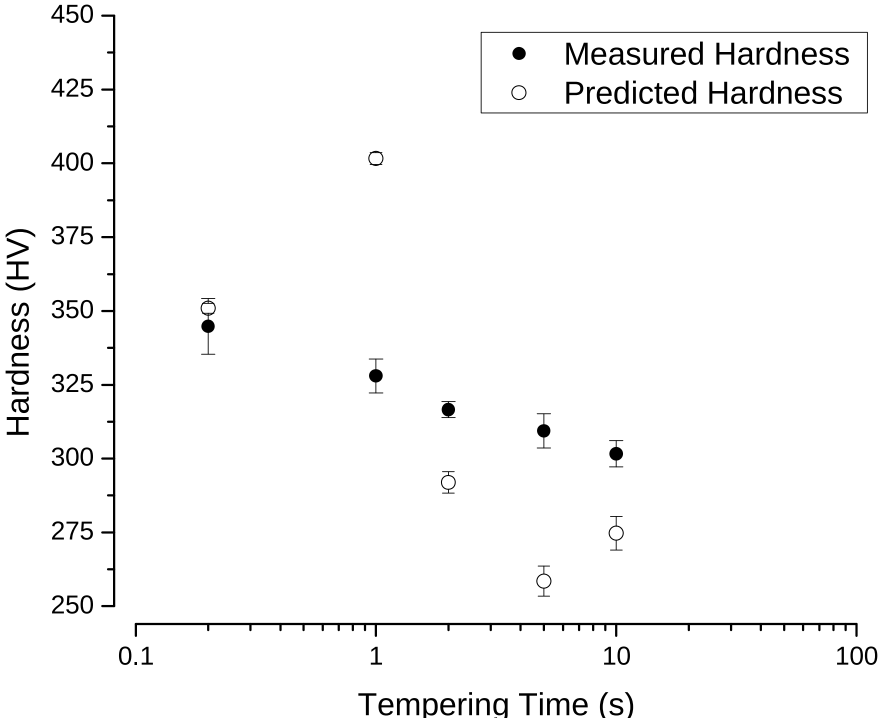

Figure 5-7. Comparison between the measured hardness from samples tempered at 500℃ and the hardness predicted by the modified Ashby-Orowan model [31].

Although Stage II softening largely arises from interactions between the ferritic matrix and carbide coarsening during tempering, the kinetic parameters *k* and *n* may still used to characterise the softening progression (Figure 5-2). Using the analysis employed for Stage I softening, the average *n* value for carbide coarsening was determined to be 0.108±0.001. Using the Stage II *k* data from Figure 5-2 and the

Arrhenius plot presented in Figure 5-8, it was determined that the activation energy for the carbide growth process was 35±4 kJ/mol. These values are in reasonable agreement with the values previously calculated for the entire softening process (28.3 kJ/mol and 0.10 [16]), which is not surprising as the majority of the data used to fit the JMAK parameters in [16] originated from the carbide coarsening stage of softening.

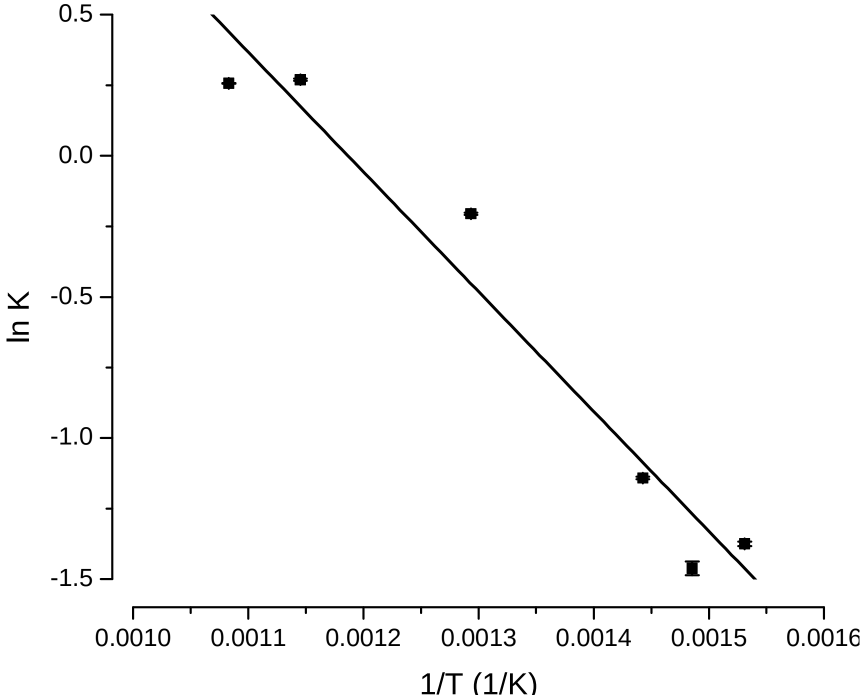

Figure 5-8. Arrhenius plot of *k* verus *1/T* for Stage II softening data (Figure 5-2).

5.6 Discussion

Decoupling the carbide nucleation and coarsening processes from the overall softening process revealed the reasons for the activation energy (*Q*) and JMAK exponent (*n*) of the combined softening processes in [16] not agreeing with the classic literature values for martensite tempering. As was shown in Figures 5-2 – 5-4, when the carbide nucleation process (Stage I in Figure 5-2) was separated from the overall softening process, the calculated activation energy (113 kJ/mol) and JMAK exponent (0.67) agreed well with the classic tempering literature values. From this, it can be concluded that Stage I softening of the present martensitic steel can be characterized as being equivalent to stage 3 (i.e. replacement of transition ε-carbides by cementite) of the well-established martensite tempering process [25].

A similar procedure applied to the Stage II portion of the tempering data in Figure 5-2 determined that the activation energy (Figure 5-8) and JMAK exponent for the carbide growth process was 35±4 kJ/mol and 0.108±0.001, respectively. However, it must be acknowledged that an inspection of these values would seem to be at odds with the rate controlling processes for carbide growth, in this case the diffusion of C. To resolve this seeming inconsistency, cementite growth kinetics need to be established.

Particle growth kinetics have been modelled by Lindsley and Marder [35] such that:

$$d_p = k_D t^m \tag{5-5}$$

where d_p is the particle equivalent diameter, k_D a diffusion dependant constant and m the coarsening exponent, which depends on the dominant coarsening mechanism (i.e. 0.2 for dislocation pipe diffusion, 0.25 for grain boundary diffusion and 0.33 for volumetric diffusion). By applying equation (5-5) to the particle growth data in Figure 5-6, it was observed that the dominant diffusion mechanism changed between samples tempered at 500°C and 600°C. When tempering at 500℃, *m* was found to be 0.25±0.02, indicating that grain boundary diffusion was the dominant cementite growth mechanism. However, at 600℃ *m* was determined to be 0.29±0.05, indicating that cementite growth was due to a combination of grain boundary and volumetric diffusion. This agrees with the results of Bannyh *et al.* [36], who also observed a progression from grain boundary to volumetric controlled diffusion with increasing tempering temperature.

Volumetric diffusion controlled particle coarsening kinetics have described by Lifshitz and Slyozov per [37]:

$$d_p^3 - d_{p0}^3 = \frac{64\gamma D_V C_0 V_m^2}{9RT}(t - t_0) \tag{5-6}$$

where d_p is the particle diameter at time t, d_{p0} the particle diameter at time t_0, γ the surface free energy of the precipitate per unit area of precipitate-matrix interface, C_0 the equilibrium concentration of solute atoms in the matrix, V_m the molar volume of the precipitate and D_v the volumetric diffusion coefficient. From Lindsley and Marder [35], grain boundary diffusion controlled particle growth can be described by:

$$d_p^4 - d_{p0}^4 = \frac{64\gamma D_{GB} C_0 V_m^2 \delta}{3k_1 RT}(t - t_0) \tag{5-7}$$

where D_{gb} is the grain boundary diffusion coefficient, δ the grain boundary thickness and k_1 a geometric constant.

It is well known that diffusion coefficients in equations (5-6) and (5-7) have an Arrhenius form and are an exponential function of activation energy and temperature. However, the cubic and quartic forms of equations (5-6) and (5-7), respectively, will result in a lower apparent activation energy for the carbide coarsening processes with respect to the particle diameter (d). By taking the 3rd and 4th roots of equations (5-6) and (5-7), respectively, it can be determined that the apparent activation energy for coarsening are 1/3 and 1/4 the values of the process activation energy, respectively. Applying this transformation to the experimentally derived activation energy for Stage I softening of 113 kJ/mol, the apparent activation energies for volumetric diffusion controlled carbide coarsening (equation (5-6)) and grain boundary diffusion controlled carbide coarsening (equations (5-7)) were be calculated to be 37 kJ/mol and 28 kJ/mol, respectively. These activation energies agree remarkably well with the activation energy calculated for the carbide coarsening process of 35±4 kJ/mol, suggesting that this process is also controlled by C diffusion in ferrite.

The correlation between the JMAK exponent, n (equation (5-2)), and the time exponent for particle coarsening, m (equation (5-5)) is less clear. To determine this relationship, it must first be understood how the softening progress (ϕ) varies with particle diameter (*d*), after which equations (5-2), (5-4), and (5-5) may be used to relate *n* to *m*. As equation (5-4) is quite complex, relating hardness both to $\ln d$ and the reciprocal of *L*, which increases as d_p decreases, it was decided that a more direct correlation between ϕ and *d* could be obtained by plotting these two parameters versus one another, as shown in Figure 5-9. From this, it can be seen that ϕ increases as a power function of particle diameter such that, in the present case:

$$\phi = 0.39 d_p^{0.26} \tag{5-8}$$

By substituting the appropriate form of *d* from equation (5-5) for the 500°C and 600°C particle data into equation (5-8), the ϕ time exponent would be 0.065 for the samples tempered at 500℃ and 0.075 for the 600℃ samples. However, in case of the JMAK equation (equation (5-2)), time is an exponential variable and is not easily isolated analytically. Thus, equations (5-2) and (5-8) were equated and *n* determined using non-linear regression. This technique yielded a JMAK equation *n* value 0.112±0.001. This agrees well with the value of the JMAK exponent calculated from the hardness data during carbide coarsening (i.e. 0.108±0.001) and shows how the non-linear relation between ϕ and d_p as well as the exponential form of the JMAK equation changes the rate constants from those expected from equation (5-5).

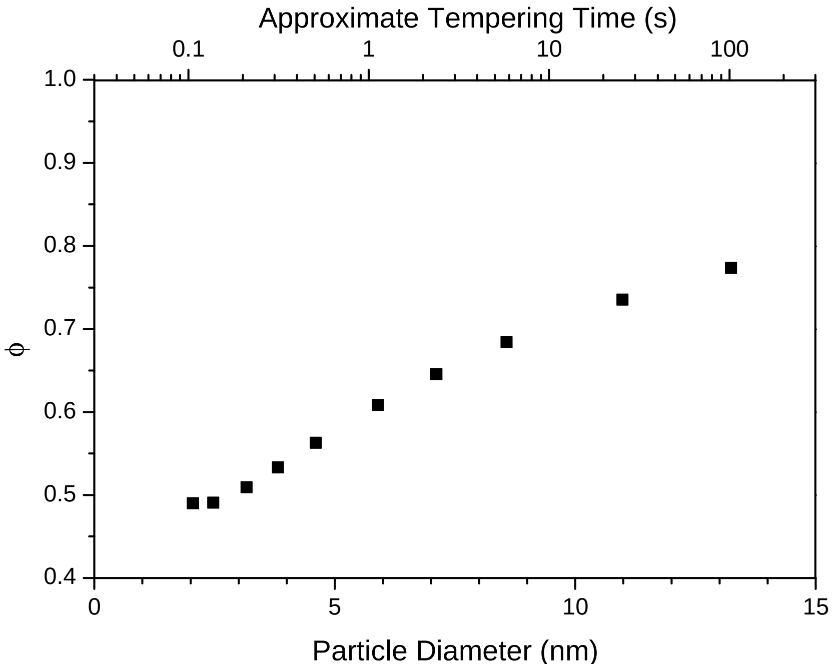

Figure 5-9. Softening progress (ϕ) versus cementite particle diameter for samples tempered at 500℃.

The overall conclusion of this study is that decoupling the short-time/lower temperature (i.e. Stage I, Figure 5-2) carbide nucleation process from the longer-time/higher temperature carbide coarsening process (i.e. Stage II, Figure 5-2) allowed for the derivation of JMAK parameters for rapid martensite softening consistent with the existing classic literature C-diffusion controlled models for martensite tempering. However, in most practical cases of rapid high temperature tempering, such as weld heat affected zone softening, the softening process can be efficiently modelled using kinetic parameters derived from the coupled process due to the dominant role carbide coarsening plays in this processes. However, it should be noted, that in cases where rapid tempering takes place at low temperatures (i.e. $T \leq 400$℃) for short times, carbide nucleation stage must be taken into account in the softening model because this will occur over a significant portion of the tempering cycle when tempering on the order of seconds or tens of seconds. This explains the poor fit between the predicted and actual ϕ values for the softening data in Figure 5-1 for tempering temperatures of 400°C or lower.

5.7 Conclusions

This study examined the softening observed in a martensitic M220 steel during rapid tempering to resolve the disagreement between the activation energy and time exponent calculated by Biro *et al.* [16] with the classic C-diffusion controlled literature associated with martensite tempering. It was found that:

1. The softening process could be broken into two sub-processes: carbide nucleation and carbide coarsening. These processes were separated within the overall softening data by transforming the softening versus time data.
2. The carbide nucleation stage occurred very quickly and was experimentally observed only for relatively short tempering times and tempering temperatures of less than 420℃. The activation energy and time exponent for carbide nucleation, calculated from hardness data, were determined to be 113±7 kJ/mol and 0.659±0.003, respectively,

matching the classic literature values for the activation energy for C diffusion in ferrite (80 – 120 kJ/mol) and particle growth on dislocations (0.67).

3. The apparent activation energy and time exponent calculated for the carbide coarsening stage of softening were 35±4 kJ/mol and 0.108±0.001, respectively.
4. The apparent activation energy associated with the carbide coarsening stage was determined to be an artefact of the non-linear relationship between the particle diameter growth kinetics and the diffusion mode of C for growth. When the activation energy for the linear cementite diameter growth was determined, it agreed well with the classic literature values for the diffusion controlled growth of C in ferrite.
5. The low time exponent associated with the carbide coarsening stage was due to the non-linear relation between the softening parameter (ϕ), cementite particle diameter and the exponential form of the JMAK equation.
6. Although this work revealed that there are two separate processes occurring when softening during rapid tempering, it is believed that in most cases softening during rapid tempering may be modelled using a kinetic model dominated by the carbide coarsening process. However, in the case of short-time tempering at temperatures of 400°C or less,

the carbide nucleation stage must be taken into account in order to predict softening.

5.8 Acknowledgements

The authors would like to thank Christine Kaczynski for preparing the rapidly tempered samples for this study, ArcelorMittal for the donation of experimental materials and for agreeing to publish this work and to the Natural Sciences and Engineering Research Council of Canada for financial support.

5.9 Nomenclature

b: Burger's vector length

C_0: initial concentration of solute atoms in the matrix

d_p: particle diameter

d_{p0}: particle diameter at initial time t_0

D_{gb}: grain boundary diffusion coefficient

D_V: volumetric diffusion coefficient

G: shear modulus

H_{BM}: as-received base material hardness

H: instantaneous material hardness

H_∞ minimum material hardness

ΔH: change in material hardness due to particle coarsening

k: energy barrier to material softening (JMAK equation)

k_D: diffusion dependant constant

k_0: fitting parameter for k

k_1: geometric constant for grain boundary particle growth

L: inter-particle spacing

m: coarsening rate exponent

M_T: Taylor factor

n: JMAK rate exponent

q: conversion factor from Vickers hardness to yield strength

Q: activation energy

R: universal gas constant

t: time

t_0: initial time for particle coarsening equation

T: temperature

V_M: particle molar volume

δ: grain boundary width

γ: particle surface energy per unit area of interface with matrix

ϕ: softening parameter

5.10 References

1. Federal Register 2009;74: 49454.

2. Gan W, Babu SS, Kapustraka N, Wagoner RH. Metall Mater Trans A 2006;37A:3221.

3. Davies RG. Metall Trans A 1978;9A:671.

4. De Cooman BC. Curr Opin Solid St Mater Sci 2004;8:285.

5. Kunishige K, Nobuyuki Y, Taka T, Nagao T. SAE Technical Paper Series 1983:830632.

6. Biro E, McDermid JR, Embury JD, Zhou Y. Metall Mater Trans A 2010;41A:2348.

7. Hashimoto S, Kanbe S, Masatoshi S. T Iron Steel I Jpn 1981;21:B-497.

8. Yamauchi N, Taka T, Kunishige K, Nagao, N. T Iron Steel I Jpn 1982;22:B-107.

9. Ghosh PK. ISIJ Int 1990;30:317.

10. Ghosh PK, Gupta PC, Ramavtar, JHA BK. Weld J 1991;70:7-s.

11. Ghosh PK, Gupta PC, Pal OM, Avtar R, Jha BK, Sagar Dwivedi V. ISIJ Int 1993;7:807.

12. Xia M, Biro E, Tian Z, Zhou YN. ISIJ Int 2008;48:809.

13. Baltazar Hernandez VH, Panda SK, Kuntz ML, Zhou Y. Mater Lett 2010; 64:207.

14. Biro E, Lee A. Welded Properties of Various DP600 Chemistries, Sheet Metal Welding Conference XI, Sterling Heights, MI, May 11-14, 2004:paper 5-2.

15. Nayak SS, Hernandez Baltazar VH, Zhou Y: Metall Mater Trans A 2011;42A:3242.

16. Biro E, Vignier S, Kaczynski C, McDermid JR, Lucas E, Embury, JD, Zhou YN. ISIJ Int 2013;53:110.
17. Vignier S, Biro E, Hervé M. 65th IIW Annual Assembly. Denver, CO, July 8-13, 2012: SC-Auto-58-12.
18. Shi J, Liu CR. Trans ASME 2005;127:476.
19. Johnson WA, Mehl RF. Trans Am Inst Miner Metall Eng, 1939;135:416.
20. Avrami M. J Chem Phys 1939;7:1103.
21. Avrami M. J Chem Phys 1940;8:212.
22. Avrami M. J Chem Phys 1941;9:177.
23. Baltazar Hernandez VH, Nayak SS, Zhou Y. Metall Mater Trans A 2011;42A:3115.
24. Shackelford JF, Alexander W. CRC Materials Science and Engineering Handbook, 3rd Ed. Boca Raton: CRC Press, 2001.
25. Honeycombe RWK, Bhadeshia HKDH. Steels: Microstructure and Properties, 2nd Ed. Oxford: Butterworth-Heinemann, 1995.
26. Christian JW. Theory of Transformations in Metals and Alloys, Part 1nd Ed. Oxford: Pergamon Press; 1975.
27. E-384-11e1 Standard Test Method for Knoop and Vickers Hardness of Materials. West Conshohocken, PA: ASTM International; 2011.
28. E112-12 Standard Test Methods for Determining Average Grain Size. Wes Conshohocken, PA: ASTM International; 2012.

29. Speich GR. Trans Met Soc AIME 1969;245:2553.
30. Tyson, WR. Acta Metall 1963;11:61.
31. Guo Z, Sha W. Mater Sci Technol 2002;18:529.
32. Cahoon JR, Broughton WH, Kutzak AR. Metall Trans 1971;2:1979.
33. Bain EC. Functions of the Alloying Elements in Steel. Cleveland: American Society of Metals; 1939.
34. Leslie WC. Metall Trans 1972;3:5.
35. Lindsley BA, Marder AR. Acta Mater 1998;46:341.
36. Bannyh O, Modin, H, Modin S. Jernkont Ann 1962;10:774.
37. Lifshitz IM, Slyozov VV. J Phys Chem Solids 1961;19:35.

6 Discussion

Chapters 3-5 sought to understand the kinetics of HAZ softening in DP and martensitic steels. These studies focused on the processes that led to softening during welding and rapid tempering, the kinetics of the softening process, quantifying softening kinetics and prediction of HAZ softening. When viewed as a whole, Chapters 3-5 sought to understand and model the change in hardness and the process kinetics associated HAZ softening during rapid tempering experienced in the welding HAZ.

6.1 Processes Responsible for softening

As presented in Chapter 5, HAZ softening occurs in two stages: carbide nucleation, where martensite decomposes to ferrite and cementite, and carbide coarsening, where the cementite that formed during nucleation grows, reducing the ability of the cementite particles to block dislocation movement in the ferrite matrix. However it should be also noted cementite growth will also occur during the carbide nucleation stage where C from the decomposing martensite will grow existing cementite as well as nucleating new particles.

The two softening stages may be clearly seen by the change in slope of the $\ln[-\ln(1-\phi)]$ vs $\ln(t)$ plot that was created by the logarithmic transformation of the softening progression plot (see Figure 6-1). The nucleation stage or Stage I of the softening process corresponds to the region on the graph occurring at short tempering times at temperatures below 420ºC with a steeper slope. The steep slope of this stage indicates that the transformation rate was more rapid than Stage II softening. Stage II softening, with the shallower slope, describes the change in hardness resulting from the reduction in the ability of the carbides to precipitation harden the matrix as they coarsen.

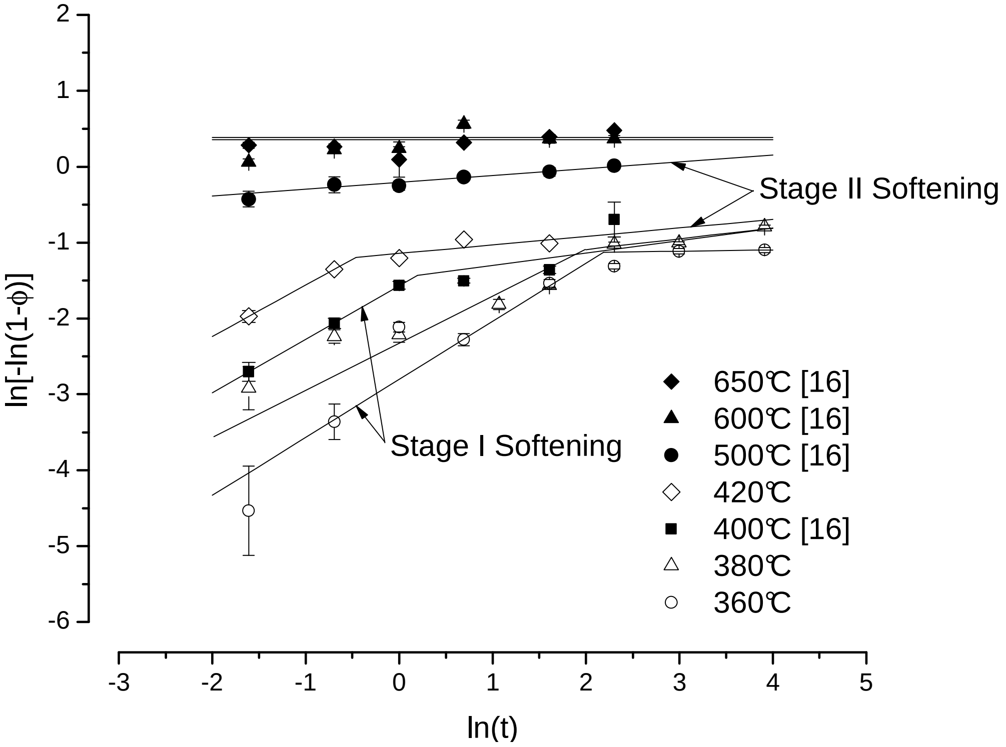

Figure 6-1. Transformed softening data for M220 steel (copied from Figure 5-2).

In the M220 steel, the nucleation stage (Stage I) was responsible for approximately 27% of the total reduction in hardness with the remainder being associated with the coarsening stage (Stage II). This is more subtle than what has been reported in the literature, where the entire softening reaction has been generalized as tempering without distinguishing any specific tempering stages [39,40]. However, as most rapid tempering heat treatments in the literature occurred at high temperatures [73,74], carbide coarsening dominated the softening process and, therefore, the process could be modelled without accounting for the carbide nucleation stage. When tempering at or below 400℃ at tempering times of less than 20 s, however, the carbide nucleation stage comprised a significant part of the softening process (see Figure 6-2). From this analysis, it can be concluded that when tempering at these low temperatures and short times, the carbide nucleation stage cannot be ignored when predicting softening. If the carbide nucleation stage (Stage I) was not accounted for in these cases, softening will be over-predicted.

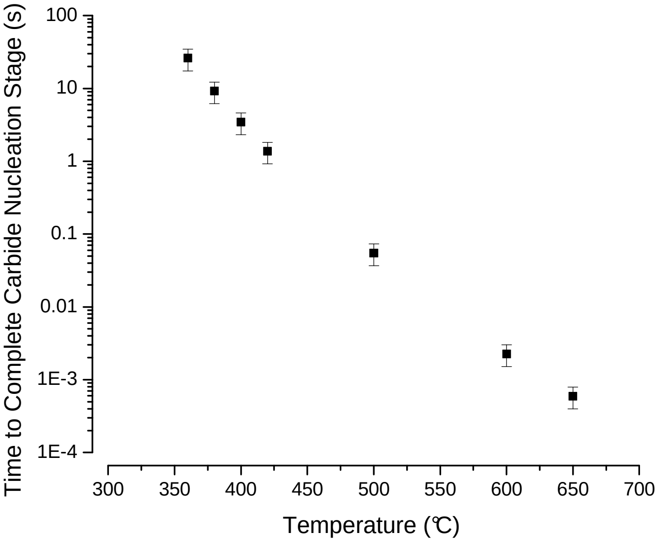

Figure 6-2. Time to complete carbide nucleation stage during rapid tempering of M220 (data taken from Table 5-3).

The separation of the processes responsible for softening also clarifies the role that alloying elements such as Cr, Mo, and Si play in retarding softening. It has been reported in the literature that these alloy additions slow cementite growth by changing the limiting diffusion mechanism responsible for cementite growth from interstitial diffusion of carbon to substitutional diffusion of these alloying additions [75-77] without affecting cementite nucleation. Due to this, carbide forming elements only slow Stage II of the softening process without affecting Stage I.

As carbide coarsening (Stage II) dominates the softening process during typical welding and rapid tempering heat treatments, softening may be modelled as a single process. If tempering is carried out at temperatures below 400℃ or if areas of the weld zone further from the fusion boundary are being examined where the peak temperature is low then carbide nucleation (Stage I) must also be account for in a predictive model. Furthermore, during tempering at lower temperatures, carbide forming elements will not strongly retard softening as carbide coarsening will be a smaller portion of the overall softening process.

6.2 Softening Kinetics

When softening is viewed as a single process, it was seen that the change in hardness progressed sigmoidally with heat input (see Figure 6-3). This softening progression was well described by the JMAK equation. The heat required to soften the material was highly affected by martensite chemistry. Figure 6-3 shows how increasing the martensite C content decreased the heat input required to induce a given degree of softening for low and moderate degrees of softening ($\phi < 0.8$), whereas alloying with carbide forming alloying elements such as Cr and Mo make the material more resistant to softening, again at low and moderate degrees of softening. These effects are related to the processes responsible for softening. Increasing the martensite carbon content increased the C concentration gradient between the un-decomposed martensite and the surrounding ferrite, which increased the rate of C diffusion from the martensite, thereby increasing the rate of martensite decomposition [78]. Increasing carbide forming alloy content slowed cementite growth, decreasing the softening rate during the coarsening stage (Stage II) of softening [75].

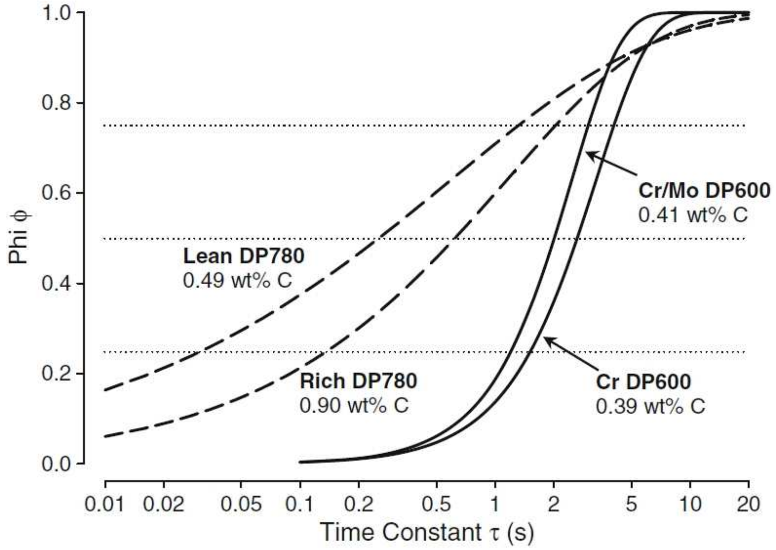

Figure 6-3. Comparison between the softening kinetics of four steels with various martensite volume fractions and alloying additions, per Table 3-1 (copied from Figure 3-10).

The effect of martensite C content on the softening rate may be directly examined by comparing the softening progression of the M190 and M220 steels from Chapter 4. The softening progression, which was examined for each tempering temperature in Figure 4-6, may be transformed to a single softening progression by calculating an effective tempering time at 650°C using Eq. 4-7. This allows the softening progressions from both materials to be directly compared. When overlaid in Figure 6-4, it may be seen that at early times, during the nucleation stage (Stage I of softening), the softening process progressed significantly more rapidly for the M220 than it did for the M190. This resulted in higher softening throughout most of the softening process. The increased rate of softening for M220 continued until the softening process was almost complete, at an effective tempering time of approximately 1 s, when there was no significant difference between the softening measured from both materials. When the data was logarithmically transformed (Figure 6-5), it may be seen that the y-intercept of the M220 data is greater for both the nucleation stage and for the beginning of the coarsening stage than that of the M190. This indicates that the JMAK k value (from Eq. 4-1) in both Stage I and II will be higher for the M220 than it will be for the M190, which implies that the M220 will have a lower activation energy, Q (from Eq. 4-2), than the M190 during both Stage I and II of the softening process. This agrees with the activation energies from Table 6-1, which is reflective of the activation energies of Stage II softening. From Figure 6-5, it may also be seen that M190 steel exhibited less of overall softening progression in Stage I as compared to the M220 steel. This is believed to be due to the M190's lower C content (0.18 wt% compared to 0.23 wt%). This would result in fewer carbides precipitating during the nucleation (Stage I), resulting in a lower hardness of the tempered martensite (at the end of Stage I), therefore a greater proportion of the overall softening would occur in Stage II, carbide coarsening. This resulted in the slope of the data corresponding to Stage II softening for the M190 being steeper than that of the M220 data, indicating that the time exponent, n, of the M190 steel should be greater than that of the M220 steel. Again, this agrees with the data from Table 6-1. From the comparison between the softening process in the M190 and M220, it was seen that martensite C content has a significant effect increasing the softening rate by lowering the activation energy for the process. From Figure 6-3, it was seen that Cr and Mo retarded the Stage II of the softening process, however, as this data was taken from welded samples no conclusions may be drawn on the effect of carbide forming elements on Stage I softening. Unfortunately there were no materials in the data set with similar C contents, but different levels of carbide forming alloying additions to allow the analysis from Figures 6-4 and 6-5 to be repeated to understand the role of Cr and Mo on the softening progression.

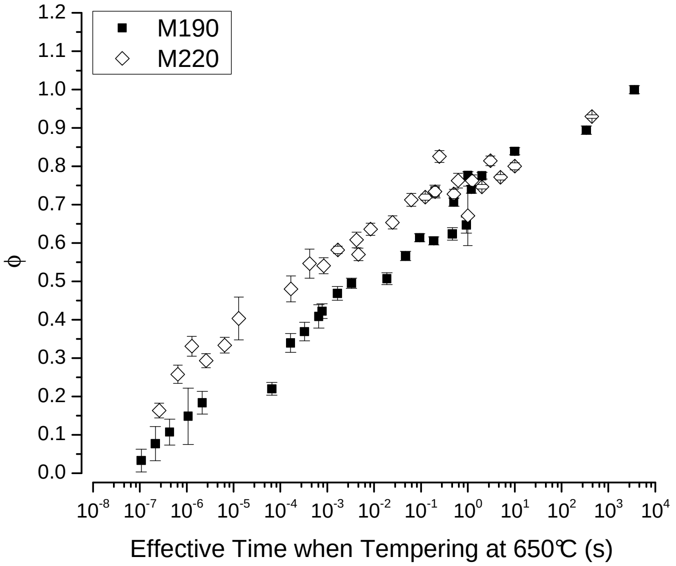

Figure 6-4. Softening (ϕ) of M190 and M220 versus effective tempering times at 650℃.

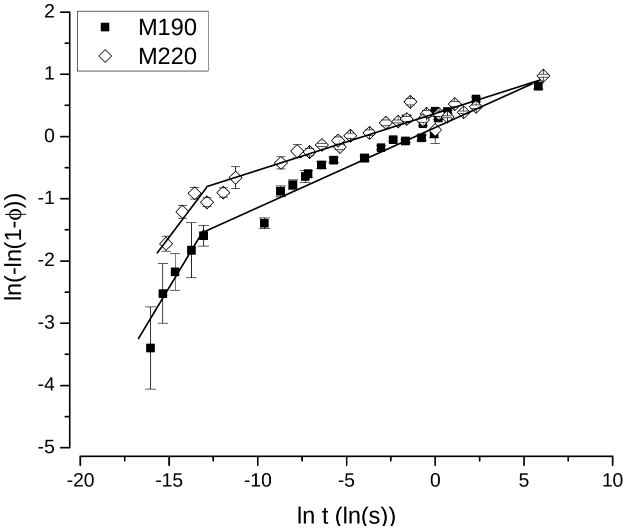

Figure 6-5. Logarithmic transformation of the M190 and M220 softening data adjusted to 650℃.

Table 6-1. JMAK fitting parameters and model goodness of fit measurement for experimental steels (copied from Table 4-3).

Steel	Q (kJ/mol)		k_0		n		Adj R^2
	Value	*95% CI*	Value	*95% CI*	Value	*95% CI*	
DP780	62.8	*13.72*	700.7	*1 245.0*	0.351	*0.048*	0.79
DP980-1	54.3	*3.90*	613.3	*320.3*	0.189	*0.012*	0.93
DP980-2	39.4	*2.10*	144.8	*42.3*	0.150	*0.010*	0.94
DP1180	39.2	*2.02*	167.7	*47.7*	0.139	*0.010*	0.94
M190	47.9	*2.61*	687.0	*254.2*	0.151	*0.013*	0.95
M220	28.3	*1.39*	59.9	*12.4*	0.101	*0.009*	0.94
Hot Stamped Boron	43.3	*1.84*	458.6	*122.2*	0.118	*0.010*	0.96

6.3 Predicting softening in welds

Softening during welding may be predicted because it can be modelled as a single process using the JMAK equation. However, as shown in Chapter 5, this assumption does not reflect the actual processes occurring in the system. For this reason, the JMAK triplet (Q, n and k_0)

may not be predicted from metallurgical theory and must be derived experimentally. It has been shown in this thesis that this may be accomplished by running a series of rapid tempering experiments at various temperatures and times to generate the data needed to calculate the JMAK triplet for each material using standard statistical methods. Once the Q, n, and k_0 values were empirically defined for a given steel, the final tempered hardness resulting from any general tempering heat treatment may be calculated if the time/temperature history is known (see Figure 6-6).

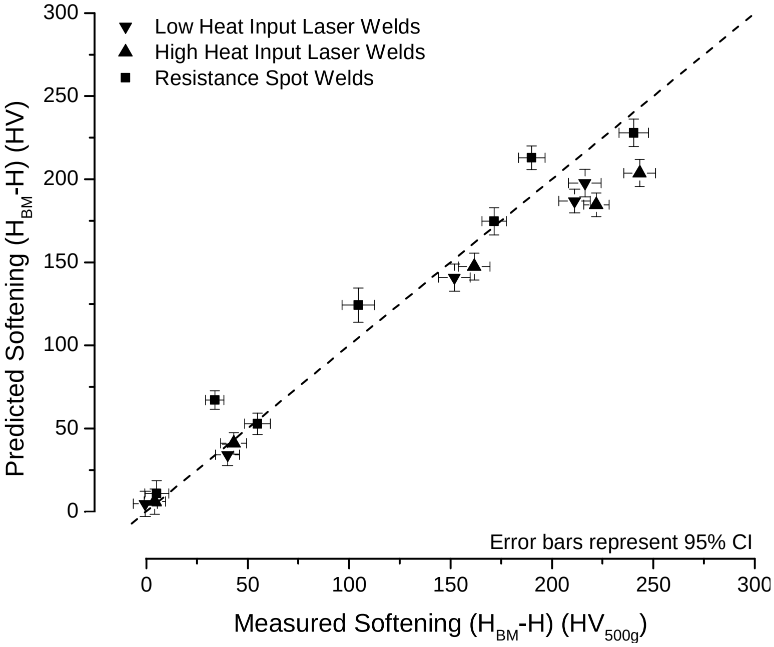

Figure 6-6. Comparison between the measured HAZ softening and the HAZ softening predicted by the JMAK equation using the parameters listed Table 4-3 (copied from Figure 4-8).

7 Conclusions and Future Work

7.1 Conclusions

This thesis sought to understand the kinetics and operative mechanisms in the HAZ softening of DP and martensitic steel weldments. From this work the follow conclusions were drawn:

1. Softening kinetics of martensitic and dual-phase steels with ferrite/martensite microstructures could be modelled using a novel technique, where steel samples were isothermally tempered with various time and temperature combinations below their Ac_1 temperature using a Gleeble. The change in hardness resulting from the various heat treatments was modelled as a single process using the JMAK equation, with the effect of temperature accounted for by the Arrhenius equation.
2. The softening kinetics measured using the isothermal tempering could be used to predict the maximum decrease in hardness measured in a weld HAZ if the thermal history of the weld was known.
3. The softening process occurs in two stages: carbide nucleation and coarsening.
   a. The carbide nucleation stage was completed at very short times, so it may only be measured at temperatures up to 420℃, above which it could not be experimentally measured. The

activation energy and time exponent for the carbide nucleation stage were 113 kJ/mol and 0.659, respectively, matching classic literature values for martensite tempering in low C steels.

b. Carbide nucleation occurs very rapidly at higher temperatures, so this process dominates during the HAZ softening process where the steel is near its Ac_1 temperature. During the carbide coarsening stage, carbides that formed during the nucleation stage grew with an associated increase in carbide spacing. This reduced their ability to reinforce the material by precipitation hardening. The relation between carbide coarsening and change in hardness was non-linear so the activation energy measured from hardness data during stage of softening did not match the classical literature associated with C diffusion.

4. Although carbide nucleation and coarsening are responsible for softening, in most rapid tempering applications softening may be accurately predicted by modelling only the coarsening stage. However, when tempering for short times (≤ 20 s) and at low temperatures (≤ 400℃), the nucleation stage must be accounted for, otherwise softening will be over-predicted.

7.2 Future Work

This work successfully clarified the processes responsible for softening and developed a technique to model this process. More work needs to be done to improve the industrial utility of this work and increase the understanding of the processes responsible for softening.

Using techniques developed in this work, softening may be predicted if the JMAK constants Q, n and k_0 are known. These may now only be found empirically by fitting experimental data. The experiments needed to generate this data are both time consuming and require specialized equipment. To improve the usability of the techniques described in this work, a greater number of chemistry variants must be tested allowing Q, n and k_0 to be directly correlated to martensite chemistry. This will allow for the prediction of softening without the need for isothermal tempering experiments as long as the chemistries chosen for the isothermal tempering experiments are wide enough to encompass the steel chemistries being used for tempering applications .

This work also leaves some fundamental questions about the growth kinetics of cementite during tempering. It was shown that chemistry plays an integral role in determining the rate of softening; however, this work was only able to describe how C affects the softening rate. To gain a better understanding of the role that substitutional alloying elements such as Si, Cr, and Mo have on softening, more work needs to be done comparing steels of like chemistries where these elements are varied and observing how these elements affect carbide nucleation and growth.

Finally this thesis focused on how tempering and microstructural changes affect the post-tempered hardness. However, no attention was given to how microstructural changes affect the local tensile properties. Even though local hardness may be easily measured, it is the local tensile properties that govern how the HAZ will behave when stressed after welding. To fully understand post-welded properties, work must be pursued to determine how local tensile properties change in the sub-critical HAZ due to welding.

8 References

1. US Government, "2017 and Later Model Year Light-Duty Vehicle Greenhouse Gas Emissions and Corporate Average Fuel Economy Standards," Federal Register, vol. 77, no. 199, pp. 62624-63200, 2012.

2. M. Johannaber, M. Espig, R. Wohlecker, H. Wallentowitz and J. Leyers, "Determination of Weight Elasticity of Fuel Economy for Conventional ICE Vehicles, Hybrid Vehicles, and Fuel Cell Vehicles," Forschungsgesellschaft Kraftfahrwesen mbH, Aachen, 2007.

3. WorldAuto Steel, Advanced High Strength Steel (AHSS) Application Guidelines, Version 4.1 ed., International Iron & Steel Institute, 2009.

4. G. R. Speich, "Physical Metallurgy or Dual-Phase Steels," in Fundamentals of Dual-Phase Steels, R. A. Kot and B. B. L, Eds., Metallurgical Society of the AIME, 1981, pp. 3-45.

5. R. G. Davies, "Influence of Martensite Composition and Content on the Properties of Dual Phase Steels," Metall. Trans. A, vol. 9A, no. 5, pp. 671-679, May 1978.

6. E. C. Bain and H. W. Paxton, Alloying Elements in Steel, 2nd Edition ed., Metals Park: American Society for Metals, 1966.

7. D. K. Matlock, F. Zia-Ebrahimi and G. Krauss, "Structure, Properties, and Strain Hardening of Dual-Phase Steels," in Deformation, Processing, and Structure, G. Krauss, Ed., Metals Park, American Society for Metals, 1982, pp. 47-87.

8. D. A. Korzekwa, D. K. Matlock and G. Krauss, "Dislocation Substructure as a Function of Strain in a Dual-Phase Steel," Metall. Trans. A, vol. 15A, no. 6, pp. 1221-1228, June 1984.

9. S. S. Hansen and R. R. Pradhan, "Structure/Property Relationship and Continuous Yielding Behavior in Dual-Phase Steels," in Fundimentals of Dual-Phase Steels, Warrendale, Metallurgical Society of the AIME, 1981, pp. 113-144.

10. J. M. Rigsbee and P. J. VanderArend, "Laboratory Studies of Microstructures and Structure-Property Relationships in "Dual-Phase" HSLA Steels," in Formable HSLA and Dual-Phas Steels, Chicago, IL, 1977.

11. A. Saha Podder, D. Bhattacharjee and R. K. Ray, "Effect of Martensite on the Mechanical Behavior of Ferrite-Bainite Dual Phase Steels," ISIJ Int., vol. 47, no. 7, pp. 1058-1064, 2007.

12. J. D. Embury and J. L. Duncan, "Formability of Dual-Phase Steels," in Fundamentals of Dual-Phase Steels, R. A. Kot and B. L. Bramfitt, Eds., Warrendale, Metallurgical Society of the AIME, 1981, pp. 333-345.

13. A. Ribolla, G. L. Damoulis and G. F. Batalha, "The use of Nd: YAG laser weld for large scale volume assembly of automotive body in white," J. Mater. Process Technol., Vols. 164-165, pp. 1120-1127, May 2005.

14. N. T. Williams, "Resistance Spot Welding," in ASM Handbook, Volume 6, Welding, Brazing, and Soldering, D. LeRoy Olson, T. A. Siewert, S. Liu and G. R. Edwards, Eds., Materials Park, ASM International, 1993, pp. 226-229.

15. D. B. Holliday, "Gas-Metal Arc Welding," in ASM Handbook, Volume 6, Welding, Brazing, and Soldering, D. LeRoy Olsen, T. A. Siewert, S. Liu and G. R. Edwards, Eds., Materials Park, ASM International, 1993, pp. 180-185.

16. J. E. Gould, S. P. Khurana and T. Li, "Predictions of Microstructures when Welding Automotive Advance High-Strength Steels," Weld. J., vol. 55, no. 5, pp. 111s-116s, May 2006.

17. W. W. Duley, Laser Welding, New York: John Wiley & Sons, Inc, 1999.

18. D. Havrilla, April 2013. [Online]. Available: http://www.seas.virginia.edu/research/lam/pdfs/speaker%20presentations/Havrilla-UofV_Laser%20Based%20Manufacturing%20in%20the%20Automotive%20Industry.pdf.

19. E. Biro, Weldability of plated thin sheet and Cu by Pulsed Nd:YAG laser Welding, Waterloo: Univeristy of Waterloo, 2001.

20. E. Powidajko, Weldability of AZ31B Magnesium Sheet by Laser Welding Process, Waterloo: University of Waterloo, 2009.

21. J. Mazumder, "Laser-Beam Welding," in ASM Handbook, Volume 6, Welding, Brazing, and Soldering, D. LeRoy Olsen, T. A. Siewert, S.

Liu and G. R. Edwards, Eds., Materials Park, ASM International, 1993, pp. 262-269.

22. K. Easterling, Introduction to the Physical Metallurgy of Welding, London: Butterworths & Co.(Publishers) Ltd., 1983.

23. Parmar, Welding Engineering and Technology, Delhi: Khanna Publishers, 1997.

24. D. Rosenthal, "Mathematical Theory of Heat Distribution During Welding and Cutting," Weld. J., vol. 20, no. 5, pp. 220s-234s, May 1941.

25. D. Rosenthal, "The Theory of Moving Sources of Heat and its Application to Metal Treatments," Trans. ASME, vol. 68, no. 11, pp. 849-866, Nov 1946.

26. J. C. Ion, K. E. Easterling and M. F. Ashby, "A Second Report on Diagrams of Microstructure and Hardness for Heat-Affected Zones in Welds," Acta Metall., vol. 32, no. 11, pp. 1949-1962, Nov 1984.

27. M. Xia, E. Biro, Z. Tian and Y. N. Zhou, "Effects of Heat Input and Martensite on HAZ Softening in Laser Welding of Dual Phase Steels," ISIJ Int., vol. 48, no. 6, pp. 809-814, June 2008.

28. R. Komanduri and Z. B. Hou, "Thermal Analysis of the Arc Welding Process: Part I. General Solutions," Metall. Mater. Trans. B, vol. 31B, no. 6, pp. 1353-1370., Dec. 2000.

29. H. Kitahara, R. Ueji, N. Tsuji and Y. Minamino, "Crystallographic Features of Lath Martensite in Low-Carbon Steel," Acta Mater., vol. 54, no. 5, pp. 1279-1288, Mar. 2006.

30. W. F. Smith, Structure and Properties of Engineering Alloys, 2nd ed., New York: McGraw-Hill, Inc., 1993.

31. G. R. Speich, "Temepring of Low-Carbon Martensite," Trans. Met. Soc. AIME, vol. 245, no. 12, pp. 2553-2564, Dec. 1969.

32. D. P. Anita, S. G. Fletcher and M. Cohen, "Structural Changes During the Tempering of High Carbon Steel," Trans. Am. Soc. Metal., vol. 32, pp. 290-332, 1944.

33. M. Jung, S.-J. Lee and Y.-K. Lee, "Microstructural and Dilatational Changes during Tempering and Tempering Kinetics in Martensitic

Medium-Carbon Steel," Metall. Mater. Trans. A, vol. 40A, no. 3, pp. 551-559, Mar. 2009.

34. K. H. Jack and S. Wild, "Nature of x-Carbide and its Possible Occurances in Steels," Nature, vol. 212, pp. 248-250, Oct. 1966.

35. L. Cheng, C. M. Brakman, B. M. Korevaar and E. J. Mittemeijer, "The Tempering of Iron-Carbon Martensite; Dilatometric and Calorimetric Analysis," Metall. Trans. A, vol. 19A, no. 10, pp. 2415-2426, Oct. 1988.

36. Gaude-Fugarolas, Modelling of Transformations during Induction Hardening and Tempering, Cambridge: Corpus Christi College, University of Cambridge, 2002.

37. S. Yamasaki, Moelling Precipitation of Carbides in Martensitic Steels, Cambridge: Darwin College, University of Cambridge, 2004.

38. S. Hashimoto, S. Kanbe and T. Sudo, "The Effect of Microstructure on the Characteristics of Flash Butt Welded High Strength Hot-rolled Sheet Steel (Development of Ferrite-Bainite-(Martensite) Sheet Steel - V)," T. Iron Steel Jpn., vol. 21, no. 11, pp. B-497, Nov 1981.

39. N. Yamauchi, T. Taka, K. Kunishege and N. Nagao, "Softening Behavior in Heat Affected Zone of Flash Butt Welded Hot Rolled Dual Phase Steel (HSLA Having Low Yield Ratio - VII)," T. Iron Steel I. Jpn., vol. 22, no. 4, pp. B-107, 4 1982.

40. K. Kunishige, N. Yamauchi, T. Taka and N. Nagao, "Softening in Weld Heat Affected Zone of Dual Phase Steel Sheet for Automotive Wheel Rim," in SAE International Congres & Exposition, Detroit, MI, 1983.

41. E. Biro and A. Lee, "Welded Properties of Various DP600 Chemistries," in Sheet Metal Welding Conference XI, Sterling Heights, MI, 2004.

42. P. K. Ghosh, P. C. Gupta, O. M. Pal, A. R, B. K. Jha and V. Sagar Dwivedi, "Influence of Weld Thermal Cycle on Properties of Flash Butt Welded Mn-Cr-Mo Dual Phase Steel," ISIJ Int., vol. 33, no. 7, pp. 807-815, July 1993.

43. E. Biro and A. Lee, "Tensile Properties of Gleeble-Simulated HAZ from Various Dual-Phase Steels," in Sheet Metal Welding XII, Livonia, MI, 2006.

44. N. Sreenivasan, M. Xia, S. Lawson and Y. Zhou, "Effect of Laser Welding on Formability of DP980 Steel," Trans. ASME: J. Eng. Mater. Technol., vol. 130, no. 4, pp. 041004-1 to -9, April 2008.

45. V. H. Baltazar Hernandez, S. K. Panda, M. L. Kuntz and Y. Zhou, "Nanoindentation and Microstructure Analysis of Resistance Spot Welded Dual Phase Steel," Mater. Let., vol. 64, no. 2, pp. 207-210, Feb. 2010.

46. D. A. Porter and K. E. Easterling, Phase Transformations in Metals and Alloys, 2nd ed., Berkshire: Van Nostrand Reinhold (UK) Co. Ltd., 1981.

47. R. W. Balluffi, M. Cohen and B. L. Averbach, "The Tempering of Chromium Steels," Trans. Am. Soc. Metal., vol. 63, pp. 497-525, 1951.

48. W. S. Owen, "The Effect of Silicon on the Kinetics of Tempering," Trans. Am. Soc. Metal., vol. 66, pp. 812-829, 1954.

49. J. N. Wong, D. S. Kim and S. T. Ahn, "Effects of alloying elements on microstructural evolution and mechanical properties of induction quench-and-tempered steels," J. Mater. Sci., vol. 38, no. 17, pp. 3611-3617, Sept. 2003.

50. J. W. Christian, The Theory of Transformations in Metals and Alloys, Part I: Equilibrium and General Kinetic Theory, Second Edition, Oxford: Pergamon Press, 1975.

51. R. A. Grange, C. R. Hribal and L. F. Porter, "Hardness of Tempered Martensite in Carbon," Metall. Trans. A, vol. 8A, no. 11, pp. 1775-1785, Nov. 1977.

52. J. H. Hollomon and L. D. Jaffe, "Time-Temperature Relations in Tempering Steel," Trans. Am. Inst. Miner. Metall. Eng., vol. 162, pp. 223-249, Sept. 1945.

53. J. J. Hoyt, Phase Transformations, Hamilton: Titles On Demand, 2010.

54. I. M. Lifshitz and V. V. Slyozov, "The Kinetics of Precipitation from Supersaturated Solid Solutions," J. Phys. Chem. Solids, vol. 19, no. 1/2, pp. 35-50, 1961.

55. B. A. Lindsley and A. R. Marder, "The Morphology and Coarsening Kinetics of Spheroid Fe-C Binary Alloys," Acta Metall., vol. 46, no. 7, pp. 341-351, July 1998.

56. M. V. Speight, "Growth Kinetics of Grain-Boundary Precipitates," Acta Metall., vol. 16, no. 1, pp. 133-135, Jan. 1968.

57. A. J. Ardell, "On the Coarsening of Grain Boundary Precipitates," Acta Metall., vol. 20, no. 4, pp. 601-602, April 1972.

58. A. N. Shiryayev, Ed., Selected Works of A.N. Kolmogorov, Volume II Probability Theory and Mathematical Statistics, Kluwer Academic Publishers, 1992.

59. W. A. Johnson and R. F. Mehl, "Reaction Kinetics in Processes of Nucleation and Growth," Trans. Am. Inst. Miner. Metall. Eng., vol. 135, pp. 416-458, 1939.

60. M. Avrami, "Kinetics of Phase Change. I General Theory," J. Chem. Phys., vol. 7, pp. 1103-1112, Dec. 1939.

61. M. Avrami, "Kinetics of Phase Change. II Transformation-Time Relations for Random Distribution of Nuclei," J. Chem. Phys., vol. 8, pp. 212-224, Feb. 1940.

62. M. Avrami, "Granulation, Phase Change, and Microstructure Kinetics of Phase Change. III," J. Chem. Phys., vol. 9, pp. 177-184, Feb. 1941.

63. Y. Tomita, "Evaluation of Rate Constants in Tempering Reaction of Hardened Steels From Dilatometric Data on Continuous Heating at Controlled Rates," Mater. Sci. Technol., vol. 4, pp. 977-983, 1988.

64. T. Waterschoot, K. Verbeken and B. C. De Cooman, "Tempering Kinetics of the Martensite Phase in DP Steel," ISIJ Int., vol. 46, no. 1, pp. 138-146, 2006.

65. E. J. Mittemeijer, L. Cheng, P. J. van der Schaaf, C. M. Brakman and B. M. Korevaar, "Analysis of Nonisthermal Transformations Kinetics; Tempering of Iron-Carbon and Iron-Nitrogen Martensites," Metall. Trans. A, vol. 19A, no. 4, pp. 925-932, 1988.

66. M. Takahashi and H. K. D. H. Bhadeshia, "Model for Transition from Upper to Lower Bainite," Mater. Sci. Technol., vol. 6, pp. 592-603, 1990.

67. S. Harper, "Precipitation of Carbon and Nitrogen in Cold-Worked Alpha-Iron," Phys. Rev., vol. 83, no. 4, pp. 709-712, 1951.

68. L. V. Meisel and P. J. Cote, "Non-Isothermal Transformation Kinetics: Application to Metastable phases," Acta Metall., vol. 31, no. 7, pp. 1053-1059, 1983.

69. J. W. Cahn, "Transformation Kinetics During Continuous Cooling," Acta Metall., vol. 4, pp. 572-575, 1956.

70. J. Shi and C. R. Liu, "On Predicting Softening Effects in Hard Turned Surfaces-Part I: Construction of Material Softening Model," J. Manuf. Sci. Eng.-Trans. ASME, vol. 127, no. 8, pp. 476-483, 2005.

71. S. Denis, D. Farias and A. Simon, "Mathematical Model Coupling Phase Transformations and Temperature Evolutions in Steels," ISIJ Int., vol. 32, no. 3, pp. 316-325, 1992.

72. M. Lusk and H.-J. Jou, "On the Rule of Additivity in Phase Transformation Kinetics," Metall. Mater. Trans. A, vol. 28A, no. 2, pp. 287-291, 1997.

73. S. L. Semiantin, D. E. Stutz and T. G. Byrer, "Induction Tempering of Steel: Part II. Effect of Process Variables," J. Heat Treating, vol. 4, no. 1, pp. 47-55, 1985.

74. O. P. Hedegärd and M. A. T. Åslund, Tempering of Hot-Formed Steel Using Induction Heating, Gothenburg, Sweden: Chalmers University of Technology, 2011.

75. W. J. Nam, D. S. Kim and S. T. Ahn, "Effects of Alloying Elements on Microstructural Evolution and Mechanical Properties of Induction Quench-and-Tempered Steels," J. Mater. Sci., vol. 38, no. 17, pp. 3611-3617, 2003.

76. S. S. Babu, K. Hono and T. Sakurai, "Atom Probe Field Ion Microscopy Study of the Partitioning of Substitutional Elements during Tempering of a Low-Alloy Steel Martensite," Metall. Mater. Trans. A., vol. 25A, no. 3, pp. 499-508, 1994.

77. W. J. Nam, S. L. Chong and D. Y. Ban, "Effects of Alloy Additions and Tempering Temperature on the Sag Resistance of Si-Cr Spring Steel," Mater. Sci. Eng. A., vol. 289, no. 1-2, pp. 8-17, 2000.

78. A. Fick, "On Liquid Diffusion," Philos. Mag., Vols. 10 - Fourth Series, pp. 30-39, 1855.